Quantifying Patterns of Morphological Diversity

Quantifying Patterns of Morphological Diversity

A DISSERTATION PRESENTED
BY
JOERG FRITZ
TO
THE SCHOOL OF ENGINEERING AND APPLIED SCIENCES

IN PARTIAL FULFILLMENT OF THE REQUIREMENTS
FOR THE DEGREE OF
DOCTOR OF PHILOSOPHY
IN THE SUBJECT OF
APPLIED MATHEMATICS

HARVARD UNIVERSITY
CAMBRIDGE, MASSACHUSETTS
AUGUST 2013

Thesis advisor: Michael Brenner Joerg Fritz

Quantifying Patterns of Morphological Diversity

Abstract

One of the central questions of biology is how shape is formed by the interaction of gene expression, cell growth and differentiation. The canonical approach to this problem is the detailed study of all these basic processes in a small number of selected model species. In this study we will approach this question from a slightly different perspective, by investigating patterns of diversity in closely related organisms. Can we quantitatively understand these patterns of morphological diversity? In general, this question is even harder to answer than the classical problem described before. Closely related species share many aspects of their developmental program, which constrains the possible morphologies that can develop. In addition, the selective pressures on the morpholgies of closely related species might also be similar, creating an additional mechanism to create patterns of similarity.

The relative importance of constraints due to a shared developmental program versus selection in determining patterns of morphology can strongly vary, further complicating matters. However the deemphasis of model species allows us to study asymptotic limits, that is systems where the pattern is nearly totally dominated by one of the above factors.

We first investigate the shapes of songbird beaks, and uncover an intriguing pattern where the beak profiles of closely related birds are nearly perfectly approximated as conic sections. Based on this pattern of morphology we determine what features the underlying developmental mechanism of all species must share to produce exactly this pattern, but no other shapes. We uncover a strong constraint on the dynamics of the growth zone of dividing cells that initially shapes the beak in terms of power laws for its size and and movement.

In the opposing limit we study a central element of the ascomycete spore shooting mechanism. Apical rings function as natural O-rings that seal of a pressure reservoir, while at the same time minimizing friction for ejected fungal spores. The trade-off between sealing and minimizing friction enforces a highly non-linear optimum ring shape. 90% of real apical ring geometries lie within 2% of this theoretical optimum.

Contents

Listing of figures

To all who have either significantly aided or impeded the completion of this thesis.

Acknowledgments

Working on my research and this thesis over the last 4 years has been a great, but pretty often overwhelming, experience. Many of the most valuable things I've learned were not what I expected, and had nothing to do with math: working in a team, giving a coherent talk, staying up and working longer than I've ever done in my life, teaching more interactively, writing a well-structured paper or generally getting things done and not being perfectionist about everything (…okay, I'm still working on that one).

I had a lot of help in all that from Michael Brenner, without a doubt one of the most intuitive, smart and supportive advisors anyone could hope for. During our first meeting he came up with more than 10 different projects on the spot while watching youtube videos about Cordyceps (seriously, google Cordyceps!); this probably counts as one of the most surreal experiences of my life. By now I know this was just par for the course, which probably makes it even more impressive, especially given that these random ideas make up most of my thesis. Thank you for your ideas, support and inspiration, and also for giving me the occasional push in the forward direction.

Michael has also fostered the most open, collaborative and friendly research group I could imagine. Some of them have helped tremendously with the science in the thesis. But probably more importantly, many of them have become really good friends. My closest collaboration was with Agnese Seminara who shared my

interest in mycology, taught me a lot about persistence, creating models, clarity when writing papers and the value of margaritas on Friday evenings. She was also the nucleus for our self-organizing group lunches, where I first met many others of this group. Another notable member of this group was Shreyas Mandre who was always around to give advice, bounce off ideas and teach me about fluid dynamics by not answering my questions. Shreyas and his wife, Radhika Kelkar, were also fantastic friends and neighbors in Peabody Terrace, were we spent many evenings chatting, laughing and cooking Indian food. Tobias Schneider made sure that I didn't forget all my German, and that I went running at least occasionally. Watching the Ironman Hawaii on the projector in Pierce 306 with Tobias was a real highlight (and next time we do this, we'll get work done on that day, I'm sure). Niall Mangan was a fantastic office mate, always ready to help, be distracted or correct my English, and is probably responsible for me coming into the office a lot more often than I would otherwise have. Unfortunately, she is also responsible for introducing me to xkcd, Questionable Content and other web comics, so I'm making no claims about an increase in efficiency.

Otger Campas provided lots of support during the initial stages of the beak shape project, and together with our collaborators Ricardo Mallarino and Joe Brancale we've spent quite a few hours in the Museum of Natural History taking photos of bird beaks. Rob Viesca was always a fountain of information about Boston, Cambridge and where to get the best free food. Thanks for the entertaining lunches, parties and visits to improv theater. Finally, Zorana Zeravic and Andrej Mesaros have been great friends, during countless entertaining dinners, our weekly shopping trips, or just when walking home from work. They also came through in the clutch, when our move away from Cambridge coincided with my thesis deadline and helped pack up our apartment (okay, they didn't help, they did most of the work). It has truly been a pleasure to spend time with so many interesting, unique and nice people.

During my whole PhD Anne Pringle has been sort of an unofficial second advisor, always available to help, listen to new ideas or give valuable advice. She taught me everything I know about fungi and most of what I know about biology

in general. Anne has also assembled the nicest and most diverse research group I have ever seen: people with backgrounds from ecology, evolutionary biology, genomics, physics, math, social science, to philosophy. I can not imagine a group I would rather have shared cookies and cakes with during group meetings.

Sometimes it feels like there was no life before the PhD, but when my parents visited for the defense, I was reminded of many things that happened before I came here. My mother has always been there for me with continuous support and encouragement and taught me a love of language, art and of teaching. My father is undoubtedly responsible for my love of numbers, math and desire to understand connections between diverse topics, but with equal certainty also for telling everyone in my small home town about where I go to school. Thanks also to my sister Melanie, who tried to keep me sane over the transatlantic phone system by reminding me that there is life outside the office, even though I didn't call nearly often enough.

Finally, Lidiya Mishchenko has been the best one-women support group imaginable over the last 4 years. She has seen my best and worst, provided moral support, good advice, hugs and the occasional hot meal, made me work, relax, smile and clean the dishes and introduced me to frozen yogurt, plov, Firefly and Gena the Crocodile (if you think you might like an aquatic tetrapod whose favorite activity it is to read the phone directory, you should totally look this up). I couldn't have finished this without your help!

The human mind evolved to believe in the gods.
It did not evolve to believe in biology.

E.O. Wilson

1

Introduction and Summary

If you are reading this chances are you are the kind of person that tries to find common themes and connecting elements between different topics[1]. In the interest of full disclosure an equally fitting title of this thesis would probably be "Things that seemed like an interesting idea at the time". But whether through the foresight of my advisors or chance, there is actually an interesting and meaningful story arc that connects much of my PhD work. The main purpose of this chapter is to highlight this connecting thread and several other minor themes that reappear several times in this work.

This thesis divides naturally into three parts, which are relatively independent

[1] Let's be honest. You're actually reading an *Introduction* of a PhD thesis. I can only see three possibilities here (a) you like introductions a lot (b) you are a member of my thesis committee (c) you are one of my friends. In any of those cases, the claim is probably right.

and can be read in any order.

- the experimental analysis of songbird beak shapes, their patterns of similarity and what we can deduce about their developmental program based on these similarities (chapter 2)
- the theoretical analysis of features of the spore shooting mechanism in fungi that predicts an optimal and highly nontrivial morphology which real morpholgies nearly perfectly adhere to (chapter 3)
- a theoretical explanation of the systematic changes in growth rate as a function of size for an important class of lichens and a comparison of this theory to real life growth rates (chapter 4)

The goals and subject matter of the three parts are sufficiently different to merit individual introductions and summaries, which follow below.

1.1 Songbird beak morphologies

The morphological diversity and adaptive significance of bird beaks provides one of the most convincing examples of natural selection. The high degree of developmental autonomy of this trait make it ideal for tackling questions about principles and mechanisms of morphological diversification. One of the most fundamental question of biology is to determine the relative contribution of selective pressures versus developmental constraints in shaping morphological diversity. Direct comparison of the relative importance of these two factors is challenging, because it requires understanding developmental mechanisms operating over a wide phylogenetic range, far exceeding the small number of model systems currently in investigation. We present an approach to address this problem, by studying the inverse problem: given the patterns of beak shapes realized in nature, what essential requirements must be shared by the underlying developmental programs to be capable of producing the extant morphological diversity. We find that the dynamics of the growth zone, a set of tightly

constrained proliferating cells near the tip of the beak, has to follow a very restrictive set of rules which constrain diversity to a three parameter family of beak shapes. We experimentally verify these predictions by analyzing cell proliferation in the developing beaks of zebra finch embryos. Our results indicate that the variability of beak shapes is both strongly constrained and potentiated by the precise structure of the beak developmental program.

This work is based on some initial ideas and observations by Otger Campas, Michael Brenner and Arhat Abzhanov. All developmental experiments described in this section where carried out by members of the Abzhanov lab: Ricardo Mallarino, Masayoshi Tokita, Joe Brancale and Brent Hawkins. The experimental analysis of beak shapes was done mainly be Joe Brancale and me. All theory in this chapter is developed by Michael Brenner and me in collaboration.

1.2 Fungal Spore shooting apparatus

The forcibly ejected spores of ascomycete fungi must penetrate several millimeters of nearly still air surrounding sporocarps to reach dispersive airflows, and escape is facilitated when a spore is launched with large velocity. To launch, the spores of thousands of species are ejected through an apical ring, a small elastic pore. The startling diversity of apical ring and spore shapes and dimensions make them favored characters for both species descriptions and the subsequent inference of relationships among species. However, the physical constraints shaping this diversity and the adaptive benefits of specific morphologies are not understood. Here, we develop an elastohydrodynamic theory of the spore's ejection through the apical ring, and demonstrate that to avoid enormous energy losses during spore ejection, the four principal morphological dimensions of spore and apical ring must cluster within a nonlinear one-dimensional subspace. We test this prediction using morphological data for 45 fungal species from two different classes and seventeen families. Our sampling encompasses multiple loss and gain events and potentially independent origins of this spore ejection mechanism. Although the individual

dimensions of the spore and apical ring are only weakly correlated with each other, they collapse into the predicted subspace with high accuracy. The launch velocity appears to be within 2% of the optimum for over 90% of all forcibly ejected species. Although the morphological diversity of apical rings and spores appears startlingly diverse, a simple principle can be used to organize it.

This work was done in close collaboration with Anne Pringle, who contributed a lot about the ecology and biology of the fungal species that we consider in this study. Marcus Roper, Agnese Seminara and Michael Brenner supported me in, and contributed significantly to, the development of the theory described in this chapter. The data analysis of apical ring morphologies was done mostly by me, with help by Agnese Seminara.

1.3 The growth speed of lichens

Lichens are a symbiosis of a fungus and photosynthetic algae or bacteria. This very specific lifestyle allows lichens to grow in environments where little else can grow, e.g. on rocks, or in desserts. The downside to these environments is that important nutrients often cannot be taken up by the substrate on which the lichen is growing. The only source for nutrition is the air around them, lichens are literally eating air. The most important compound limiting their growth is carbon, which is gained by the photobiont during photosynthesis from atmospheric CO_2. Given the density of photobionts close the the surface of most lichens, CO_2 will be completely depleted very close to the surface at steady state. Since lichens generally grow in wind protected areas, they are surrounded by a boundary layer of nearly still air with a thickness on the order of centimeters. Thus the depleted CO_2 cannot be replenished by active transport (e.g. wind over the lichen surface) and is instead diffusing through the boundary layer. The pattern of diffusion is very different for a small, roughly hemispherical, lichen and a larger, roughly circular disk-like, lichen. For a small lichen, the flux over the surface area is constant and all the area contributes evenly to carbon uptake. Thus, with increased size, the surface area increases ind the growth rate

accelerates. However as the lichen grows its height remains roughly constant while its radius continues to increase, thus creating a more and more disk like morphology. The flux of carbon into a large lichen is distinctly different, with nearly all the flux concentrated at the edge of the disk where the growth front lies.

We compare this theoretical prediction to the growth speeds of 10 different lichen species and find very good agreement. It is also consistent with all experimental data on factors that influence the growth speed and correctly predicts the maximal growth speed of lichens in terms of only 4 parameters: the height H of the lichen, the diffusion constant D of CO_2 in air, the and the density of CO_2 in air and inside the lichen mycelium.

This work is based on an idea by Michael Brenner and Anne Pringle, originally conceived while Michael was, probably intentionally[2], spilling some coffee on a table at the Radcliffe Institute. Filling out the details of the theory and the comparison of real life growth speeds for different species to this theory was performed by me.

1.4 The interplay between selection and developmental constraints

The canonical picture of how morphological diversity is shaped prescribes a constraint on possible morphologies based on what the developmental program of a given organism can produce. Within this space, selection can act and select the morphologies than maximize fitness. Recent research has also highlighted that most morphologies are subject to a large number of, generally competing, functional demands, so fitness is not maximized by optimizing for a specific goal, but is a compromise between the competing demands. How strongly the developmental constraint restricts possible shapes and how steep the fitness landscape is, varies strongly between different systems, but generally both

[2] though this is also a great excuse for the next time you spill liquid on a table. Simply start talking about evaporating drops and how the fluid mechanics of that is exactly what is determining the growth speed of lichens

components are needed to even qualitatively understand existing morphologies.

The topics in chapters 2 and 3 are on opposite ends of the spectrum in the interplay between developmental constraints and selection. In chapter 2 we study a feature, beak shape modulo size, that has only very weak selective pressures acting on it. While different beak shapes can change the fitness of an individual in terms of its biting force or characteristics of its song, a small change in overall beak size produces significantly bigger changes in both aspects. Based on this and additional experimental evidence we expect and confirm that most aspects of beak shape can be completely understood in terms of developmental constraints.

In contrast, chapter 3 deals with spore dispersal in fungi. The selective pressures in this system are extremely strong and nearly binary. If a microscopic spore makes it out of the boundary layer its small size allows for long-range dispersal. However, without making it out of the boundary layer, it falls back on its parent fungus, essentially reducing the fitness of the spore to zero. In addition, fungal fruiting bodies are produced with the sole purpose of dispersing spores, they have no other biological function and thus the competing functional demands encountered in most other systems simply don't exist. Thus we expect and can confirm by comparison to real morphologies that shape is formed nearly exclusively by the selective pressure to eject the spore out of the boundary layer.

Since most, in fact nearly all, biological systems do not fall neatly at the edge of this continuum between development and selection, it is valid to ask if we can learn something general from these two examples. Mathematics indicates that the answer should be yes. The idea that studying the limiting behavior of a problem, the asymptotics, can often reveal a lot about the more complicated processes between the extremes is deeply entrenched in applied mathematics and responsible for some of the most important results of theoretical physics. How exactly this framework can be extended to biological problems is not completely transparent however.

1.5 The role of boundary layers in shaping biological diversity

Both chapters 3 and 4 discuss in detail how fluid dynamical constraints shape the morphologies of organisms. And in both cases, one of the central factors shaping these constraints are boundary layers. In chapter 3 the need of microscopic fungal spores to cross the boundary layer around the fruiting body where they are produced is the main driver for the optimal shape of apical rings. In chapter 4 the boundary layer around a growing lichen restricts the flux of carbon through the lichen surface, creating an effective upper limit for the growth speed of the organism.

The fact that both chapters deal with fungi is likely not a complete coincidence. How strongly the existence of boundary layers affects an organism depends strongly on its size. Organisms that share the same features and lifestyle, but are only one order of magnitude larger than the fungal equivalent, are generally nearly unaffected by boundary layers. Dust seeds, the smallest seeds in the fungal kingdom are only about 10 times larger than the biggest fungal spores. Yet even this is enough for these seeds to completely span the boundary layer at higher wind speeds or unsteady conditions, completely negating the huge constraint that shapes the morphologies of fungal spores and the mechanisms that forcible eject them.

1.6 Data analysis versus experiments

Another interesting aspect shared by all three topics discussed in this thesis is that they contain fairly few new experiments, even though we attempt to make wide, sweeping predictions about the morphologies of a large number of biological entities. However, while low on experiments, all three projects discussed here feature heavy amounts of data analysis. In chapter 2 we collect and pairwise compare the shapes of over 100 different songbird species based on museum specimen. In chapter 3 we search over 2000 published papers by hand

for high-resolution images of apical rings to extract their dimension and compare them to theory. And in chapter 4 we again manually extract over 500 separate datapoints from over 20 different publications to compare real life growth data to the predicted universal growth curve.

This is one of the most redeeming features of studying patterns of morphological diversity. In some sense the relevant experiment has already been performed, by nature itself, and if those morphologies are well documented in the literature, then new knowledge can be gained in the library over the course of one week, instead of in a lab over the course of 2 years. The caveat about good documentation of the relevant morphologies initially appears to be rather big, but closer examination reveals that it isn't. The biological literature is vast, and especially before the genetic revolution nearly every field of biology was intimately involved in describing some aspect of morphology. The implausibility of finding a high resolution cross section of an ascomycete apical ring, a tiny feature, only several μm big of a vastly understudied group of organisms, fungi, and hard to section in addition, is difficult to overstate. Yet we found extremely high quality transmission electron images of cross sections for over 40 different species, even though no study before ours ever needed precise dimensions of any dimension of apical rings.

The amount of hard, quantitative, and meaningful information in largely older biological literature is significant and probably vastly underused. This is something to consider at a time when university libraries across the country are downsizing and trying to become more efficient. While many biological theories from 30 years ago have been revised or become outdated, the data collected at those times is still invaluable.

There is something fascinating about science. One gets such wholesale returns of conjecture out of such a trifling investment of fact.

Mark Twain

2

The morphological diversity of bird beaks

Bird beaks are three dimensional structures that show a tremendous variability in shape and size. They have a profound impact on birds' ability to survive and reproduce, and play a major role in their radiation as the most diverse group of land vertebrates[47]. The adaptive significance of beaks coupled to the extreme levels of diversity observed in nature and high degree of developmental autonomy make this trait a useful model for tackling developmental and evolutionary questions about mechanisms of morphological diversification and principles of biological shape evolution[29]. Over a century of ecological research showed that differing beak shapes allow birds to adapt to different food sources, and it is still often argued that the shape of a beak is optimized for eating and foraging[102, 105]. Does beak morphological diversity primarily arise from the competing functional demands on its structure? An alternative point of view[62]

suggests that beak shape diversity is mainly the consequence of contingency, with the constraints on beak shape being imposed by the developmental program for the beak. Within this viewpoint, morphological adaptation to a food source would only act within the potentially tight constraints imposed by the nature of its developmental program[96]. Such arguments are notoriously difficult to resolve, in no small part because answering them requires understanding developmental mechanisms operating over a wide phylogenetic range. Although significant progress has been made in recent years at understanding bird beak development in several laboratory and natural model species (chicken, duck, quail, Darwin's finches)[1, 2, 50, 100, 120], we are far from having a synthesis of how developmental pathways diverge across a multitude of bird species.

Below, we present a novel approach to address this problem. Instead of trying to generalize from the developmental program and its influence on morphology in a small number of species to large-scale diversity we will pose the inverse problem: Given observed patterns of morphological diversity, which constraints on the developmental program must exist so the programs produce the observed, and only the observed, diversity? We will combine analysis of morphological data on the shapes of bird beaks for over 100 species with a theoretical analysis of the possible developmental programs that can produce such beak shapes and experimental evidence indicating that the developmental program in one common model species follows the predicted developmental program. The results of this analysis show that the variability of beak shape in songbirds largely arises from subtle changes in one universal developmental programs shared by all songbirds. Our calculations and experiments imply that the functional requirements on songbirds, such as adaptation to a food source, can operate at most within a three parameter family of beak shapes; the rest of the shape is determined by developmental constraints. We make specific quantitative predictions for the variability of beak shape development across songbirds, including quantitative predictions for the size and time dependence of the growth proliferation zones that give rise to the beak shape. We then verify these predictions in the most widely studied model organism in this group of birds, the

zebra finch *Taeniopygia guttata*, by studying patterns of cell proliferation using ethynyl deoxyuridine (EdU) labeling on medial sections of the upper beak during several key developmental stages when the beak forms and undergoes morphogenesis.

2.1 Quantification of beak shape diversity

The upper and lower beaks of birds develop largely independently[120], and many studies, including this one, focus on the morphologically more diverse and developmentally better understood upper beak. This structure is generally believed to be the critical biomechanics component for mastication (feeding) and other functions that experiences strong levels of selective pressure[105]. The recent discovery of the developmental genetic origin of beak shape diversity within the genus *Geospiza*, by several morphogens, e.g. Bmp4 expression in the beak primordium affects both beak width and depth[1], while Calmodulin expression controls beak length[2], implied that beak shape diversity within *Geospiza* is controlled simply by differing scales (length, width, and depth). This suggested that it might be possible to superimpose their beak shapes onto a single common shape after normalizing each axis with its corresponding scale. We recently[31] demonstrated that this is in fact the case, and moreover that the beaks of species in genera closely related to *Geospiza*, like the tree, Cocos or warbler finches, do not collapse onto the *Geospiza* beak shape under scaling, indicating that their beak shape is fundamentally different from the *Geospiza* shape. However by extending the class of transformations to include shear along the length component of the beak, the beak shapes across all these genera collapse onto the *Geospiza* shape[31]. That is, under a subset of affine transformations, all these beak shapes can be mapped onto each other. To examine this hypothesis and quantify the true amount of diversity present in songbird beaks, we analyzed the beak profiles obtained from lateral pictures of museum specimens of over 100 different species (see Figure 2.1.1), representing the diversity of beak shapes present in songbirds. Our analysis thoroughly

samples the tanagers (Thraupidae), one of the most diverse families of songbirds that also contains the Darwin's finches (Fig. 2.1.1), as well as the zebra finch (*T. guttata*), the most common model species for morphological and behavioral studies in the songbirds, and close relatives in the Estrildidae.

The shapes used for analysis were from specimens in the Museum of Comparative Zoology at Harvard University and the American Museum of Natural History in New York. Lateral photographs of museum specimens of each species were taken under slightly underexposed conditions (-1.5EV) with a Nikon D-90 digital camera. Underexposed photographs allow us to track the silhouette of the bird beak, making the detection of the beak profile more efficient and accurate. Using a feature detection program (Steerable—ImageJ plugin), we detect the contour of the beak at pixel resolution (Pixel size around 10 μm). The beak profile obtained from the feature detection analysis corresponds to a set of points (pixels) in the plane. In order to obtain a smooth profile of the upper beak, we trace a cubic spline of the upper profile of the beak. This smooth upper beak profile is used for the pairwise comparison of shapes.

The condition and quantity of available specimens allows us to consider only the top profile of the upper beak for three individuals from each species; this is not restrictive as the upper beak shape reflects the functional biomechanical properties of the entire bill[105] and upper beak shape diversity is highly predictive of the complete three dimensional diversity. To determine whether two given (upper) beak shapes $y_1(x)$ and $y_2(x)$ represent the same shape under a given transformation, we let $T_{s_L,s_H}(y_2)$ denote the transformed shape, rescaled by s_L along the length and by s_H along the height dimension, and compute two metrics quantifying the difference in their shape $E_s(s_L, s_H) = y_1 - T_{s_L,s_H}(y_2)$ and their derivative profile $E_d(s_L, s_H) = y_1' - T_{s_L,s_H}(y_2')$[31]. If there is a global minimum in E_s and E_d for a given set of s_L^* and s_H^*, then the values of E_s^* and E_d^* (the residuals) measure how closely the two shapes $y_1(x)$ and $y_2(x)$ are related by scaling transformations. The two metrics E_s and E_d for two real valued functions

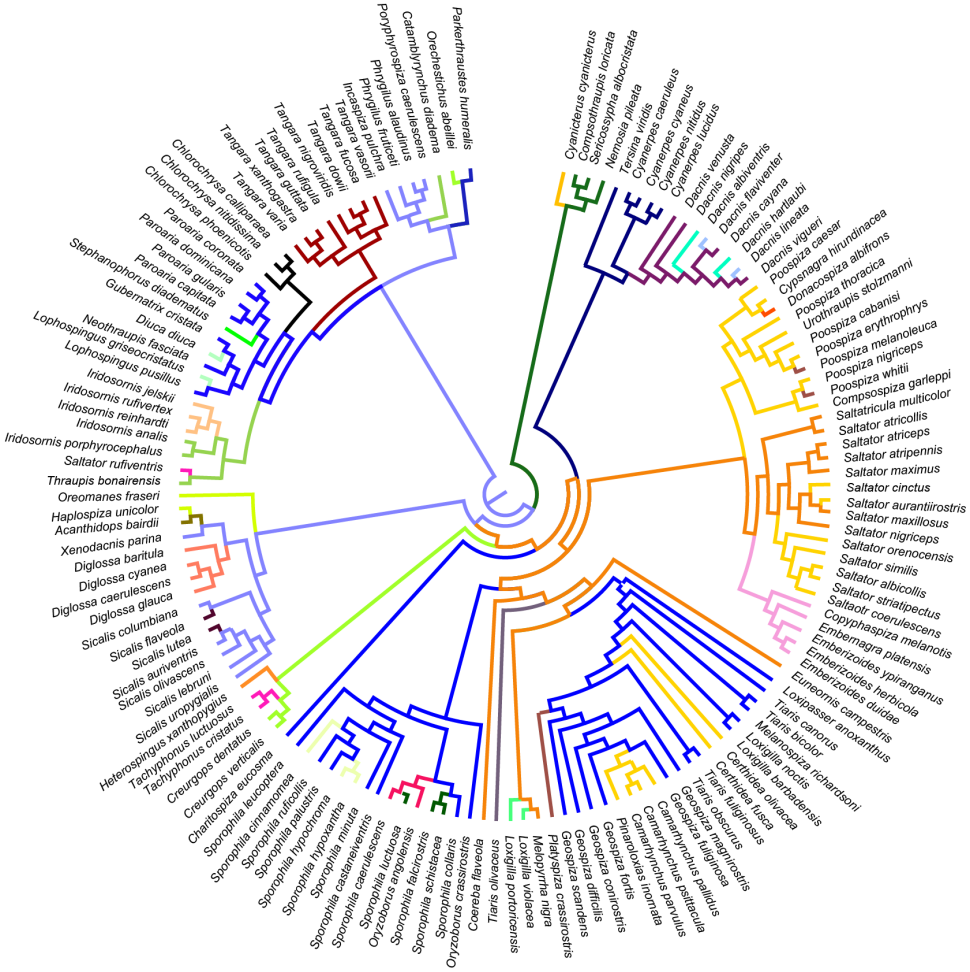

Figure 2.1.1: The phylogenetic structure of beak shapes. Maximum likelihood phylogeny of Thraupidae, indicating diversification of beak shape across the phylogenetic history of the group. Colors represent group shapes of beaks mapped onto the phylogeny using maximum likelihood. Species in the same color collapse onto each other with scaling alone, all shapes collapse under shear.

y_1 and y_2 are defined as

$$E_s = \frac{\int_0^{x_m} \left(y_1(x) - T_{s_L,s_H}[y_2(x)]\right)^2 dx}{\int_0^{x_m} \left(y_1(x) + T_{s_L,s_H}[y_2(x)]\right)^2 dx} \tag{2.1}$$

and

$$E_d = \frac{\int_0^{x_m} \left(y_1'(x) - T_{s_L,s_H}[y_2'(x)]\right)^2 dx}{\int_0^{x_m} \left(y_1'(x) + T_{s_L,s_H}[y_2'(x)]\right)^2 dx} \tag{2.2}$$

where x_m is the endpoint of the beak and $T_{s_L,s_H}[\cdot]$ corresponds to a scaling transformation with scaling factors s_L and s_H in the length and depth directions, respectively. The defined measures are dimensionless quantities that depend only on the two scaling factors s_L and s_H. A necessary condition for two given beak shapes to be related through a scaling transformation is the existence of a minimum of both defined measures, E_s and E_d, for particular values s_L^* and s_H^* of the scaling factors. In order for the reference and transformed shapes to collapse, landmark points in one shape must also be mapped onto the same landmark points of the other shape. In particular, the beak tip and end point of the beak of the reference shape should coincide with the beak tip and end point in the collapsed shape. This effectively restricts the space of s_L and s_H that we are allowed to search for a minimum.

Fig. 2.1.2B shows a heat map of the residuals for these pairwise comparisons, with the different species clustered according to their similarity in beak shape. The heat map clearly identifies 34 morphological groups, represented by colors, within which the beak shapes differ only by their scales. Scaling transformations thus account for a substantial part of the variation observed in songbird beak shapes by reducing the complexity from 145 original beak shapes to 34 different (group) shapes. If we extend the space of transformations to include shear along the length dimension, then in fact all songbird beaks collapse, as shown in the heat map in Fig. 2.1.2C. That is, all songbird beak shapes can be mapped exactly (within the precision provided by modern digital cameras) onto each other under scaling and shear, characterized by precisely three parameters: the height

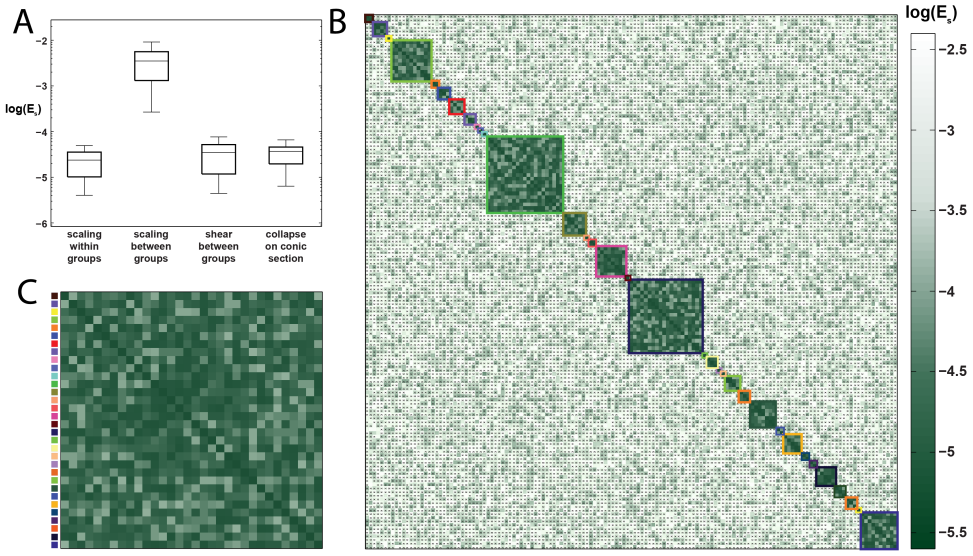

Figure 2.1.2: The hierarchical collapse of beak shapes onto each other under scaling and shear. (A) Quality of collapse (in terms of E_s) for the different levels of similarity presented in Fig. 2.1.3. Note that the quality of scaling within groups, shear between groups and collapse of all beak shapes on conic sections is on the same order of magnitude as our precision of measurement for beak shapes (set by the resolution of modern digital cameras). (B) Heat map of Es resulting from all pairwise comparisons of all beak shapes in the phylogeny from scaling one beak shape onto another. Crosses (X) indicate pairs of species whose beaks do not collapse via scaling transformations, as there was no minimum in E_s as a function of the scaling factors. The species that correspond to the different rows are listed in appendix A. Note the large blocks where the residual is small – these are the scaling groups. (C) Residuals for the collapse of the different scaling groups found in (B) when rescaled using shear transformations. The colors of the rows correspond to the block colors in (B). Note the magnitude of the residuals upon shear collapse are similar to those for the scaling groups.

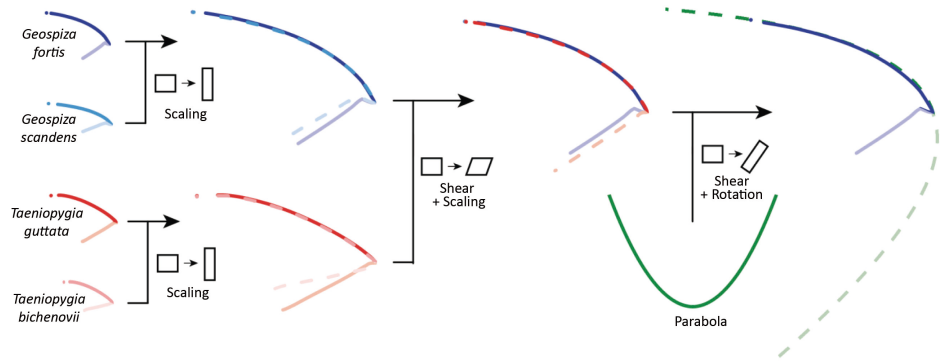

Figure 2.1.3: The basic pattern of beak shape diversity presented here. On small phylogenetic scales, beak shapes collapse under scaling alone (e.g. the two *Geospiza* species on the top left), creating groups of highly similar beak shapes (represented by colors). These group shapes in turn collapse onto each other under shear in their length direction. Specifically, all group shapes collapse onto the shape of the blue colored group. This blue colored group can be approximated to an extremely high precision as a section of a parabola, as shown on the right. The combination of this hierarchical collapse under scaling and shear onto the blue colored group, and the collapse of the blue colored group on a parabola lead to the conclusion that all beak shapes considered here are conic sections.

and length (s_L and s_H respectively) for the scaling transformation and an additional parameter τ measuring the degree of shear. This pattern of hierarchical collapse of shapes is represented in Fig. 2.1.3.

How surprising is this pattern represented in Fig. 2.1.3? This strongly depends on how easily two curves in 2 dimensions can be mapped onto each other. This question has been studied in detail in Invariant Theory, which is most developed for polynomial functions. So to further quantify the diversity of shapes, we fit polynomial functions to the beak profiles, and search for the beak shape with the simplest functional form. This turns out to be *Geospiza* in the Darwin's finches, which are fit well to within the error of our methods for recording shapes by a parabola $y = ax^2 + bx$. The shear collapse of all other songbird beaks onto this shape implies that all beak profiles are well fit by this equation after sending

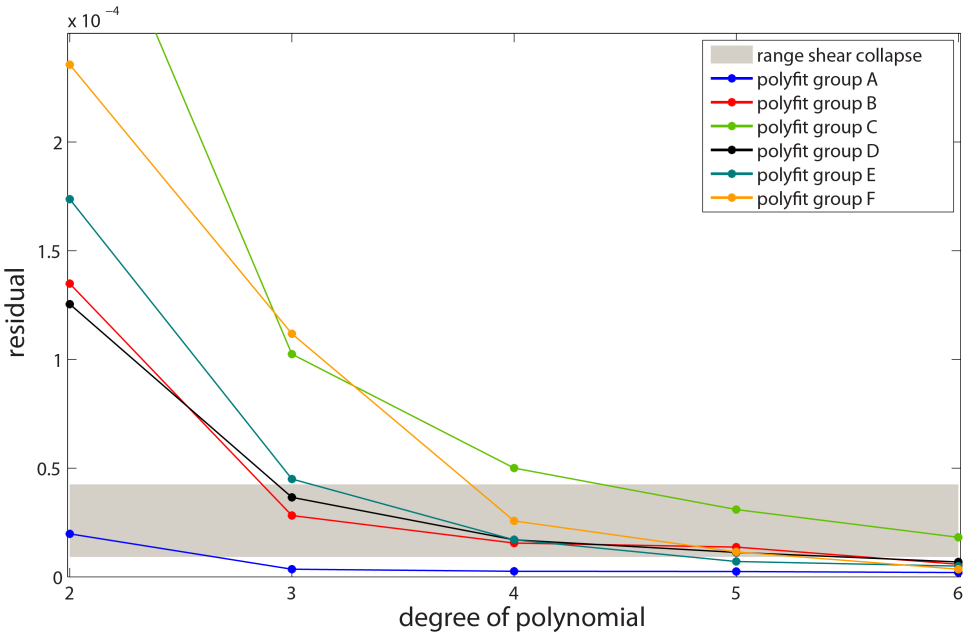

Figure 2.1.4: Polynomial fits for a selection of group shapes as defined in the text. In general, polynomials of degree 6 are necessary to approximate the beak shapes of all songbirds to accuracy comparable to our precision of measurement (gray band). However, the blue group A can be well approximated by a parabola.

$x \to s_l x + \tau y$ and $y \to s_H y$. Thus all beak shapes are well fit by an equation of the form

$$0 = Ax^2 + Bxy + cy^2 + Dx + Ey. \tag{2.3}$$

The midsagittal sections of songbird beaks investigated here are all *conic sections*.

2.2 Flexibility between shape and aspects of developmental program

The role that genes play during development is key to understanding evolutionary processes that generate morphological diversity[35, 47, 56]. Thus the most likely candidate to explain the pattern observed above would be that

species with shapes that collapse under scaling might share the same molecular and developmental mechanism, and different groups are generated by a change in the genes that control the developmental mechanism. Initial evidence confirming this theory comes from experiments on Darwin's Finches. In Darwin's finches of the monophyletic genus *Geospiza*, which all belong to morphological group A (see previous chapter), beaks are patterned by a common underlying molecular and developmental mechanism [1, 2, 76]. At early embryonic stages (stages 26 and 27), Bmp4 and calmodulin (CaM) regulate the growth of the prenasal cartilage (pnc) skeleton [1, 2]. Subsequently, the pnc ceases its expansion [53], and beak morphogenesis is completed by the developing premaxillary bone (pmx), which forms from a separate condensation and is patterned by a network of unrelated yet interacting regulatory genes, TGFβIIr, β-catenin, and Dkk3 [76] at the later stages 28–31. Differences in scaling between species arise through changes in the signaling pathways that alter the pnc and the pmx, the two separate developmental modules that form the beak, along different axes of growth [1, 2, 76]. However, it is unknown whether this mechanism is unique to Geospiza or is also responsible for generating scaling variations and novel beak shapes in other bird species.

We hypothesized that the previously discovered mechanisms controlling beak diversity in Darwin's finches would explain similar beak shapes in other more distantly related bird species. To address this hypothesis, we capitalize on the remarkable beak shape variation in the 13 species most closely related to Darwin's finches [21, 29, 68]. Together with Darwin's finches, these birds, which are mainly endemic to the Caribbean islands, form a monophyletic and recently diverged clade known as the Tholospiza, the "dome finches," because its members build dome-shaped nests with side entrances [29]. Despite high genetic similarity, the Tholospiza have extraordinary levels of beak diversity that are comparable to those seen among members of disparate bird families on mainland [22, 29]. The marked beak diversity of Tholospiza could be explained by ecological factors, such as strong selection pressures upon colonization of specific

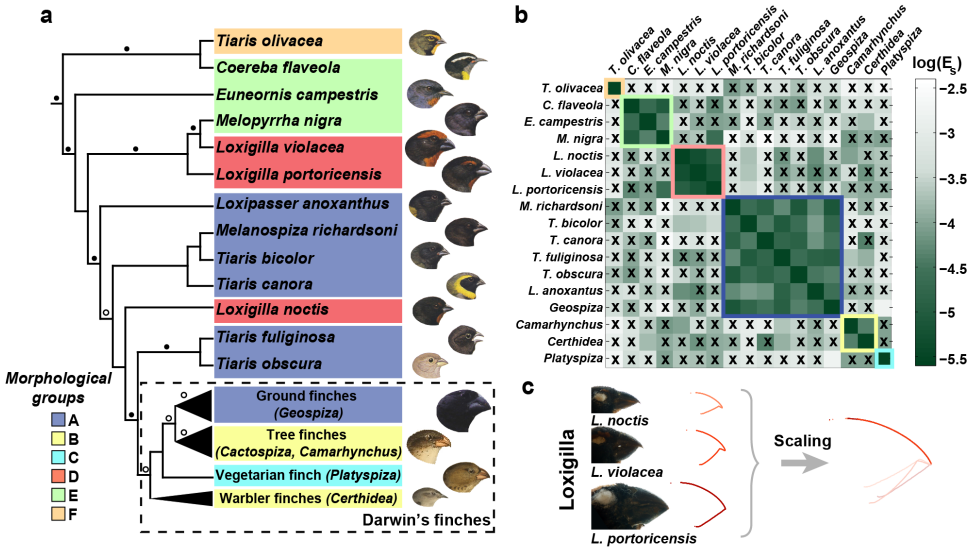

Figure 2.2.1: Tholospiza phylogeny and classification of beak shapes. (A) Maximum Likelihood phylogeny of Tholospiza based on six genes. For Darwin's finches, we show the summarized results from the detailed beak shape analysis that was done previously [31]. Bird illustrations were reproduced with permission from ref. [91]. (B) Heat map of pairwise comparisons between different beak shapes of species in Tholospiza. Crosses (x) indicate pairs where no minimum in the defined measures of shape difference, E_s and E_d, as a function of the scaling factors could be found. The plotted color represents the residual of the shape difference measure, $E_s(s_L, s_H)$. Two beak shapes collapse under scaling transformation if a minimum in both measures describing the difference between the shapes exists (no x) and the associated residual is low (dark green). Morphological groups, defined as groups of species where the beaks of all its members collapse onto each other under scaling transformations (and differ thus only by their scales, such as depth and length), are outlined in the phylogeny and in the heat map with colors. (C) Beak profiles of the three Loxigilla species as obtained from digitization of the beak profile (Left) and after being collapsed onto a common shape by nonuniform (anisotropic) scaling transformations (Right).

island niches, by unique aspects about the beak developmental genetic architecture of its ancestor, or by a combination of both [29].

The morphological analysis in the previous chapter showed that species in the genus Loxigilla, which form part of the Tholospiza, have evolved beaks of the same shape, different from that of *Geospiza*, varying among each other only in scaling. However, in contrast to *Geospiza*, *Loxigilla* species achieve identical beak shapes through distinct signaling pathways and tissues. In one species, beaks are patterned by the same mechanisms as in *Geospiza*, whereas the other two species use different signaling pathways and tissues. Overall, these results demonstrate flexibility between developmental mechanisms and morphology among the closely related members of Tholospiza.

To study in detail the developmental mechanisms that generate novel shapes and the variation within them, we chose to focus on beak morphogenesis in the Caribbean bullfinches of the genus *Loxigilla* (*Loxigilla noctis*, *Loxigilla violacea*, and *Loxigilla portoricensis*) for three reasons: (i) *Loxigilla* species (group D) have deep and wide conical seed-eating beaks that resemble those of *Geospiza* (group A) and thus the comparison of the developmental mechanisms of both groups has a relevant ecological context; (ii) distribution of their beak morphology (*L. noctis* has proportionally the least deep/wide beak, *L. violacea* an intermediately scaled beak, and *L. portoricensis* has the largest and deepest beak) [21] allows for analyzing the mechanisms originating scaling variation within this morphological group (Fig. 1C); and (iii) our beak shape analysis and the phylogenetic evidence from this and a previous study [29] shows that, although *L. noctis*, *L. violacea*, and *L. portoricensis* have been traditionally grouped under the same genus based on similarities in plumage coloration and beak characters [21], their beak shape has evolved convergently (Fig. 2.2.1), with *L. noctis* more closely related to Darwin's finches than to the other two species of *Loxigilla*. Therefore, these birds are ideal to further investigate the principles of beak evolution, such as presence of possible developmental constraints in shape patterning.

Experiments[77] show that a set of different signaling pathways and developmental mechanisms, involving different tissues (cartilage and bone), can

be associated with identical beak shapes varying only in scaling dimensions. Specifically, the beak developmental program in *L. noctis* is similar to that of Darwin's finches of the genus *Geospiza* [1, 2, 76], with a marked contribution from two developmental modules: the pnc, shaped by Bmp4 and CaM signaling, followed by the pmx, regulated by TGFβIIr, β-catenin, and Dkk3 signaling. In contrast, in *L. violacea* and *L. portoricensis*, the contribution of the pnc to beak shape is negligible. Instead, beak patterning in these species is established by a single developmental module through a mechanism in which Ihh and Bmp4, two regulatory molecules that interfere with normal dermal bone development when up-regulated individually, synergize to promote expansion of pmx. It is worth pointing out that the gene expression differences seen in *Loxigilla* demonstrate formally that underlying developmental programs are different, whereas our functional experiments in chicken embryos serve to reinforce the conclusion that such differences, when mimicked in another bird system, can lead to variation in beak patterning and morphogenesis. The use of chicken embryos for functional tests assumes that the developmental gene toolkit for craniofacial morphogenesis and skeletogenesis is largely conserved in all birds, and indeed all vertebrates. For example, most of the known functions for molecules such as Ihh and Bmp4 come from studies on both chick and mouse embryos [67, 92, 103, 106]. In fact, similar craniofacial mechanisms have been observed in groups as disparate as fishes and birds (e.g., Bmp4 plays a role in deep/ strong jaw morphology in cichlids) [3]. However, only functional experiments performed in *Geospiza* and *Loxigilla* will determine with certainty whether the genes examined here cause the species-specific morphologies.

We have shown that different developmental pathways can be involved in development of the same beak shape.

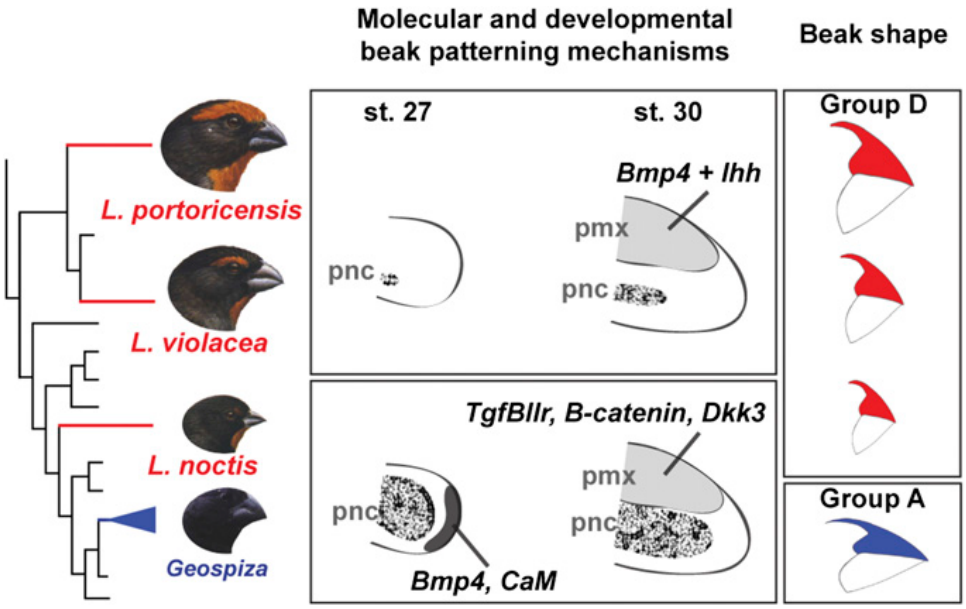

Figure 2.2.2: Different developmental mechanisms (signaling pathways and tissues) can generate beaks of the same shape, whereas beaks of different shapes can be generated by the same developmental mechanisms. In *L. noctis* and in *Geospiza* [1, 2, 76], beak morphology is formed by two developmental modules: first by the pnc, through the action of Bmp4 and CaM signaling, and then by the pmx, through the action of TGFβIIr, β-catenin, and Dkk3 signaling. In *L. violacea* and *L. portoricensis*, Bmp4 and Ihh signaling promote expansion of the pmx, which is the main developmental module responsible for shaping beak morphology. Despite these differences in signaling pathways and tissues, the three *Loxigilla* species have independently evolved a common beak shape (group D), which varies only in scaling and is different from that of *Geospiza* (group A). Branch lengths have been altered to highlight the species analyzed.

2.3 Constraints on growth zone dynamics

The size and shape of the growing beak is completely determined from information stored within the neural crest cells, and not determined by complex external feedback mechanisms, as transplantation experiments in quails and ducks have shown. If neural crest cells from a quail embryo are transplanted into the beak primordium of a duck embryo, the resulting beak looks quail-like, reflecting the origin of the neural crest cells [100], and vise versa. Beak shape is also to some extent independent of the tissue used to pattern the beak. Experiments in *Loxigilla* have shown that while all species within the genus have the same beak shape up to scales, the beak of L. noctis is patterned by pnc, whose growth is regulated by Bmp4, whereas the beaks of other species in the genus, like L. violacea or L. portoricensis are patterned by pmx which is controlled primarily by Ihh. That is species with differing developmental programs, and using different tissue modules to pattern the beak, can grow beaks with identical shapes [76]. The expression patterns of morphogens controlling these processes are most prominent in small regions, close to the tip of the growing beak [2], and EdU staining results in chicken embryos show that this is also the main region of cell proliferation, with only limited cell divisions in the rest of the beak primordium [120].

This mode of growth can be modeled by considering a relatively simple scenario: the induction by morphogens generates a group of dividing cells localized near the rostral tip of the growing beak, the highly defined growth zone. This group of cells changes its shape, size and position as the beak grows. We can describe the shape of the growth zone by the solution to $G(\eta, \xi) = 0$, where $\eta = (x - x_0(t))/l(t)$, and $\xi = (y - y_0(t))/l(t)$. Here (x_0,y_0) are the locations of the center of the growth zone and $l(t)$ is the size of the zone. With this definition, the final shape of the beak is essentially given by the envelope of the growth zone over time, if cell rearrangement during growth is not significant. The envelope for these growth zone shapes is given by $\partial_t G = 0$.

Using this framework, we can ask what the observed invariances from our

analysis of beak shapes imply about the growth process. Under which conditions do these laws have solutions that can only be Eqn (2.3)? To understand this, we note that the most prominent feature of bird beaks is their sharp tip, which requires the size of the growth zone $l(t)$ to shrink to size zero in finite time. We can produce shapes that are conic sections by choosing the growth zones to be homogeneous functions of time, namely $x_0(t) = a(t^* - t)^q$, $y_0(t) = \beta(t^* - t)^q$ and $l(t) = \gamma(t^* - t)^p$, where t^* is the time when beak growth ends. Different scaling groups of beak shapes can then naturally be generated by modifying the prefactors a,β and γ for the same exponents p and q.

Given these laws for the size and movement of the growth zone, the envelope for any polynomial function in η and ξ will simultaneously obey $G(\eta, \xi) = 0$, and $\partial_t G = 0$, or

$$\eta G_\eta + \xi G_\xi = -\Lambda_\xi G_\xi + \Lambda_\eta G_\eta, \tag{2.4}$$

where $\Lambda_\xi = \frac{\beta}{\gamma}\frac{q}{p}$ and $\Lambda_\eta = \frac{a}{\gamma}\frac{q}{p}$. If G is a polynomial of degree n, then Eqn. (2.4) is a polynomial of degree $n-1$. Bezout's Theorem then implies that the system has at most $n(n-1)$ solutions of the form

$$\eta = \Gamma_1, \Gamma_2, , \Gamma_n(n-1) = \Gamma(a, \beta, \gamma, p, q) \tag{2.5}$$

$$\xi = \Theta_1, \Theta_2, , \Theta_n(n-1) = \Theta(a, \beta, \gamma, p, q) \tag{2.6}$$

where Γ, Θ are constants, if a, β, γ, p, q are chosen. We can express these solutions in terms of the original variables as e.g.

$$x - x_0(t) = \Gamma_1 l(t) \tag{2.7}$$

$$y - y_0(t) = \Theta_1 l(t) \tag{2.8}$$

which can be subtracted to yield

$$\beta x - a y = (\Gamma_1 - \Theta_1) t^q \tag{2.9}$$

and plugging this expression back into (2.4) yields

$$x - A(\tilde{\alpha}x - \alpha y)^{p/q} = B(\tilde{\alpha}x - \alpha y). \tag{2.10}$$

where $A, B = f(\alpha, \beta, \gamma, p, q)$. This demonstrates that the envelopes of growth zones are exactly conic sections in agreement with equation (2.3) only for scaling exponents $p/q = 2$. Only a very small class of developmental laws for the growth zone allow the resulting beak shapes to be only conical sections.

These dynamics must be satisfied individually for both the upper and lower profile of a midsagittal beak section. Even for a single profile the invariance of beak shapes sets the exponents of the power laws (p and q) and the precise shape of the profile forces values for all other parameters (α, β and γ). Since the required values for these parameters will generally be slightly different for the upper and lower profile, both can only be satisfied simultaneously if we allow for an additional degree of freedom in allowing the shape of the growth zone to be anisotropic. Our calculations show that only a small set of fixed growth zone shapes can simultaneously generate a given combination of upper and lower profile (see Fig. 2.3.1) while still preserving $p/q = 2$. Under the assumption that the growth zone shape $G(\eta, \xi) = 0$ is preserved in time, we find a one parameter family of growth zone shapes that are consistent with a given upper and lower beak profile. Thus the observation that the beak profiles of songbirds are conic sections not only precisely fixes the dynamics of the growth zone development, but also strongly constrains its potential shape at each embryonic phase.

2.4 Experimental verification

Based on the theoretical results derived above, any universal law for the growth zone dynamics satisfying $p/q = 2$ could generate the patterns of beak shape diversity observed in nature. The simplest scenario has $p = 1$, which corresponds to the location of the center of the growth zone moving with constant velocity. This would occur if the division rate of cells within the growth zone is constant in

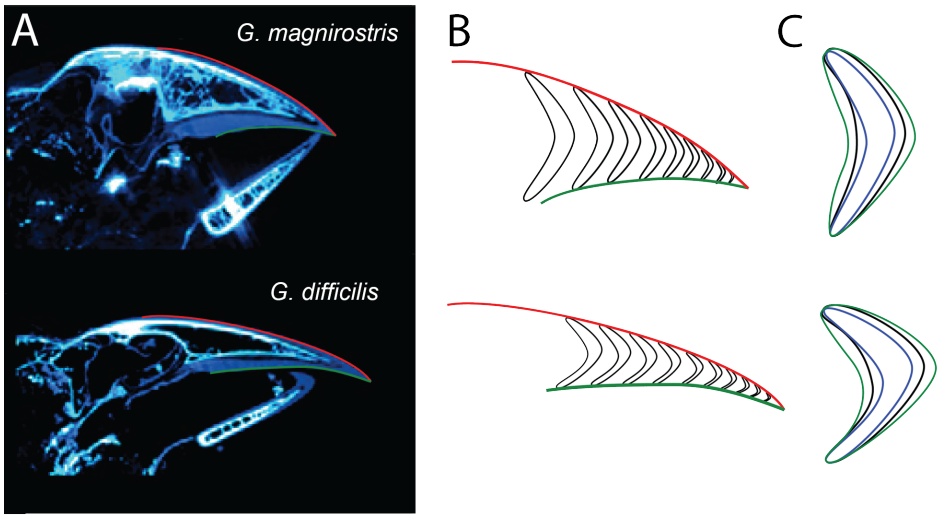

Figure 2.3.1: Prediction of growth zone shape and dynamics, based only on final beak morphology. (A) Midsagittal cuts of beaks for G.magnirosteris and G. difficilus, from Darwin's finches. (B) Red lines show digitized upper shape of the beaks and green lines show lower shape of the beaks. The black curves are growth zone shapes that simultaneously produce the upper and lower beak shapes, as computed from the Monte Carlo procedure described here. The only assumption is that the shape of the growth zone only changes due to change in its center and scale, according to the scaling laws uncovered in the main text. Note that this makes precise predictions for the shape of the developing beak. (C) There is a one parameter family of growth zone shapes (shown in green, black and blue outline) that are able to generate the beak shapes shown in (B). These growth zone shapes vary only in their initial area.

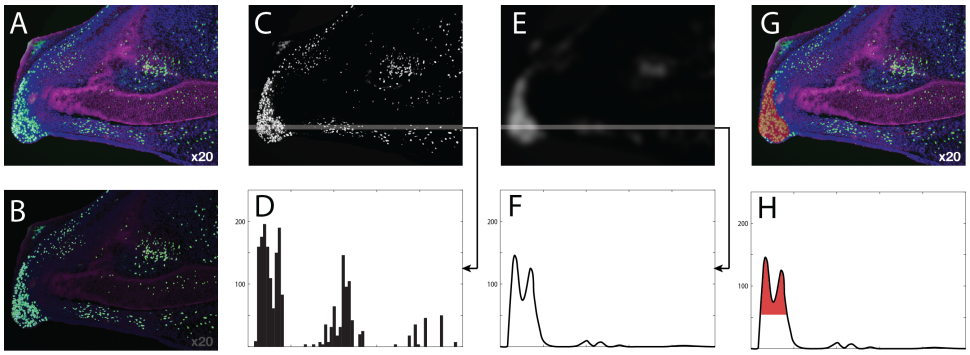

Figure 2.4.1: Measurement and definition of the "growth zone" of proliferating cells in the growing beak. (A) A superposition of EdU and col2 staining for the midsagital section of a developing beak. (B) By extracting the color component of the EdU staining, cells that are dividing can be separated from the background. (C) A thresholded binary image showing the data presented in (B). Note the bright cluster of cells near the tip of the beak where the proliferation zone is situated. A robust and reproducible definition of the growth zone based on this data is however complicated, since the system is very noisy. (D) shows the average brightness of pixels in the small slice highlighted in (C), with a binning of approximately 5 times the average cell size, highlighting the high level of noise. To circumvent this problem, we smooth the data with a Gaussian Filter of radius 20 times the average cell size (E). This creates a continuous brightness profile, with the growth zone well separated and distinguishable from the uniform proliferation everywhere else in the tissue (F). Applying another threshold to the data, allows us to define the growth zone precisely (G,H).

time, and the center of the growth zone is pushed forward by the dividing cells. With $p = 1$, we must have $q = 1/2$, which implies that the largest dimension of the growth zone decreases to zero as $t^{1/2}$.

We test these predictions by measuring the size and position of the growth zone in embryos of zebra finch (*T. guttata*), since their adult beak shape collapses under scaling and shear onto the Geospiza shape (see Fig 2.1.3). We analyze midsagittal sections of the upper beak from stage E5 (embryonic day 5), when the growth zone can first be clearly delineated at the rostral tip of the developing beak, to E9, when the growth zone is no longer visible. All sections are stained to

show dividing cells (with injection of EdU cell proliferation marker, shown green) as well as cell nuclei (blue) and either cartilage precursor (with PNA, shown magenta) or established cartilage (with Col2, shown magenta). The growth zone is clearly identifiable as a concentrated region of dividing cells close to the tip of the developing beak (see Fig. 2.4.2A). We use a simple filter and thresholding method to determine the size of the growth zone at these different developmental stages (see Fig. 2.4.2). Fig. 2.4.2B shows that the largest dimension scales with the expected $t^{1/2}$ dependence on time ($q = 0.48 \pm 0.18$), as predicted by the theoretical framework.

Comparisons between different tissue sections at the same developmental stage indicate that the distance of the growth zone to the region where upper and lower beak meet is very uniform. This distance is, therefore, a good measure for determining the speed with which the growth zone advances relative to a fixed point outside the developmental module. For each growth zone as determined above, we find its centroid, and measure the distance from the meeting point between upper and lower beak and this centroid. Fig. 2.4.2C shows the results of this analysis, which demonstrate that the speed of advance for the growth zone is indeed linear ($p = 0.98 \pm 0.25$) and thus $p/q = 1.87 \pm 0.32$ based on these experimental results, which agrees well with the theoretically predicted value of $p/q = 2$.

Under the assumption that the growth zone shape does not change, our theoretical analysis predicts the growth zone shape from the shapes of the upper beak (Fig. 2.3.1). Intriguingly, although the predicted and observed shapes are similar, the observed shape changes in time as beak develops. The set of time-dependent growth zone shapes that lead to a given beak shape is also strongly restricted, though allowing time dependence clearly gives a larger class of possible solutions. The choice of growth zone shape depends on the developmental rules for encoding the temporal dynamics of cell proliferation.

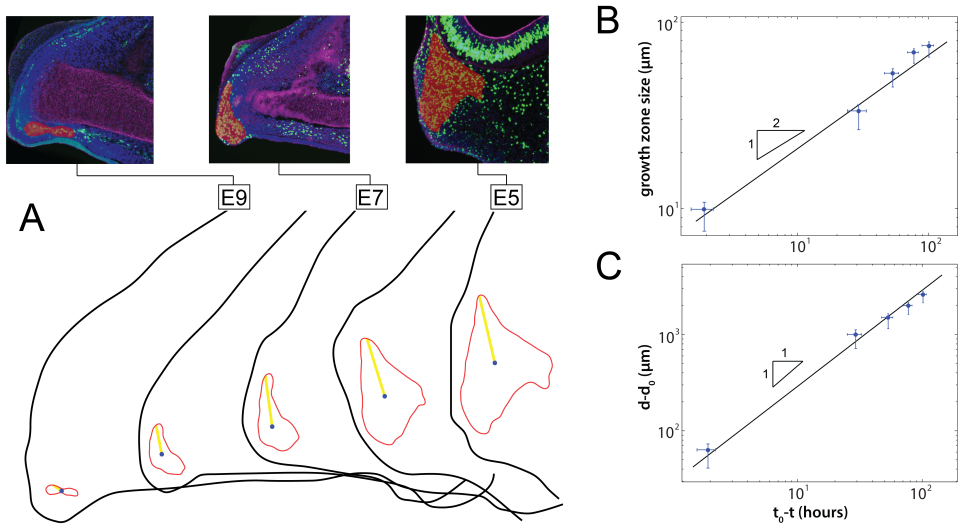

Figure 2.4.2: Experiment testing the time development of the growth zone in developing zebra finch embryo beaks. (A) Snapshots of growing beak for stages E5 to E9, showing its outline (black), the size of the growth zone (red), its centroid (blue) and the relevant length scale for shaping the upper beak profile (yellow). All measures of the growth zone are derived from midsagittal cross sections of zebra finch embryo beaks, stained to show cell nuclei (in blue) and dividing cells (in green). Areas with a high density of dividing cells are defined as the growth zone (red overlay). (B) The dimension of the growth shrinks as $(t^* - t)^{1/2}$, consistent with theoretical predictions. (C) The distance $d - d_o$ of the center of the growth zone from the point where upper and lower beak meet increases as $(t^* - t)$, consistent with theoretical prediction.

2.5 Summary

We demonstrated that the shapes of songbird beaks are accurately represented as a three dimensional subset of conic sections; this is only a small part of the possible morphological parameter space that the shapes of bird beaks could occupy. We demonstrated a direct connection between the shape of a developing beak and the dynamics of the growth zone that shapes it. This suggests that there are also strong constraints on growth zone dynamics by regulatory processes that can be investigated more directly in future experiments.

Our growth model only considers early times in the development of the embryo, up to about HH stage 34. At this point, the shape of the beak is largely set, which coincides with the disappearance of the growth zone at the rostral tip of the beak. The absolute size of the beak appears to to change through more uniform cell proliferation into the late stages of embryogenesis and beyond. However, most results indicate that the shape modulo size is largely unaffected by these processes [46].

In summary, the adaptive significance of beak shapes has been an area of much interest in the literature, with many authors hypothesizing that a bird beak shape is at least partly optimized for feeding and foraging behaviors [102, 105] and vocal song structure [83]. The present study limits the potential set of parameters that can be optimized, since the developmental pathways place strong constraints on the set of beak shapes that can be actually produced. Any optimization can only occur within the 2 to 3 parameter subspace of shapes that is available to the developmental pathway. These free parameters happen to coincide nearly perfectly with the dimensions (like length and height of the beak) that are traditionally used to quantify beak shape diversity [20, 78], which might be a contributing factor to the success that Darwin's finches have enjoyed as a model system connecting morphology and ecological adaptation. Although this amount of variability can have great functional significance, containing, for example, birds that can crack large and hard seeds, such as the large ground finch *G. magnirostris*, and birds that can forage from flowers, e.g. the cactus finch *G. scandens*, there is

no reason to expect a priori that the set of shapes accessible to the developmental programs should include the biomechanics optima.

The process of the highly controlled decay of the growth zone strongly suggests the presence of constrained upstream molecular mechanisms. The nature of such robust developmental constraints is currently unknown but is likely dependent on the interactions of diffusible morphogens with the competent cells within the growing beak skeletal condensations, e.g. cell proliferation-controlled decay in the effective release of the morphogen from the overlying facial ectoderm or feedback loops in the morphogenetic mechanism that gradually shut off the signal and/or signal response [39, 69, 98]. Future research should investigate precise controls of the beak growth zone dynamics in multiple bird species with differently shaped beaks to explain the ultimate principles of beak shape evolution.

Orgel's Second Rule:
Evolution is cleverer than you are.

Francis Crick

3

Boundary layer escape and the ascomycete spore shooting mechanism

Spore dispersal is the primary determining factor for the range and distribution of fungi in nature. The importance of understanding this process in detail has been highlighted in recent years by an unprecedented number of fungal diseases, which have caused some of the most severe die-offs and extinctions ever witnessed in wild species [43], and are increasingly considered a worldwide threat to food security [82]. An effective control of these emerging diseases is only possible if we can understand and control how they propagate.

The defining feature of the largest fungal phylum, Ascomycota, is the ascus, a fluid filled sac from which spores are ejected. Ascus and spore morphologies are highly variable, and have been an essential element of species descriptions for

more than 200 years [13, 72]. Since spores are the primary agents of dispersal, these morphologies also play a critical role in the ascomycete life cycle: most fungi grow on highly heterogeneous landscapes, and to persist a fungus must move between disjoint patches of habitat [60], thus effective dispersal is critical to the fitness of an individual.

To reach dispersive air currents, spores must be launched with enough speed to cross the stagnant air layer around the fungus, the fluid mechanical boundary layer. Although typical boundary layer thicknesses are around 1 millimeter [14], a spore's small size (roughly 10 micrometers) causes rapid deceleration after launch, meaning that it must be launched at very high velocity even to travel a very small distance, and the likelihood of effective dispersal is directly correlated to the thickness of boundary layer that the spore is able to cross [94].

3.1 Crossing the boundary layer

We present a way to parse the startling morphological diversity of spore-shooting apparatuses in the light of this important physical constraint and reveal a critical and previously unsuspected trade-off: the specific feature enabling long distance dispersal of fungal spores, their small size, constrains entry into dispersive air flows. Boundary layer escape provides an important organizing principle for understanding morphological diversity among ascomycetes that shoot their spores.

Fungal sporocarps often form in wind sheltered areas such as under crop or forest canopies, and close to the ground, or on low lying substrates such as plant stems or fallen logs. Air in contact with the ground and the sporocarp must be at rest, and viscous drag between this layer and the flow of air above decelerates a thin layer of air, called the boundary layer. The thickness of the boundary layer depends on whether the air flow above the sporocarp is turbulent or laminar. Air flows at the top of and above the canopy are generally turbulent [119], but the pioneering measurements of near-ground air-flows by Aylor et al. [11] revealed that air flows at the height of a typical *Scelotinia sclerotiorum* sporocarp (height =

3 cm) are slow (U_{wind} = 1-10 cm/s) though highly unsteady. Accordingly we model the dependence of the boundary layer thickness δ upon U_{wind} by the approximate equation:

$$\delta = \sqrt{\frac{\nu L}{U_{wind}}} \tag{3.1}$$

where ν is the kinematic viscosity of the air (equal to the ratio μ/ρ of viscosity, μ, to density, ρ; for air at room temperature, ν=10-5 m^2/sec) and L is the length scale over which air is moving (for example, the span of the sporocarp and the leaf on which it grows). We make two approximations to arrive at equation (3.1):

1. We neglect a coefficient of proportionality that determines the velocity reached at the edge of the boundary layer. In laminar boundary layer theory air-flows only reach the speed U_{wind} infinitely far from the solid surface.

2. We neglect the fluctuations in U_{wind} , doing so requires that the fluctuation time scale exceed L/U_{wind}. Using the data in Aylor et al. [11] (fluctuation time scale 0.6s, $U_{wind} \approx$5 cm/s), we see that this assumption is supported provided that $L < 3$ cm.

Although detailed theories of boundary layer characteristics can be complex [99], the basic physics underlying equation (3.1) is simple: imagine a fluid particle moving in the wind which comes very close to the surface of the sporocarp. The particle slows down dramatically, due to the flow's interaction with the solid surface. This particle can only return to the free stream wind velocity by being jiggled and buffeted by neighboring fluid particles, which also have been slowed down by the fruit body. The jiggling and buffeting causes the motion of the particles to be diffusive, so that the particle will move according to the law

$$y(t) = \sqrt{\nu t} \tag{3.2}$$

where $y(t)$ is the distance that the particle moves away from the fruit body in a time t. Now the total amount of time that it takes for the wind to blow over the

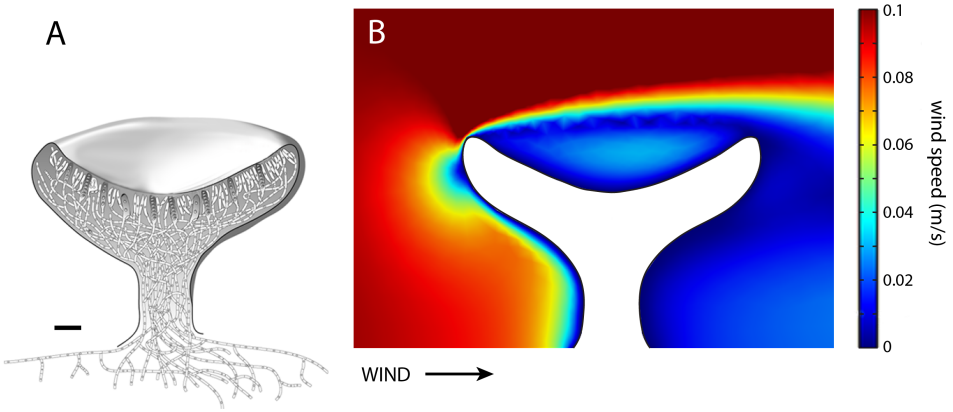

Figure 3.1.1: Boundary layer around a fungal sporocarp.

sporocarp and its substrate of size L is

$$t = L/U_{wind}. \tag{3.3}$$

This is the maximum time the particle has to return to the free stream. Hence, combining Equation (3.3) with Equation (3.2) yields the (maximum) thickness of the boundary layer, Equation (3.1).

Based on this calculation, boundary layers around sporocarps can vary dramatically in thickness, depending on the geometry of the sporocarp and wind speed, but are typically on the order of a few millimeters in thickness; equivalent to hundreds or even thousands of spore lengths.

Mechanisms enabling spores to escape boundary layers are critical to the fitness of individuals. If the range of a spore is less than the thickness of the boundary layer, the spore will fall back on its parent and is unlikely to establish as an independent fungus.

Spores are ejected at enormous speeds (typically 1-20 m/s [121]), but decelerate much more rapidly than macroscopic projectiles. The range of any forcibly ejected body is determined by a balance of forces: the resistance caused by air-drag, causing deceleration, the inertia of the body itself, working to

maintain the body at its original speed, and gravity. Small objects have great difficulty moving through still air because of the different ways resistance and inertia scale with body size. For a spore, resistance stems almost entirely from the viscosity of the air. The viscous force on a spore is directly proportional to its size [42, 85, 118]. So, leaving all other parameters the same, halving the size of a spore halves the total viscous force. On the other hand, the inertial force scales with the spore volume, i.e. is proportional to the cube of its size. Halving the size of a spore reduces its inertia eightfold. Vogel [118] draws an analogy between forcibly ejecting a spore and throwing an air-filled balloon to the other end of a closed room. In both cases, resistance greatly exceeds inertia, causing rapid decelerations, and keeping the effective range of the projectile very low.

If a spore is ejected from the ascus with velocity V_{spore}, it decelerates according to:

$$m\frac{du}{dt} = -\xi v \tag{3.4}$$

which balances the spore's inertia with air drag. In Equation (3.4) ξ is the viscous drag coefficient, linearly proportional to spore size. Equation (3.4) can be solved to find the maximum distance the spore can travel:

$$x = V_{spore}\frac{m}{\xi} \tag{3.5}$$

For the spore to escape the boundary layer, this distance must exceed the boundary layer thickness

$$V_{spore}\frac{m}{\xi} > \sqrt{\frac{\nu L}{U_{wind}}} \tag{3.6}$$

Equation (3.6) is the fundamental constraint for boundary layer escape. It includes three different parameters, V_{spore}, m/ξ, and L that can be manipulated through fungal adaptations to maximize the probability of spore dispersal (Fig. 3.2.1). In what follows, we argue that this constraint provides a logical framework for a unified understanding of the diverse morphologies and

mechanisms of ascomycete spore dispersal: Figure 3.2.1 shows specific adaptations – spore shape, coordinated ejection, apical ring morphology,spore appendages and fruiting body shape – whose characteristics can be quantitatively understood as arising from this constraint. In what follows we will summarize the specific adaptations and mechanisms that arise from this constraint.

3.2 Morphological adaptions for boundary layer escape

3.2.1 The spore ejection velocity V_{spore}

To maximize the probability of boundary layer escape, the initial spore ejection velocity should be as large as possible. The ejection is velocity determined by the chemistries causing an osmotic imbalance and pressure within the ascus, and the various morphologies first maintaining the swollen ascus and then propelling the spore out of the ascus. By equating the spore's kinetic energy to the work done to accelerate the spore we can relate the maximal achievable V_{spore} to the overpressure Δp and spore density ρ_{spore}:

$$V_{spore} = \sqrt{\frac{2\Delta p}{\rho_{spore}}} \tag{3.7}$$

This predicted speed is independent of spore shape and size [93]. Although different species use different osmolytes to create turgor pressure [41], overpressure appears to be broadly conserved at about 0.3 MPa ([41, 110] but see [111]), suggesting most species function at a limit caused by physiological or biomechanical constraints (for example, the strength of the ascus wall).

However, Eqn. (3.7) neglects a critical aspect of spore ejection from the ascus: to prevent too much fluid loss during the ejection of each spore, there must be a tight seal between the spore and ascus during ejection. But the tightness of the seal leads to large friction on the ejected spore, which reduces the real speed of spore ejection from the value predicted by Equation (3.7). In many species, spores are forced through the apical ring, an elastic seal at the tip of the ascus.

This ring functions like an o-rings used by engineers to seal moving pistons. It deforms to accommodate a thin layer of lubricating fluid between the ring and the ejecting spore spore. Doing so requires satisfying two constraints: If the lubricating fluid layer is very thin, fluid friction between the fast moving spore and the stationary ring slows down the spore. If the fluid layer is thicker, this effect is reduced, but more fluid escapes the ascus through the fluid layer and the pressure in the ascus drops. Real asci compromise between these two effects if a relation between the spore size and ring geometry is precisely satisfied. We will investigate this effect in more detail in chapter 3.3.

Equation (3.6) is a physical constraint for the ejection velocity of single spores. However, fungi can get around this by ejecting many spores at once and letting them be dragged in their own wind. The synchronized ejection of hundreds or even hundreds of thousands of spores by discomycete fungi cooperatively creates a jet of air, which enhances spore range by a factor of 10 or more [94].

3.2.2 The mass to drag ratio m/ξ

Physically, m/ξ is the timescale over which an ejected spore will decelerate. If this timescale is large, a spore will decelerate more slowly and travel farther under the impulse of its initial ejection. The ratio is sensitive to spore size: the mass of a spherical spore is $m = 4/3\pi\rho_{spore}a^3$, where a is the spore radius and ρ_{spore} is the density of the spore, while $\xi = 6\pi\mu a$. Thus

$$\frac{m}{\xi} = \frac{2}{9}\frac{a^2}{\nu}\frac{\rho_{spore}}{\rho_{air}} \tag{3.8}$$

A twofold increase in spore radius produces a fourfold increase in range. If we combine Equation (3.6) with Equation (3.8), we obtain a minimum size enabling escape from the boundary layer:

$$a^2 >= \frac{9}{2}\frac{\nu}{V_{spore}}\frac{\rho_{air}}{\rho_{spore}}\sqrt{\frac{\nu L}{U_{wind}}} \tag{3.9}$$

Figure 3.2.2 shows this curve as a function of the wind velocity, with a colored contourmap showing the necessary initial velocity V_{spore} that barely allows boundary layer escape. Note that the size of ascomycete spores are close to the threshold, which is why boundary layer escape is such an important constraint for fungal spores, as opposed to e.g. plant seeds.

To manipulate m/ξ, a species may evolve a number of different adaptations. To increase mass, fungi may evolve very large spores, eject spores as a group, or create mucoid appendages to stick smaller spores together. Temporarily tethering spores with mucous increases their likelihood of entering dispersive air flows, by breaking apart once through the boundary layer, spores can still be carried by weak air flows. A "polyspore" grows as a single larger spore with septa or divisions, and serves the same purpose; polyspory would allow a single large mass to cross the boundary layer and subsequently disassociate into smaller parts [12, 88]. Each of these adapations has evolved independently in multiple ascomycete orders [101]. Equation (3.8) shows the strong dependence of m/ξ upon spore size, which may be constrained by aerodynamics or the limits of maternal investment, spore shape also directly affects m/ξ. The benefits of drag minimization appear, initially negligibly small; unlike large bodies such as cars, for which low drag shapes and spheres may differ in drag by less than a factor of 2, for a typically sized spore. Spores with drag minimizing shapes travel only 5-10 percent farther than equivalently sized spherical spores. However, across the Ascomycota, spore shapes are within 1% of the drag-minimizing optimum [93], suggesting that dispersal effectiveness is associated with strong selective forces upon spore morphology.

3.2.3 Fruiting Body Shape L

The final element of equation (3.6) that fungi can manipulate is the size of the boundary layer itself. *Cordyceps spp.* have extremely long filiform spores, that are often hundreds of times longer than they are wide. A fully extended spore may reach across the boundary layer before its ejection is completed. In aid of this,

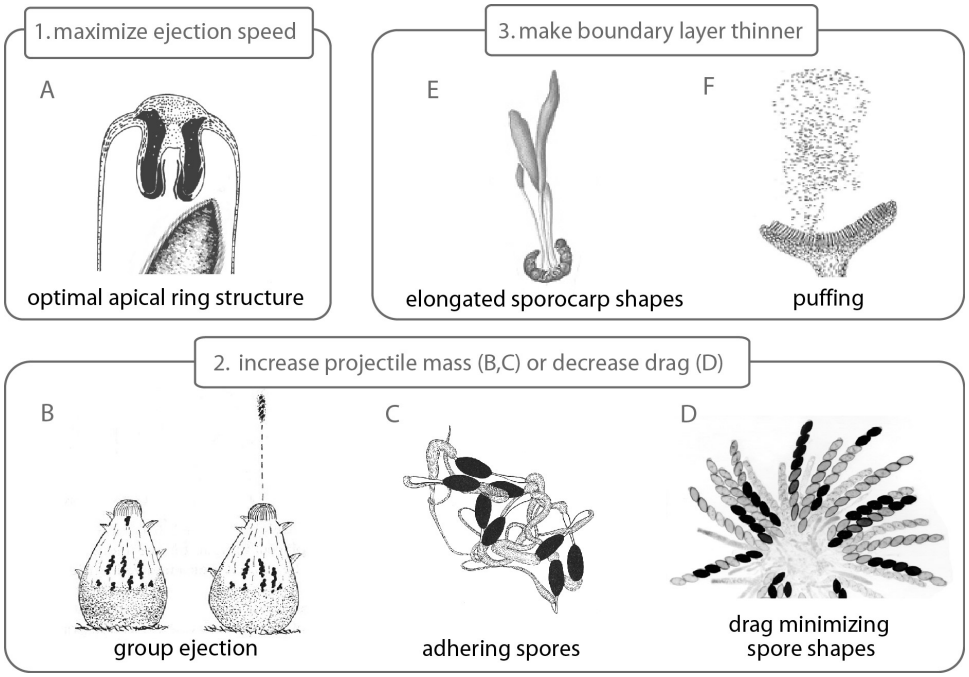

Figure 3.2.1: Overview of morphological adaptions related to boundary layer escape and grouped by different terms of the basic governing equation for this process, Eqn. (3.6).

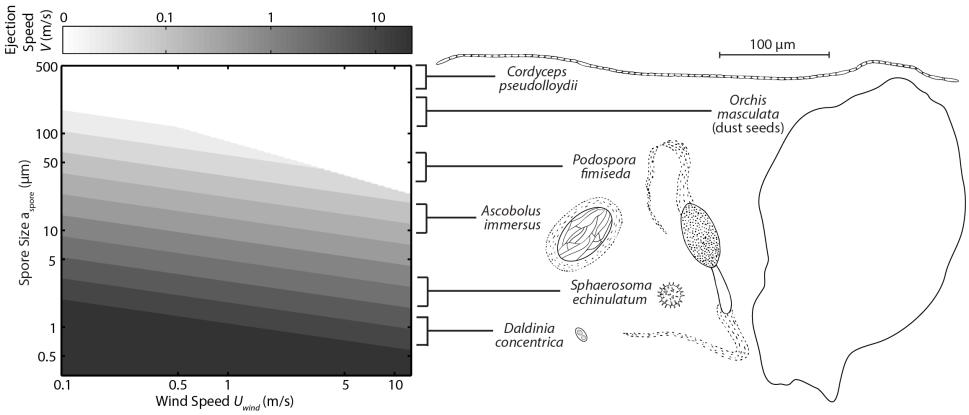

Figure 3.2.2: The speed necessary to escape the boundary layer strongly depends on the size of the spore.

sporocarp geometries that minimize the boundary layer thickness may be favored. Figure 3.1.1 shows the boundary layer thickness for different sporocarp geometries. The smaller the radius of curvature at the top of the ascus (the smaller L), the thinner is the boundary layer. While most other species have sporocarp morphologies that are related to the specific ejection mechanism they use, e.g. disk-like sporocarps allow for puffing dispersal, the sporocarps of *Cordyceps* are very slender with a small radius of curvature at the tip, to minimize the size of the boundary layer.

A species may fruit preferentially on smaller substrates or at sites with greater winds: a plant pathogen might preferentially produce sporocarps on plant stems instead of leaves, or at the tips of protruding or elevated structures. We are unaware of any data which would specifically test this novel hypothesis. For many species, the sporocarp's location will be dictated by the size and exact placement of the parent: epiphytic fungi colonize just a few square mm of a particular leaf [10], while many competing fungi occupy a single pellet of dung [28]. But remarkable adaptations may allow some species to influence sporocarp placement. *Cordyceps* preys on insects, and is known to modify the behaviors of infected ants [40]. Responding to unknown cues from the fungus, ants have been

seen to leave their nests to climb a nearby plant; "grasping the stems with their mandibles before dying in this exposed position" [40]. Since wind speed increases with height from the ground, the climb exposes the emerging sporocarp to higher wind speeds, and a thinner boundary layer.

3.3 Apical rings optimize spore dispersal

In a large number of ascomycete species spore ejection is powered by a buildup of osmotic pressure [110], which forces spores through a ring or hole at the tip of the ascus, after a critical pressure is reached [111]. The critical role of this apical ring in spore dispersal caused speculation about whether the diverse morphologies of the spore ejection apparatus are tuned to allow effective dispersal. Buller proposed a relationship between the dimensions of the apical ring and the size of the spore, ostensibly to prevent spores from tumbling during flight [28]. Ingold thought spores would be shaped to maximize the force used by apical rings to push on them [60]. But, surprisingly, the individual geometric dimensions of apical rings and spores critical to these hypotheses are either very weakly or not correlated.

Here we resolve this discrepancy by demonstrating a strikingly tight coupling between the size of the spore and a nonlinear function of multiple dimensions of the apical ring. The relationship is suggested by physical constraints on spore ejection: the requirement to efficiently convert the potential energy stored in the ascus to kinetic energy of the spore. The apical ring is an elastic seal, and distorts significantly when the spore, which is lubricated by a thin fluid layer, passes through it. The basic physical principles governing this kind of process were discovered fifty years ago, in the study of elastomeric seals and O-rings used to control fluid flow in engines, pipes and other engineering applications [38]. By adapting these theories to the fluid mechanics of spore ejection, we demonstrate that although there are at least 5 independent dimensions to the morphological diversity of spores and apical rings, the need to minimize energy losses during ejection restricts spore and ascus morphologies to a one-dimensional subspace,

where the dimensions of a spore and its apical ring are tightly coupled.

We test this theory using published electron micrographs of apical rings and spores (e.g. [16, 26, 34, 48, 54, 112, 114, 117]) and a recently published ascomycete phylogeny [101], which identifies two potentially independent groups of species with spores singly ejected through apical rings. Quantitative descriptions of spores and apical rings at a high resolution are available for 45 species, with dimensions of the spore and apical ring characters varying over one order of magnitude. Nonetheless, the observed variation is confined to the predicted one-dimensional subspace with surprising accuracy: energy losses are held within two percent of the theoretical optimum.

By assembling data on species where there is no selective pressure to maximize ejection velocity, because spores are dispersed using different mechanisms, for example, insect vectors, we test whether genetics are a constraint on morphology. In fact, these species have very different apical ring and spore shapes, suggesting natural selection is the force maintaining collapse into the one-dimensional subspace for species with functional apical rings.

3.3.1 Optimal lubrication layer thickness

Fig. 3.3.1 shows a representative context in which spore ejection occurs. The sporocarps of a fungus are scattered on a host (e.g. the stalk of a plant, Fig. 3.3.1A). These structures are produced by the fungus with the sole purpose of dispersing the spores. Within each sporocarp, there can be hundreds of asci, each generally containing eight spores (Fig. 3.3.1B). When the spores in an ascus are mature, osmolytes are produced, leading to water influx into the highly elastic ascus, resulting in a significant increase of volume and pressure [111]. When the osmotic pressure p_o inside an ascus is sufficiently high, the spores are singly ejected into the surrounding air.

The speed U at which a spore is launched depends critically on energy losses during ejection. If the osmotic pressure were entirely converted to kinetic energy,

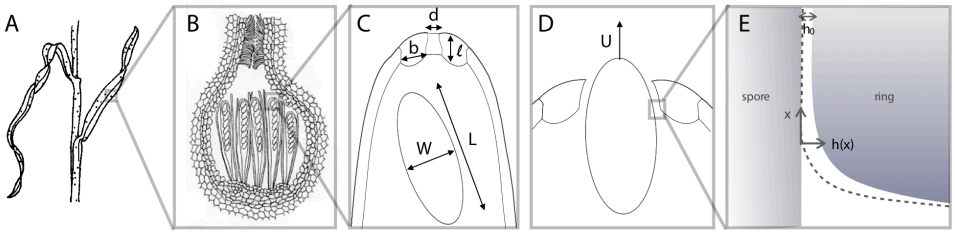

Figure 3.3.1: The spore shooting apparatus. (A) Sporocarps on the stalk of a plant. (B) Flask-shaped sporocarp, containing 5 asci. (C) Upper part of an ascus with a mature spore close to the apical ring, which is still sealed. The length L and width W of the spore and the dimensions of the apical ring (ℓ, b, d) are indicated. (D) Spore moving at velocity U and deforming the apical ring at launch. A lubricating layer of fluid separates the spore from the ring. (E) The region where the spore first deforms the ring. x measures the distance from the point where the spore starts to compress the ring; the gap thickness h varies with x and asymptotes to a constant value h_o at $x > \lambda$ as described in the text. Dashed line: dry contact deformation.

the spore would be ejected at an ideal velocity:

$$U_{ideal} = \sqrt{\frac{2p_o}{\rho_s}} \tag{3.10}$$

where ρ_s is the density of the spore and p_o is the overpressure in the ascus.

However, the ideal launch velocity is necessarily degraded by both friction and fluid loss as the spore moves through the apical ring (Fig. 3.3.1C,D). The apical ring consists of an elastic material with thickness b and height ℓ. The size of the opening of the apical ring before the spore starts to pass through it, d, is much smaller than the width W of the spore. During the ejection of the spore, the apical ring is strongly deformed, and there is a thin layer of fluid with viscosity μ and density ρ, separating the apical ring from the spore.

Energy losses arise from two different processes occurring in this lubricating fluid layer of thickness h_o: first, there is friction between the spore and the apical ring, due to the viscous force in the fluid gap $F \sim W\ell\mu U/h_o$, opposing the motion of the spore moving with velocity U. The total energy dissipated is then $E_{friction} = FL$, the product of this viscous force with the distance that the spore

moves when the force is acting, which is the length L of the spore. The second energy loss arises because the pressure in the ascus, and thus the main accelerating force, decreases while the spore and lubricating fluid leave the ascus. If ascus pressure and volume are proportional, the energy lost due to fluid leaving the ascus is proportional to the kinetic energy, $E_{fluid} = \rho W h_0 L U^2$, up to a constant parameterizing the ratio of ascus volume before ejection to spore volume. If h_0 is large, the energy loss is dominated by the fluid flow through the gap, while if h_0 is small, the energy loss is dominated by friction. The minimal total energy loss $E_l = E_{fluid} + E_{friction}$ occurs if $E_{fluid} \approx E_{friction}$ and thus if the physical gap thickness is close to the optimal value $h_0 = h_*$, with

$$h_* = a\sqrt{\frac{\mu\ell}{\rho U}} = a\frac{(\mu\ell)^{1/2}}{(2\rho p_0)^{1/4}}, \tag{3.11}$$

where in the second equality, we have assumed that the energy dissipation is sufficiently small that $U \approx U_{ideal}$, with $\rho_s \approx \rho$. The proportionality factor $a = 0.45$ can be found by explicitly integrating the equations of motion for the spore, as demonstrated in chapter 3.3.5. Fig. 3.3.3A shows a plot of the energy dissipated as a function of h_0 following from this more complete analysis.

3.3.2 Elastic Deformation of Apical Ring

We model the apical ring as a thick-walled short cylinder of an ideally elastic material in cylindrical coordinates (r, x, θ). This simple model is motivated by the following two observations:

1. The apical ring behaves like an elastic material under internal pressure, with Poisson ratio $1/2$, so that the material is incompressible. While we are not aware of direct measurements of material properties for apical rings, owing to their large water content biological materials are generally nearly incompressible. Comparisons of ring micrographs right before and after ejection (see figure 3.3.2) indicate that the deformation is essentially purely elastic, with only a small plastic component, even after all (usually

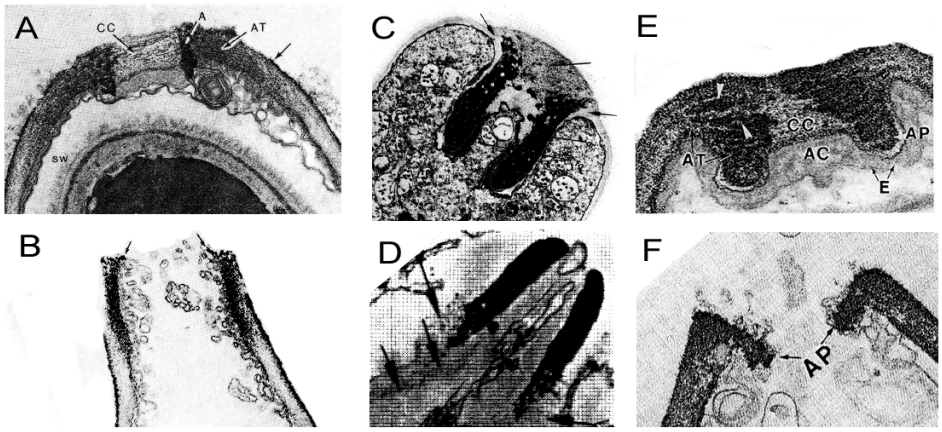

Figure 3.3.2: Comparison of rings before (A,C,E) and after (B,D,F) ejection for *Neobulgaria pura* (A,B) [112], *Xylaria longipes* (C,D) [16] and *Mitrula paludosa* (E,F) [114].

8) spores have been ejected.

2. During ejection, the spore is separated from the ring by a thin layer of lubricating fluid. Due to constraints in resolution in both time and space, this thin lubricating layer between spore and apical ring cannot be easily observed experimentally. However, from engineering applications at similar scales it is well known that this lubricating layer generally exists. Very complicated sealing geometries are needed to eliminate it, none of which occur in the species considered here. A complete removal of the lubricating layer would drastically increase friction between the ring and the spore and thus make spore ejection very difficult.

3. The elastic deformation of the ring is not influenced by the ascus wall during ejection. The reason for this is two-fold. As seen in figure 3.3.2, the ascus wall is, even for the smallest rings, one order of magnitude thinner than the ring. In addition, the ascus wall strongly deforms for pressures on the order of the initial osmotic pressure p_o in the ascus, whereas the ring only deforms for the much larger lubrication pressure. This indicates that

the elastic modulus of the ring is at least an order of magnitude higher than that of the ascus wall. These two factors together imply that the total force transmitted on the ring from the ascus wall (which is slightly deforming during ejection, since ascus volume is decreasing) can be neglected compared to the forces transmitted by the spore passing through the ring. Unfortunately no experimental data on the elastic modulus or other material parameters of either the apical ring or the ascus wall are available to make this argument more quantitative.

The ring has an internal radius r_i, external radius r_o and length ℓ in the x-direction. Our goal is to find the deformation u of the ring as a function of an internal pressure p_r. We will make the classical Lame assumptions:

1. axial-symmetry: u (in the r-direction) is the only displacement component
2. the radial displacement u only depends on the radius r: $u(r, x, \theta) = u(r)$
3. shear stresses on the elementary volume must be zero: $\tau_{xr} = \tau_{x\theta} = \tau_{r\theta} = 0$
4. due to axial-symmetry and the constant thickness $r_o - r_i$ of the ring, the radial and circumferential stresses only depend on the radius r: $\sigma_r(r, x, \theta) = \sigma_r(r), \;\; \sigma_\theta(r, x, \theta) = \sigma_\theta(r)$.
5. the axial stress σ_x is constant along the length of the transverse section (independent of the coordinates x, r): $\frac{\partial \sigma_x}{\partial r} = \frac{\partial \sigma_x}{\partial x} = 0$

We first consider the radial force equilibrium of an infinitesimal element of the ring with the dimensions $dr, dx, d\theta$, keeping only the lowest order terms:

$$\left(\sigma_r + \frac{d\sigma_r}{dr}dr\right)(r + dr)d\theta dx \; - \sigma_r r d\theta dx \; - 2\sigma_\theta dx dr \frac{d\theta}{2} \approx 0$$

$$\Leftrightarrow \sigma_r dr d\theta dx + \frac{d\sigma_r}{dr}dr^2 d\theta dx + \frac{d\sigma_r}{dr} r dr d\theta dx - \sigma_\theta dr d\theta dx \approx 0 \qquad (3.12)$$

Neglecting small products like $(d\sigma_r/dr)dr^2 d\theta dx$ and collecting terms, the above equation reduces to:

$$\frac{d\sigma_r}{dr} + \frac{\sigma_r - \sigma_\theta}{r} = 0 \tag{3.13}$$

We have recovered one equation with two variables $\sigma_r,\ \sigma_\theta$. If the complete stress field $(\sigma_r,\ \sigma x,\ \sigma_\theta)$ in the ring is known, strains and the deformation can be determined easily. To derive two additional equations for these three variables we combine the strain-displacements equations:

$$\varepsilon_r = \frac{du}{dr} \tag{3.14}$$

and

$$\varepsilon_\theta = \frac{2\pi(r+u) - 2\pi r}{2\pi r} = \frac{u}{r} \tag{3.15}$$

with Hooke's generalized law for these strain components:

$$\varepsilon_r = \frac{1}{E}\left[\sigma_r - \nu(\sigma_x + \sigma_\theta)\right] \tag{3.16}$$

and

$$\varepsilon_\theta = \frac{1}{E}\left[\sigma_\theta - \nu(\sigma_r + \sigma_x)\right]. \tag{3.17}$$

Combining Eqns. (3.14) to (3.17) we find

$$\sigma_\theta = \frac{E}{1-\nu^2}\left(\frac{u}{r} + \nu\frac{du}{dr}\right) + \frac{\nu\sigma_x}{1-\nu} \tag{3.18}$$

and

$$\sigma_r = \frac{E}{1-\nu^2}\left(\frac{du}{dr} + \nu\frac{u}{r}\right) + \frac{\nu\sigma_x}{1-\nu}. \tag{3.19}$$

Eqns. (3.13),(3.18),(3.19) give us three equations for the three stress components. By combining these equations we can derive an ODE for $u(r)$

$$\frac{d^2u}{dr^2} + \frac{1}{r}\frac{du}{dr} - \frac{u}{r^2} = 0 \tag{3.20}$$

Integrating twice we find

$$u(r) = C_1 r + \frac{C_2}{r} \tag{3.21}$$

The constants C_1 and C_2 are determined by the boundary conditions of the problem. In our case we will require an overpressure (above atmospheric pressure) of p_r on the inside of the ring. That is

$$\sigma_r(r = r_i) = -p_r \text{ and } \sigma_r(r = r_o) = 0. \tag{3.22}$$

Plugging Eq. (3.21) into (3.19) and comparison with Eq. (3.22) shows that for our case

$$C_1 = \frac{1-\nu}{E}\frac{r_o^2 p_r}{r_i^2 - r_o^2} \text{ and } C_2 = \frac{1-\nu}{E}\frac{r_i^2 r_o^2 p_r}{r_i^2 - r_o^2} \tag{3.23}$$

The most general expression for $u(r)$ is then

$$u(r) = \frac{1+\nu}{E}\frac{r_i^2 p_r}{r_o^2 - r_i^2}\left(1 - 2\nu + \frac{r_o^2}{r^2}\right) r \tag{3.24}$$

which for biomaterials with $\nu \approx 0.5$ simplifies to

$$u(r) = \frac{3}{2E}\frac{p_r r_i^2 r_o^2}{(r_o^2 - r_i^2) r} \tag{3.25}$$

3.3.3 The fluid layer thickness h_o

What physical mechanism determines h_o? During spore ejection, the apical ring undergoes a strong deformation to allow the spore to pass, and this deformation causes a restoring elastic pressure to push against the spore. On the other hand, within the fluid gap there is viscous pressure caused by the fluid motion itself. The fluid layer thickness h_o is determined so that these two pressures exactly balance. The layer thickness h_o thus depends in a nontrivial fashion on all of the parameters of the problem outlined thus far: the dimensions and elastic modulus E of the apical ring, the viscous forces acting in the thin fluid layer, and the size of the spore.

Determining the dependence of the layer thickness h_o on these parameters is a classic problem in elastohydrodynamics, and it was examined in the 1960's to understand the properties of engineering seals, for example O-rings. The theoretical ideas worked out in this context are directly applicable to the present problem, and here we recapitulate the basic arguments [37, 38, 55] in the context of our system. Fig. 3.3.1E shows the geometry of the contact, focusing on the edge of the apical ring where the spore enters from the ascus. The coordinate x parameterizes distance from the entry point, located at $x = 0$. Within the ascus, far from the spore entry point, the pressure is $p \approx p_o$, and the shape of the apical ring is undeformed.

First, it is convenient to consider what would happen if there were no fluid gap ($h_o = 0$), and no flow through the contact. In this case, the elastic distortions and pressures caused by the spore moving through the apical ring follow from Hertzian contact theory. The Hertz contact solution is completely specified by the local radius of curvature $R_* \sim \ell$ of the contact region [1], and the resulting elastic deformation, implying that when $x < 0$, $h(x) = \xi(x/\xi)^{3/2}$, whereas when $x > 0$, the pressure distribution for $x/\xi \lesssim 1$ obeys $p(x) = E\sqrt{x/\xi}$, where $\xi = \ell\sqrt{E/p_r}$ is an elastic healing length. Here, p_r is the elastic pressure exerted by the spore on the apical ring, well inside the contact ($x/\xi \gg 1$). Since the ring deformation is dominated by the spore passing through it, we can neglect the deformation of the ascus wall for the elastohydrodynamic calculation. Under this assumption we can approximate the apical ring as a circular cylinder with internal radius $r_i = d/2$ and outer radius $r_o = d/2 + b$, subject only to an internal pressure p_r. Due to symmetry, the displacement of the ring depends only on the radial distance r from the center line. Classical elasticity theory[73] dictates that the deformation is given by

$$u = \frac{3}{2E}\frac{p_r r_i^2}{r_o^2 - r_i^2}\frac{r_o^2}{r}. \tag{3.26}$$

[1]The local radius of curvature is approximately ℓ as a result of the spore being much larger than the apical ring. We obtain the proportionality constant by data analysis as illustrated in the *ESM*.

With the spore passing through the apical ring, the deformation of the inner surface of the ring is $u(r_i) = W/2$, implying the elastic pressure

$$p_r = \frac{E}{3} W \frac{r_o^2 - r_i^2}{r_i r_o^2} = E_* W \frac{b(d+b)}{d(d+2b)^2} \tag{3.27}$$

where $E_* = 2/(1-\nu^2)E = 8/3E$. Here we have assumed that the apical ring is incompressible (Poisson ratio $\nu = 1/2$), as are most biological materials.

With a fluid gap separating the apical ring from the spore, this purely elastic solution is modified. Dowson and Higginson [38] solved the coupled elastohydrodynamic problem by realizing that the fluid gap thickness h_o itself only slightly increases the elastic distortion of the apical ring. The pressure distribution in the center of the apical ring is thus still given by the Hertzian solution, scaling as $p \sim E\sqrt{x/\xi}$ for $x \lesssim \xi$. Similarly, away from the contact (negative x in Fig. 3.3.1E), the shape of the apical ring is mainly affected by the large elastic stresses within the contact, and so it is also given by the Hertzian solution, $h \sim \xi |x/\xi|^{3/2}$. However, there will be deviations near the entry point ($x \approx 0$), where the fluid pressures created by the flow through the gap will significantly modify $h(x)$.

Solving for $h(x)$ in this regime requires coupling the viscous flow in the gap to the elastic deformation of the apical ring. Viscous forces imply that the pressure gradient in the gap is given by the Reynolds lubrication equation,

$$\frac{dp}{dx} = 6\mu U \frac{h - h_o}{h^3}, \tag{3.28}$$

A coupled solution to the elastohydrodynamic problem requires that the pressure distribution $p(x)$ and the gap shape $h(x)$ satisfy *both* the Reynolds equation (3.28), and the elastic equations.

The value of h_o is selected by the solution to this coupled elastohydrodynamic problem [38]. The dependence of h_o on parameters follows from a scaling argument at $x \approx 0$ [55]. If λ is the length scale over which the pressure varies in the fluid gap, P is the pressure scale, and H is the scale of the gap thickness,

Eq. (3.28) implies $P/\lambda \sim \mu U/H^2$. The lubrication solution must match the Hertz solutions, implying $P \sim E\sqrt{\lambda/\xi}$ and $H \sim \xi(\lambda/\xi)^{3/2}$. Combining these relations, we find that

$$h_0 = \beta H = \beta \frac{\xi}{K^{3/5}} = \beta \left(\frac{\mu^3 p_0^{3/2} \ell^2 d(d+2b)^2}{\rho^{3/2} E_*^3 W b(d+b)} \right)^{1/5}, \tag{3.29}$$

where $K = E_* \xi/(U\eta)$ is the ratio of the elastic modulus to the viscous pressure created in the gap. The proportionality constant $\beta = 1.42$ requires the complete elastohydrodynamic solution, outlined in chapter 3.3.5. Fig. 3.3.3B shows the exact gap height and pressure following from this complete elastohydrodynamic analysis. Note that in order to effectively minimize the fluid loss through the gap, the pressure in the gap (for $x > 0$) will be significantly higher than in the ascus ($x << 0$). This is consistent with our previous assumption that the pressure in the ascus is the main accelerating force of the spore. The gap pressure acts nearly exactly perpendicular to the spore motion during the ejection of the spore and can thus be neglected when calculating its acceleration.

3.3.4 Optimality Criterion

We can now combine the results of the last two sections to define an optimal spore shooting apparatus. To minimize energy losses during spore ejection, the thickness of the fluid gap (h_0, Eq. (3.29)) determined by the elastohydrodynamic solution must be close to the optimal thickness of the fluid gap (h_*, Eq. (3.11)). The equation $h_0 = h_*$ implies the law

$$W = \gamma \frac{\mu^{1/2}}{(p_0 \rho)^{1/4}} \left(\frac{p_0}{E_*} \right)^3 \frac{d(d+2b)^2}{b(d+b)\sqrt{\ell}}, \tag{3.30}$$

where $\gamma = \gamma(a, \beta) = 371$ (see chapter 3.3.5 for derivation).

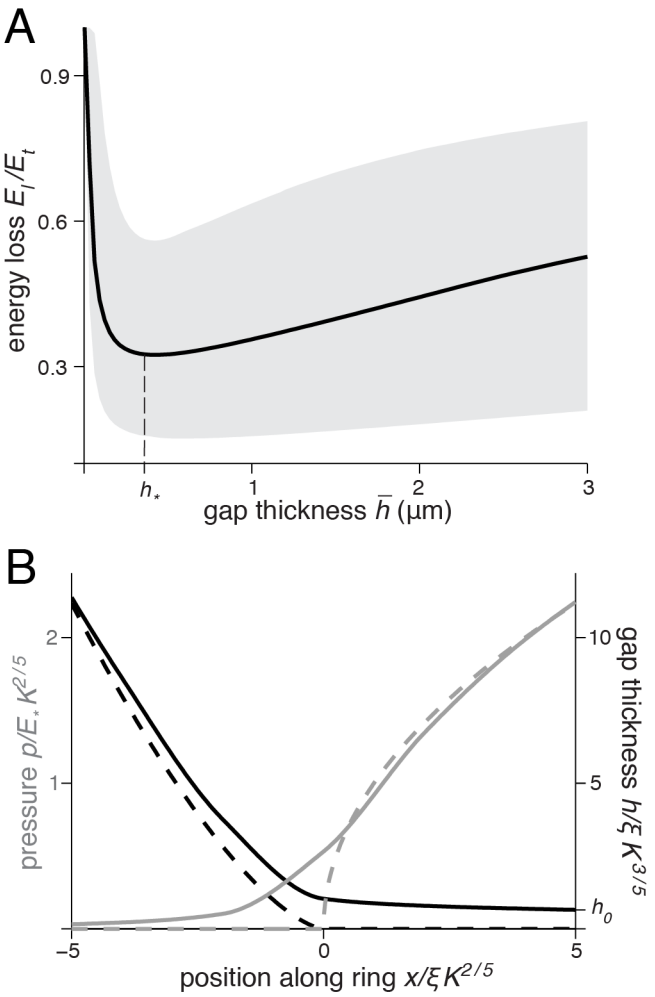

Figure 3.3.3: Simulations of the elastohydrodynamics of apical ring deformation coupled with spore motion shows the optimal thickness h^* (Eq. (3.11)). (A) Total energy dissipated through friction and fluid loss $E_l = E_{fluid} + E_{friction}$, as a function of the average gap thickness $\bar{h}$. We normalize E_l with the final spore kinetic energy $E_t = 2LW^2\rho U_{ej}^2/3$. Energy dissipation is minimized at the optimal gap thickness h_*, which is preserved as we vary the parameters of the model (G, C described in the chapter 3.3.5). Solid lines/shades: results obtained for a realistic set of parameters ($G = 0.05$, $C = 2.3$, $D = 0.79\,\mu m^{1/2}$) and their expected variation. (B) Normalized gap thickness (black) and pressure (grey) as a function of the distance from the point $x = 0$ where the spore first starts to compress the ring. The appropriate non-dimensionalization and numerical procedure are described in chapter 3.3.5. Dashed lines: solution of the dry contact problem; solid lines: solution of the full elastohydrodynamic problem.

3.3.5 Numerical calculation of constants

Dynamics of spore motion

To complement the scaling analysis presented in the paper, and exactly compute the energy dissipation during spore ejection we consider here the time evolution of the macroscopic motion of the spore. We introduce a closed system of equations for the velocity of the spore $U(t)$, the gap thickness $h(t)$ and the falling pressure in the ascus $p_a(t)$. The solution of these coupled equations with given initial condition gives the final velocity U_{ej} at which the spore is ejected.

Thickness of the lubrication layer. In the main text and section 3.3.5 we have outlined the method to solve the elastohydrodynamic equations to determine the constant gap thickness h_o at every instant in time. We summarize these results, highlighting the time dependence of the width of the spore $r(t)$ and the velocity of the spore $U(t)$:

$$h_o(t) = \beta \left(\frac{\mu U(t)}{E} \right)^{3/5} \xi(t)^{2/5} \tag{3.31}$$

where $\beta = 1.42$ (see section 3.3.5), $\xi(t) = 0.43\ell\sqrt{E/p_r(t)}$ and the dry contact pressure is

$$p_r(t) = E_* \frac{b(d+b)}{d(d+2b)^2}\, r(t) \tag{3.32}$$

For an ellipsoidal spore with width W and length L, $r = \frac{W}{L}\sqrt{X(L-X)}$, where X is the Lagrangian coordinate of the spore (measured from the tip of the spore to the apical ring, see figure 3.3.4).

Note that this solution for h_o is only valid in the case where the ascus pressure is much smaller than the dry contact pressure, which holds in this system for most of the spore ejection, except during the very initial stages when the spore starts to compress the ring to pass through.

Force balance on the spore. We now proceed to write Newton's law for the trajectory of the spore, subject to the ascus pressure p_a pushing the spore out and viscous stress originating in the lubrication layer. If we approximate the pressure

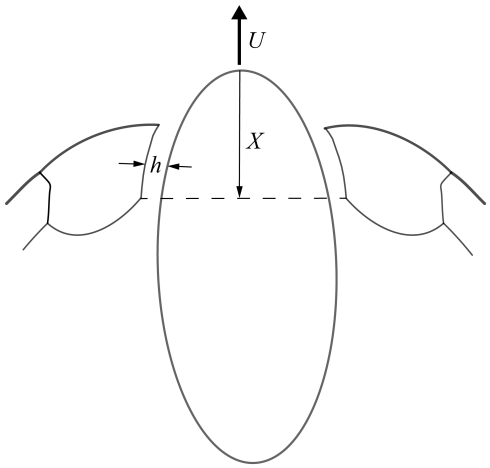

Figure 3.3.4: Definition of the Langrangian coordinate X in this model of spore ejection

in the gap as the dry contact pressure, and the height of the gap as $h_\circ$ from equation (3.31), the flow in the lubrication layer is a simple shear with no pressure gradients:

$$u(y) = U\frac{y}{h_\circ} \tag{3.33}$$

so that the viscous stress on the spore wall is

$$\mu\frac{du}{dy}|_{y=\circ} = \mu\frac{U}{h_\circ} \tag{3.34}$$

where y is the coordinate in the lubrication layer perpendicular to the spore wall. If U is the velocity of the spore and X its Lagrangian coordinate (measured from the tip of the spore to the apical ring), the equation of motion for the spore is:

$$m\frac{dU}{dt} = \pi r^2 p_a - \left[2\pi r l \mu \frac{U}{h_\circ}\right]\cos[\arctan r'] + 2\pi\int_\circ^l rpdx\sin[\arctan r'] \tag{3.35}$$

where the r.h.s. terms, from left to right, originate from the ascus pressure, the viscous stresses and the pressure forces in the gap respectively. This last term is negligible, since the spores are approximately fore-aft symmetric. The cos and sin

terms represent the projection of the forces along the direction of motion.

Writing $dU/dt = UdU/dX$ and using the mass of the spore $m = \pi/6\rho W^2 L$ we have

$$U\frac{dU}{dX} = \frac{6}{\rho L^3}X(L-X)p_a - \frac{12\mu l}{\rho W L^2 h_\circ}U\sqrt{X(L-X)} \tag{3.36}$$

where we have neglected the projection terms, since they only introduce a weak dependence on the aspect ratio of the spore.

Pressure evolution. As discussed in the model assumptions and section D the pressure in the ascus depends linearly on ascus volume, so that

$$\frac{p_a}{p_\circ} = \frac{V}{V_\circ} \tag{3.37}$$

The volume V of the ascus decreases as the spore and the fluid leave the ascus according to $dV/dt = -\pi U(t) r(r + h_\circ)$ where we used the linear velocity profile (3.33) in the lubrication layer so that

$$\frac{dp_a}{dt} = -\pi\frac{p_\circ}{V_\circ}Ur[r + h_\circ] \tag{3.38}$$

Nondimensional system. Equations (3.31), (3.36), (3.38) form a closed system of equations for the pressure in the ascus and the velocity of the spore. There are three length scales in this problem (H,h_*,W), we can thus define two non-dimensional parameters from them: $F = H/h_*$ representing the optimum identified in the main paper and $G = h_*/W$. We now non-dimensionalize with $X = \tilde{X}L$, $U = \sqrt{2p_\circ/\rho}\,\tilde{U}$, $r = W\sqrt{\tilde{X}(1-\tilde{X})}$ for ellipsoidal spores, $p_a = \tilde{p_a}p_\circ$ and $h_\circ = \beta H\tilde{U}^{3/5}/[\tilde{X}(1-\tilde{X})]^{1/10}$ and obtain the two coupled equations:

$$U\frac{dU}{dX} = 3X(1-X)p_a - \frac{12}{\beta}\frac{G}{F}U^{2/5}[X(1-X)]^{6/5} \tag{3.39}$$

$$\frac{dp_a}{dX} = -\frac{48}{C}[X(1-X) - \beta FGU^{3/5}(X(1-X))^{4/10} \tag{3.40}$$

where we have dropped the tildes. The solutions to these equations are

completely determined by three non-dimensional parameters F and G introduced above and C representing the ratio of fluid volume in the ascus to the volume of the spores $V_0 = 8C\pi W^2 L/6$ (assuming 8 spores in the ascus, by far the most common number).

As outlined in the main paper, we expect that to minimize dissipation, the morphology of the apical ring must be designed in such a way that the thickness of the lubrication layer matches the thickness at which minimum dissipation occurs, i.e. $h_0 = h_*$, or $F = F_{opt}$. Note that equation (3.39) immediately shows that there is indeed an optimal F: if F is too small, the spore rapidly loses momentum to viscous stress as the second term dominates the dynamics; if F is too large, the ascus pressure pushing the spore drops rapidly as a consequence of fluid loss (see eq (3.40)).

We are interested in a numerical solution for $U_{ej}(F, G, C)$ in a defined region of the space spanned by the three independent parameters. We expect: (i) $F = O(1)$, since at the optimum we must roughly have $h_0 = h_*$ (ii) $0.03 < G < 0.3$ to be determined by the maximum variation in spore size $2\ \mu\text{m} < W < 20\ \mu\text{m}$ and ring length $0.5\ \mu\text{m} < \ell < 2\ \mu\text{m}$ (iii) $2 < C < 6$, since the volume of fluid in the ascus before ejection is somewhere between 1 to 5 times the volume of spores in the ascus [59]. Numerical simulations of these equations show that there is indeed a sharp maximum in F (see figure 3.3.5) in the relevant region of phase space, and that the optimal value of F is nearly independent of both G and C. These latter properties are shown in Fig 3.3.6 and 3.3.7, which show contour plots of the optimal velocity as a function of F, G, C: the optimal value of F is essentially independent of both G and C.

From this analysis, we obtain $F_{opt} = 0.32 \pm 0.08$ for realistic values of G and C ($G = 0.05$ and $C = 2.3$) where the error is given by the range expected for these two nondimensional parameters. Since by definition $F_{opt} = \alpha/\beta$ we can use this result to determine α, since $\beta = 1.42$ follows purely from the elastohydrodynamic

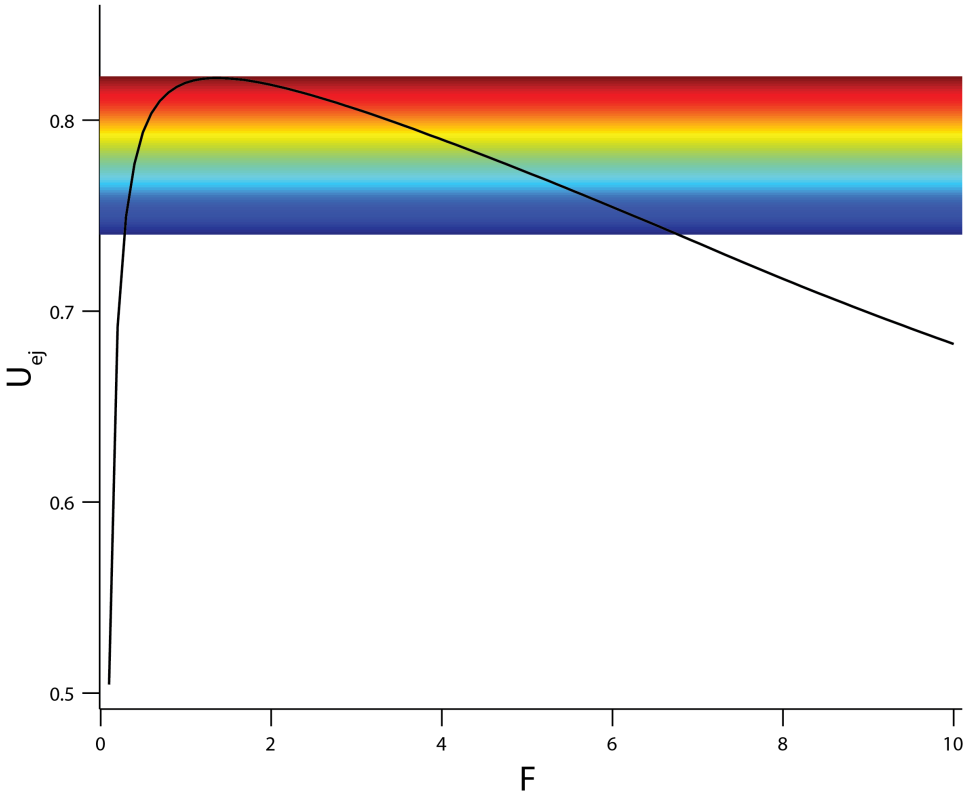

Figure 3.3.5: Final ejection speed as a function of F showing an optimal value, for $G = 0.05$ and $C = 2.3$. The color bar corresponds to the colors in the contour maps (Fig. 3.3.6 and Fig. 3.3.7).

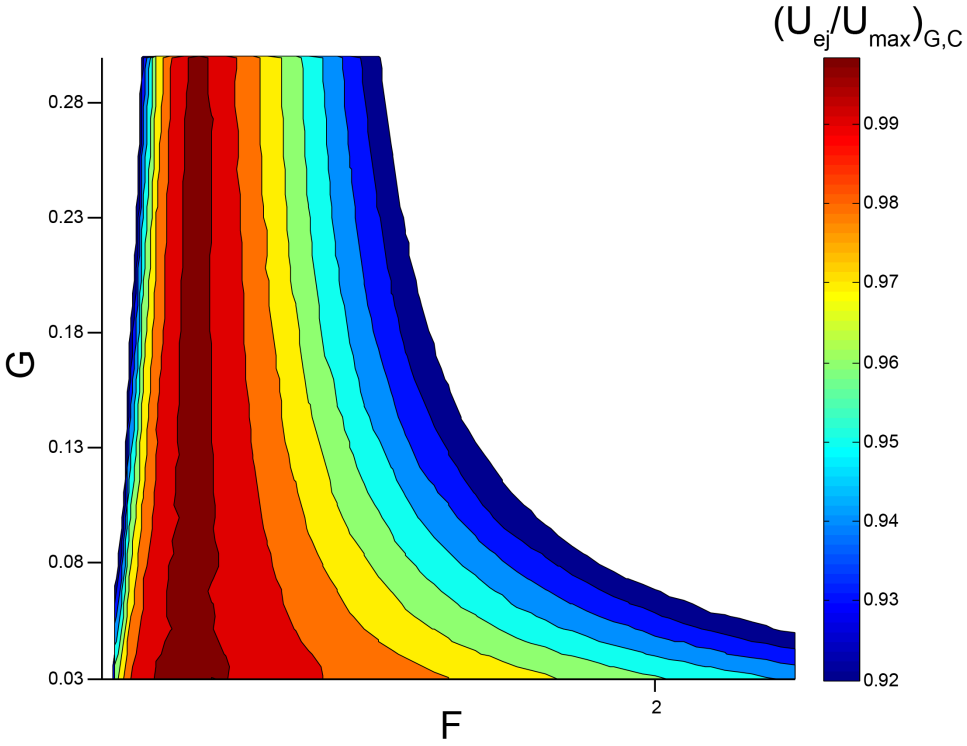

Figure 3.3.6: Contour map of the final ejection speed as a function of F and G, where the speed is normalized by the optimum value. The dark red denotes the parameter range where the optimum is attained. Note that there is a sharp optimum near $F \approx 0.32$, and its location is insensitive to G over the physiological range of the species considered here.

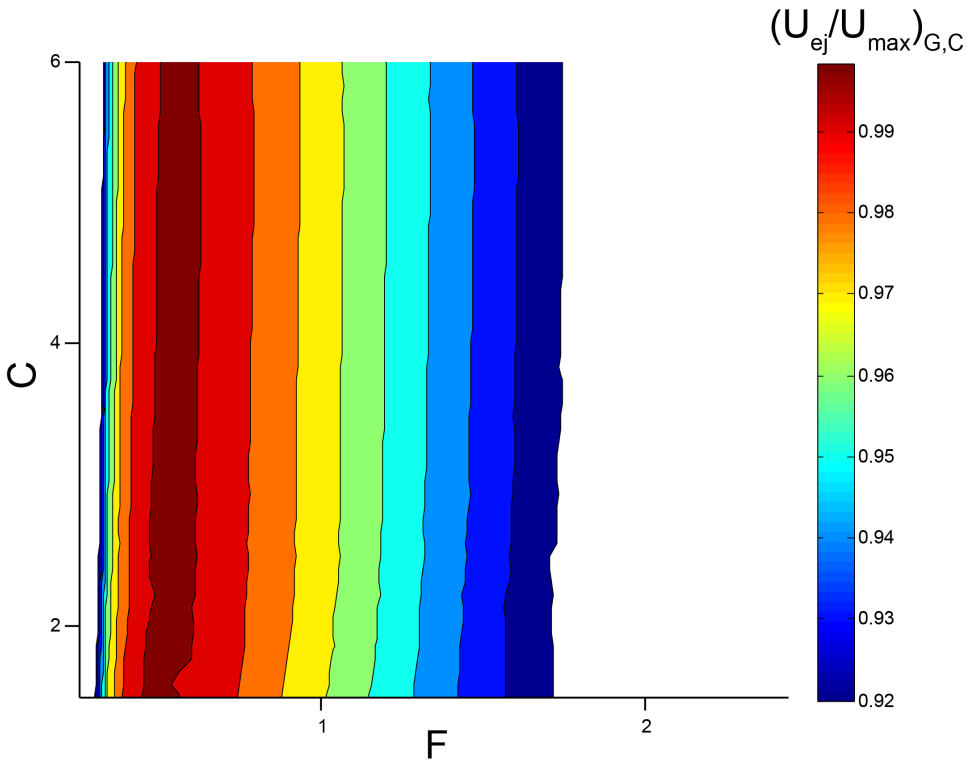

Figure 3.3.7: Contour map of the final ejection speed as a function of F and C, where the speed is normalized by the optimum value. The dark red denotes the parameter range where the optimum is attained. Note that there is a sharp optimum near $F \approx 0.32$, and its location is insensitive to C over the physiological range of the species considered here.

solution outlined in chapter 3.3.5. We find

$$a = \beta F_{opt} \approx 0.45. \tag{3.41}$$

Elastohydrodynamics

We now outline the solution to the elastohydrodynamic equations outlined in the main text. The structure of the solutions to these equations were discovered by Dowson and Higginson in the 1960's [38]; here we simply outline their original methodologies for solving the equations. More sophisticated variations of their methods have been extensively discussed [37].

Our goal is to find a solution for the gap height profile $h(x)$ in the entry region of the apical ring that satisfies both the Reynolds equation and the elasticity equation of the ring. Guided by the scaling outlined in the main text we non-dimensionalize the system with $\bar{p} = (p/E_*)F^{1/5}$, $\bar{x} = (x/\xi)F^{2/5}$, $\bar{h} = (3h/8\xi)F^{3/5}$ with $F = (32E_*\xi)/(27\mu U)$.

Then the lubrication equation becomes

$$\frac{d\bar{p}_f}{d\bar{x}} = \frac{\bar{h} - \bar{h}_0}{\bar{h}^3} \tag{3.42}$$

subject to the conditions $\bar{p}_c = \bar{x}^{1/2}$ for $x >> 0$ and $\bar{h} = \bar{x}^{3/2}$ for $x << 0$ arising from the Hertzian contact problem. This equation must be solved in conjunction with the elastic equation (Eqn. (3.32)).

We solve the problem of matching the hydrodynamic to the elastic solution iteratively, following a method first outlined by Hooke [55]. The central idea of this method is to find the minimal deformation away from the dry contact gap profile that allows

- the lubrication equation to be satisfied everywhere
- the height and height gradient at a point far away from the contact to be exactly the Hertz solution for the deformation and its gradient

- the pressure and pressure gradient at a point well into the contact to be exactly the dry contact pressure and pressure gradient

The basic steps in the algorithm are:

1. Guess a value for $\bar{h}_0$
2. At a point x_∞ well inside the contact region we calculate $\bar{h}_\infty$ according to (3.42) assuming the contact pressure gradient arising from $\bar{p}_c = \bar{x}^{1/2}$
3. Add the constant $\bar{h}_\infty$ to the height profile, so that in the first iteration $\bar{h} = \bar{h}_\infty + \bar{x}^{3/2}$
4. Given this height profile, perform a forward integration of the Reynolds equation from $-x_\infty$ to x_∞, with the initial condition $\bar{p} = 0$
5. Iteratively adjust the guess for $\bar{h}_0$ until the difference between the pressure at x_∞ from the hydrodynamic solution and the elastic solution becomes negligible by repeating the steps above
6. Calculate a correction to the height profile from this pressure difference as

$$\Delta\bar{h}(\bar{x}) = -R \int_{-x_\infty}^{x_\infty} (\bar{p}_f - \bar{p}_s) \ln(\bar{x} - s)^2 ds \tag{3.43}$$

   where R is a relaxation factor
7. Add this correction to $\bar{h}$ and repeat from step 1) until the norm of $\Delta\bar{h}$ is sufficiently small

Following the method outlined above with $R = 0.01$ and $x_\infty = 10$ yields a value of $\bar{h}_0 \approx 0.59$ (see figure 3.3.3 in the main paper for a full profile of gap height and pressure). With this result we can also find the value of β as defined in the main paper:

$$h_0 = \underbrace{0.59 \frac{8}{3} \left(\frac{27}{32}\right)^{3/5}}_{\beta} \underbrace{\frac{(\mu U)^{3/5} \xi^{2/5}}{E_*^{3/5}}}_{H} \tag{3.44}$$

$$\Rightarrow \beta \approx 1.42$$

Derivation of prefactor for the apical ring law

From the integration of the equations of motion (see Eq. (3.41)) we found that

$$F_{opt} = \frac{H}{h_*} = 0.32$$

Combining this with the results from the elastohydrodynamic solution (Eq. (3.44)) we find

$$\frac{(2\rho p_0)^{1/4}(\mu U)^{3/5}\xi^{2/5}}{(\mu\ell)^{1/2}E_*^{3/5}} = 0.32, \tag{3.45}$$

which can be rewritten in terms of the dimensions of spore and apical ring using Eqns. (3.32) as

$$\frac{(2\rho p_0)^{1/4}\mu^{3/5}(2p_0)^{3/10}(0.43\ell)^{2/5}d^{1/5}(d+2b)^{2/5}}{\rho^{3/10}(\mu\ell)^{1/2}E_*^{3/5}[Wb(d+b)]^{1/5}} = 0.32 \tag{3.46}$$

or in terms of $W = W(S_r)$

$$W = \underbrace{\frac{2^{11/4}(0.43)^2}{0.32^5}}_{\gamma}\ \frac{p_0^{11/4}\mu^{1/2}}{\rho^{1/4}E_*^3}\ \underbrace{\frac{d(d+2b)^2}{b(d+b)\sqrt{\ell}}}_{S_r}. \tag{3.47}$$

Thus we find

$$\gamma = \frac{2^{11/4}(0.43)^2}{0.32^5} \approx 371.$$

3.3.6 Testing the prediction with morphological data

Eq. (3.30) implies a strong constraint coupling spore and apical ring morphologies: the spore diameter W should be linearly proportional to a single parameter S_r, capturing the different dimensions of the apical ring,

$$S_r = \frac{d(d+2b)^2}{b(d+b)\sqrt{\ell}}, \tag{3.48}$$

if the material parameters of all species, most notably p_0/E_*, are reasonably conserved. While theoretical considerations make it likely that both these values individually should be roughly constant across different species, no experiments determining the elasticity of apical rings have been performed. The few available measurements of p_0 for different species indicate that this value might be roughly conserved [109].

To test our prediction, we compiled a library of over 1000 papers from the mycological literature, and searched them for high resolution electron-micrograph images showing medial cuts of mature apical rings (see appendix B for search rules and example images). We found data for 45 species in 2 classes (18 families), with a good coverage of the whole phylogeny of species whose spores are singly ejected through an apical ring (see Fig. 3.3.8, classes and families where data were found are shown in color). The phylogeny highlights the ubiquity of this trait in the ascomycetes (Fig. 3.3.8A), not only in two large classes (Fig. 3.3.8B,C) but also in more distant families (e.g. Peltigeracea and Geoglossacea), potentially indicating multiple independent origins of this trait. It also shows several loss events (represented by dashed lines), where species ejecting spores through an apical ring evolved into niches where this trait

Figure 3.3.8 ***(following page)*****:** Phylogenetic tree highlighting the 45 species used in this study (adapted from [101]). Classes and families with functional apical rings are in color, those with non-functional rings are represented by gray dashed lines, and classes with other dispersal mechanism are shown in solid gray. (A) Cladogram of the entire ascomycete phylum, delineating classes. Clades with functional apical rings are the Leotiomycetes (blue), Sordariomycetes (red), Geoglossaceae (orange) and the Peltigeracea in the Lecanoromycetes (green). More detailed phylogeny of the Sordariomycetes (B) and of the Leotiomycetes (C) delineating families. The families of the species used in this study are highlighted. (D) Examples of apical ring geometries (not to scale) to illustrate morphological diversity (redrawn from [16, 26, 34, 48, 54, 112, 114, 117]). Scale bars represents substitutions per site.

Figure 3.3.8: (continued)

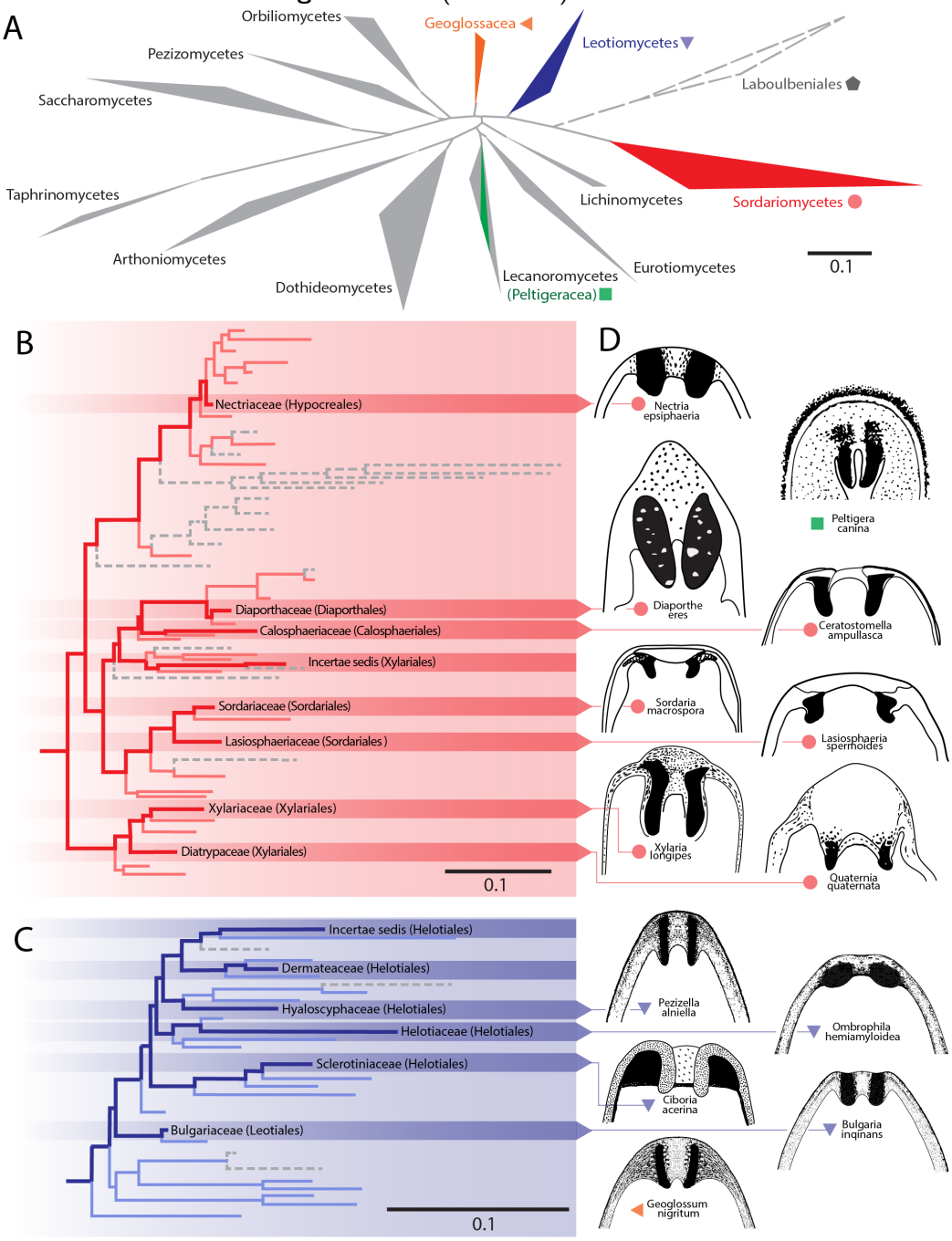

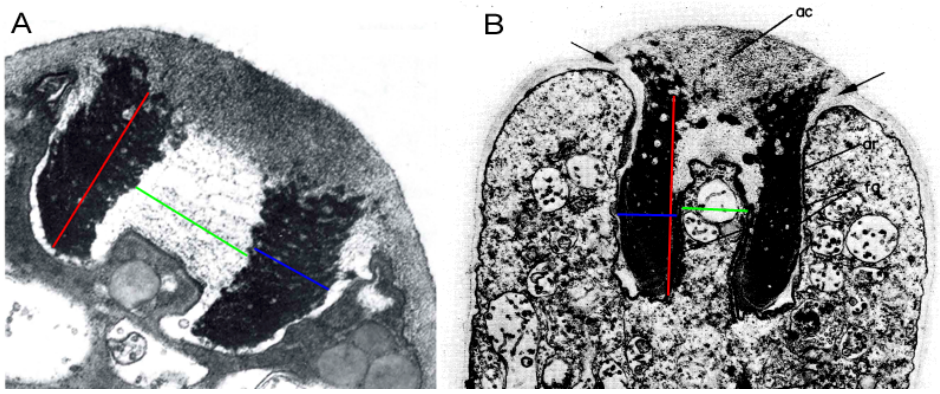

Figure 3.3.9: Examples for measured ring dimensions. Red is ring height ℓ, blue is ring thickness b and green is pore diameter d for (A) *Hypoxylon multiforme* and (B) *Xylaria longipes*

conveyed no selective advantage and was eventually lost, both on the class level (e.g. Laboulbeniales, Fig. 3.3.8A) and family level (Fig. 3.3.8B,C).

From the images found with this search we extracted the three independent dimensions of the apical ring (b, ℓ and d) relevant to our physical model, as well as the spore size W. When available, morphological data were taken from the same publication, to limit the influence of intraspecies variability. If no spore size was reported or could be measured, it was taken as the average value reported in standard texts [23, 36] (see appendix B for details).

Fig. 3.3.10 shows the results of this analysis. Each data point represents one species from the classes highlighted in Fig. 3.3.8. The individual dimensions of the apical rings are not strongly linked to the dimensions of the spores for the same species. The spore width W does not correlate with ℓ or b (R-squared 0.11 and 0.10). The degree of correlation between W and d is higher (R-squared 0.64), indicating that species with larger spores have apical rings with slightly larger diameters. In contrast, Fig. 3.3.10B shows the correlation of the spore radius with S_r. The data collapse on a single straight line (R-squared 0.84) is in excellent agreement with the theoretical expectation (Eq. (3.30)), with only one

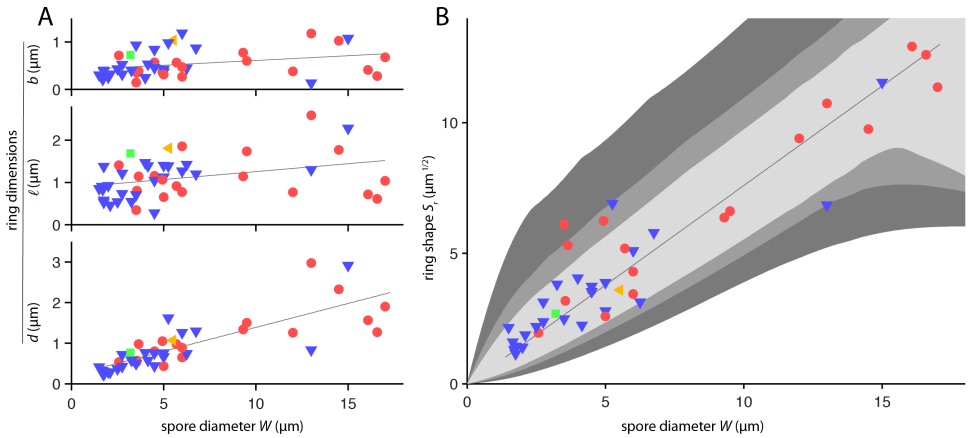

Figure 3.3.10: Comparison between the theoretical prediction and real morphological data for 45 species represented in Fig. 3.3.8 by matching colors and symbols. (A) Correlation between the width of the spore W and individual dimensions of the ring. The R-squared values of the correlations are 0.11, 0.10, 0.64 for ℓ, b, d respectively. (B) The non-trivial combination of lengthscales predicted theoretically correlates well with spore width (R-squared value 0.84). The line represents Eq. (3.30) with fitting parameter $D = 0.79\,\mu m^{1/2}$. Contour lines represent regions where spores attain 99% (light grey) 98% (grey) 95% (dark grey) of the maximum ejecion velocity.

free parameter $D = \gamma\mu^{1/2}(p_o/E_*)^3/(p_o\rho)^{1/4} = 0.79 \pm 0.06\,\mu m^{1/2}$. If we assume $\rho = 1000\,kg/m^{-3}$, $\mu = 10^{-3}$ Pa · s and $p_o = 2$ atm [41], the predicted elastic modulus of the apical ring is $E_* \approx 1$ MPa, consistent with the elastic moduli of soft biological materials [64].

To quantify energy losses within this system, Fig. 3.3.10B also shows contours (gray shading) for spores attaining 99%, 98%, and 95% of the maximum launch velocity, which can be obtained from a numerical integration of the equations of motion (see chapter 3.3.5). Nearly all of the data fall within 2% of the theoretical optimum.

3.3.7 Summary

The collapse of morphological data suggests spore launching apparatuses have evolved to maximize dispersal potential. A spore must escape its parent and if it can penetrate through the fluid mechanical boundary layer surrounding the sporocarp, it may be carried by the wind and achieve long distance dispersal. After launch from the ascus, the velocity $U(t)$ of a spore decelerates according to

$$m\frac{dU}{dt} = -\zeta U, \tag{3.49}$$

where m is the spore mass and ζ the drag coefficient. This implies that the distance Z a spore ejected with initial velocity U_{ej} will travel is given by

$$Z = U_{ej}\frac{m}{\zeta}. \tag{3.50}$$

The larger the range Z, the greater the variety of environments a spore can tolerate and still escape the boundary layer. We have previously shown the shape of spores (the ratio m/ζ) is tuned to within 1% of the theoretical optimum [93]; the present study demonstrates that the launch velocity U_{ej} is optimized to the same degree of precision by matching apical ring shape to spore size.

Our theory shows that gradients away from the optimum are steep – if a species moves off of the line in Fig. 3.3.10B, the energy dissipation penalty will be high, and the launch velocity U_{ej} will plummet.

The most striking feature of the data collapse shown in Fig. 3.3.10B is the large diversity of apical ring shapes captured by the model. Apical rings may be flat, thin, elongated, or shallow, with only weak correlations between the different geometrical dimensions, as seen in Fig. 3.3.8D (R-squared between 0.32 and 0.39), but in the right combination all morphologies are confined to the one dimensional subspace of the theoretical prediction (Eq. (3.30)). It is worth noting that our analysis explains more of the variation in the dimensions W, d, ℓ, b than traditional morphometric analysis using the first principal component (84 vs 64%). Principal component analysis finds the linear

combination of parameters that best explains a wide variance. In contrast, Eq. (3.30) depends nonlinearly on all of the parameters, in a fashion predicted by our mechanical analysis of dissipation processes occurring during spore ejection.

Morphologies may also be shaped by genetic constraints. To test whether genetics constrains fungi within the one-dimensional subspace, we explored the evolutionary trajectories of ascomycete species not subject to the selective force for range maximization. Several groups have evolved into niches where spore shooting is not critical to survival, because species use insects or other animals to disperse spores. Although nearly all of these species have completely lost the apical ring, the evolutionary residue of spore ejection is seen in a few genera, for example, *Geospora*. Species of *Geospora* do forcibly eject spores, but spores are ejected into a closed, subterranean sporocarp, where range maximization is irrelevant.

Using the same methodology described for the forcibly ejecting species (see chapter B for details) we collected morphological data for 13 species with non-functional rings: 7 are deliquescent i.e. ascospores are not forcibly ejected because the ascus wall dissolves; 5 are cleistothecial i.e. spores are released within an enclosed sporocarp; and one releases spores through a fissure in the ascus wall, and not through the apical ring. The spore and ring morphologies of 9 of 13 species are far from the subspace occupied by spore-shooting species (see Fig. 3.3.11). So while over 90% of all species with functional apical rings have morphologies within 2% of the optimum, this is only the case for about 30% of species with non-functional apical rings.

These data confirm that the data collapse in Fig. 3.3.10B is not the result of genetic constraints: alternate morphologies are possible. In fact, the time of divergence from an ancestor with a functional apical ring is positively correlated with the loss of optimality of the apical ring (see inset of Fig. 3.3.11), suggesting a role for genetic drift in shaping these morphologies. In a phylum with almost no fossil record, and where molecular clock models remain problematic, morphological trait evolution may provide valuable additional data for dating

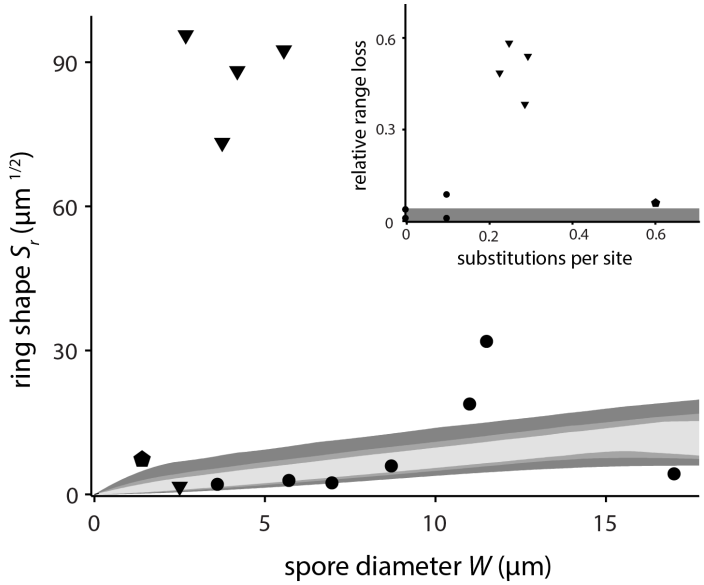

Figure 3.3.11: Morphological analysis for 13 species with non-functional apical rings. Symbols represent classes (see Fig. 3.3.8), species shown here are represented by dashed gray lines in Fig. 3.3.8. Contours as in Fig. 3.3.10B. Relaxation of the evolutionary constraint on the apical ring results in loss of optimality. No signature of the linear relation between W and S_r, as predicted by Eq. (3.30) for functional apical rings, can be seen here (R-squared 0.076; p-value 0.32). The (inset) shows a positive correlation between the phylogentic distance from the last ancestor with a functional apical ring (in substitutions per site) and the loss in range compared to an optimal ring geometry for the same spore size $(Z_{opt} - Z)/Z_{opt}$. The distance from the last common ancestor is measured on species level phylogenies [30, 108] using ancestral character reconstruction. The gray band corresponds to a 5% deviation from the optimum, which would contain all species with function apical rings. Note that 3 species are not shown in the inset, since their phylogenetic status in unclear.

species divergences.

Our model highlights the key role of physics in generating and shaping morphological diversity, which – even despite the emergence of molecular tools – remains a key to understanding the evolution of biodiversity.

It is easy to overlook this thought that life just is. As humans we are inclined to feel that life must have a point. We have plans and aspirations and desires. We want to take constant advantage of the intoxicating existence we've been endowed with. But what's life to a lichen? Yet its impulse to exist, to be , is every bit as strong as ours-arguably even stronger. If I were told that I had to spend decades being a furry growth on a rock in the woods, I believe I would lose the will to go on. Lichens don't.

Bill Bryson

4

The growth speed of crustose and foliose lichens

Lichens are a symbiosis of a fungus and photosynthetic algae or bacteria, and function as ecosystems, housing myriad other fungi and bacteria within a thallus [24, 80]. Lichens are ubiquitious, growing on bark or leaves, rocks, soil, and other substrates, and found at the poles, in boreal, temperate and tropical forests, and deserts and other biomes. Many ecosystems are dominated by lichen, and global models indicate that they are responsible for about 10% of total photosythesis on the planet. Approximately 8% of terrestrial ecosystems are lichen-dominated, both with respect to species diversity and in quantitative abundance [24].

Lichens grow slowly, and may be very old. Experimental data on the growth rates of foliose and crustose lichens, which are close to circular disks when

mature [5], also indicate that many species grow in a very reproducible manner. Very small lichens start with a low, bus steadily increasing growth rate, which levels of to a constant as they get bigger. This reproducible pattern of growth is leveraged in the field of lichenometry, which uses lichens to date deposits[61], for example rockfalls[27], by using the size of the largest thallus and measured or extrapolated growth rates of lichens to calculate an age of the substrate. While lichenometry is a current technique [45], the forces controlling lichen growth rates remain unclear[9, 74].

Diverse approaches to building models of lichen growth have been taken. The most successful and consistent with experimental data all share several essential features [4, 33, 51]. Carbon is assumed to be taken up uniformly over the surface area by the lichen symbiont (photosynthetic algae or bacteria) through photosynthesis. They model the internal flow of carbon within the mycelium of the lichen, which is supposed to be limiting the amount of carbon reaching the growing edge at the circumference of the circle. Additionally, a mechanism creates a gradient in the carbon distribution within the lichen, such that only a small band close the the growing edge can contribute to the size increase, which allows the growth rate to initially rise while the lichen is small (since the area of carbon uptake increases) and then level off, when the structure becomes bigger than the size of that band.

However experimental evidence is in conflict with these assumptions, consistently showing that internal transport of carbon does not seem to control the growth rate. Lichens where the center of the disk dies grow as fast as ones where the center is alive, even thought the area for uptake of carbon has been significantly reduced[7]. Lichen growth speed is also not affected by covering everything but a small band at the edge of the lichen for larger lichens, again removing nearly all of the available area for carbon uptake. Studies investigating the actual flow within the mycelium of lichens do not show fluxes that would be necessary to sustain growth at the observed speeds[9].

Here we present an alternate model of lichen growth that naturally produces the universal growth rate for circular lichens and is consistent with the existing

experimental data. Most of the mass of the lichen is made up of fungal mycelium, which in turn is dominated by carbon. The main source of carbon for a lichen is CO_2 taken up from photosynthesis through its photobiont. Given the density of photobionts close the the surface of most lichens, CO_2 will be completely depleted very close to the surface at steady state. Since lichens generally grow in wind protected areas, they are surrounded by a boundary layer of nearly still air with a thickness on the order of centimeters. Thus the depleted CO_2 cannot be replenished by active transport (e.g. wind over the lichen surface) and is instead diffusing through boundary layer. The pattern of diffusion is very different for a small roughly hemispherical lichen and a larger roughly circular disk-like lichen. For a small lichen, the flux over the surface area is constant and all the area contributes evenly to carbon uptake. Thus, with increased size, the surface area increases ind the growth rate accelerates. However as the lichen grows its height remains roughly constant while its radius continues to increase, thus creating a more and more disk like morphology. The flux of carbon into a large lichen is distinctly different, with nearly all the flux concentrated at the edge of the disk where the growth front lies.

The presented model is in excellent agreement with growth rate data, consistent with all experimental data on factors that influence the growth speed and correclty predicts the maximal growth speed of lichens in terms of only 4 parameters: the height H of the lichen, the diffusion constant D of CO_2 in air, the and the density of CO_2 in air and inside the lichen mycelium.

4.1 Diffusion of CO_2 around lichen enforces upper limit for growth speed

Figure 4.1.1a shows a schematic cross section of a growing lichen at several moments during its growth. We impose that the concentration of CO_2 at the surface of the lichen is 0, due to active photosythesis of the photobiont and is ρ_{CO_2}, the average value in free stream air, far away from the lichen, at the edge of

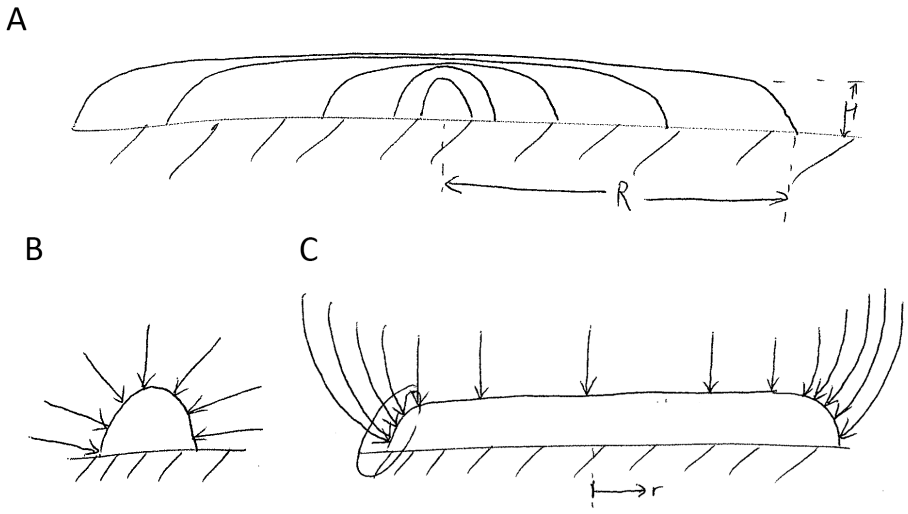

Figure 4.1.1: Lichen growth and associated flow pattern for different morphologies. (A) Cross section through a growing lichen for different time points. Note that while the height barely changes, the radial increase in size is high, changing the morphology from a hemispherical to a disk-like shape. (B) The diffusion pattern around small hemispherical lichen creates a uniform flux over the whole surface area. (C) For a more disk-like morphology, the flow pattern looks distinctly different, with most of the carbon influx concentrated at the edge, even though the photobionts are evenly distributed over the surface.

the boundary layer. Under these circumstances, we can construct a stream function Ψ for the flow of CO_2 in the air, which has to satisfy the Laplace equation

$$\nabla^2 \Psi = 0 \tag{4.1}$$

We can calculate the flux q of CO_2 into the lichen surface as $q = D\nabla\Psi$ under the assumption that the flux into the substrate on which the lichen is growing is zero. Solutions to the Laplace equation with this type of boundary conditions are a classical problem in physics, with well known solutions. Originally encountered in electrodynamics, where Ψ would be an electric potential and q the field strength on the surface of an ideal conductor, this problem has also been studied in fluid dynamics, e.g. for the evaporation of droplets, which is a nearly identical problem, except for a reversal of the flux direction. In the context of lichen growth, we are interested in two asymptotic limits with respect to the two length-scales of a lichen, its height H and its circular radius R (see Figure 4.1.1). If $H >= R$ the lichen is roughly a hemisphere, while for $R > H$ the lichen resembles a circular disk with a rounded edge and small contact angle.

Growth rate for small lichens

For a hemisphere, the flux of carbon is uniform over the surface and with our boundary conditions is

$$q = \frac{D\rho_{CO_2}}{H} \tag{4.2}$$

This flux leads to an increase in lichen mass of

$$\frac{dm}{dt} = \frac{d}{dt}\left(\frac{2\pi}{3}R^2 H \rho_{lichen}\right) = q\pi R^2 \tag{4.3}$$

and thus the growth rate of the lichen in terms of radius is

$$\frac{dR}{dt} = \frac{3}{2}R\frac{D\rho_{CO_2}}{H^2\rho_{lichen}} \propto R \tag{4.4}$$

Growth rate for large lichens

As the lichen grows larger, it more and more resembles a flat circular disk in external morphology (see Figure 4.1.1). For a disk the flux is very high at the edge

$$q = \frac{2D\rho_{CO_2}}{\pi\sqrt{R^2 - r^2}} \tag{4.5}$$

This flux leads to an increase in lichen mass of

$$\frac{dm}{dt} = \frac{d}{dt}\left(\frac{2\pi}{3}R^2 H\rho_{lichen}\right) = \int_0^R q(r)2\pi r dr \tag{4.6}$$

and thus the growth rate of the lichen in terms of radius is

$$\frac{dR}{dt} = \frac{2}{\pi}\frac{D\rho_{CO_2}}{H\rho_{lichen}} \tag{4.7}$$

which is independent of lichen radius R. This expression thus gives us an easy way to calculate the maximal growth rate this this mechanism allows. With $D = 5\,10^{-5}\mathrm{m}^2/\mathrm{s}$, $\rho_{CO_2} = 8\,10^{-4}\mathrm{kg}/\mathrm{m}^3$ and an average lichen density of $\rho_{lichen} \approx 10^2\mathrm{kg}/\mathrm{m}^3$ and lichen height $H = 4\,10^{-3}$ m, we can estimate

$$\frac{dR}{dt}_{max} \approx 10\frac{\mathrm{mm}}{\mathrm{year}} \tag{4.8}$$

4.2 Universal growth curve for lichens

Lichens generally do not reach this maximal growth speed, because they are only photosynthetic active under very defined conditions in terms of temperature, water availability and other parameters. This generally means that they are active only for a few hours every day. To compare our model predictions with real growth speeds, we will thus add an additional parameter e that represents the proportion of time the lichen is on average photosythetically active (i.e. $0 < e < 1$). The simplest functional form that contains the two asymptotic limits

derived above and smoothly interpolates between them is

$$\frac{dR}{dt} = \frac{2}{\pi}\frac{eD\rho_{CO_2}}{\rho_{lichen}H}\frac{R}{R + 4/(3\pi)H} \tag{4.9}$$

Of the parameters in this model D and ρ_{CO_2} are completely outside of the control of the lichen. In addition, the density of the mycelium does not vary significantly between different fungal species and thus ρ_{lichen} will also be roughly constant between different species. Thus the only way we expect the growth rates of different species to vary is through different average heights H and photosynthetic activity e. That is, we can write a non-dimensional, universal growth rate prediction for all species after writing $\tilde{r} = R/H$ and $\tilde{t} = t(\rho_{lichen}H)/(D\rho_{CO_2}e)$

$$\frac{d\tilde{r}}{d\tilde{t}} = \frac{2}{\pi}\frac{\tilde{r}}{\tilde{r} + 4/(3\pi)} \tag{4.10}$$

The model predicts that the growth rate of all foliose and crustoce circular lichens collapse onto this universal growth rate with only two free fitting parameters; H and e.

We test this prediction by analyzing published lichen growth curves in the literature. The result of this analysis is shown in Figure 4.2.1. Data for 7 different species of lichen collapse onto the predicted law to within error (error bars equal to 1 standard deviation).

We can not only collapse the experimental data onto the universal growth curve, our fitting parameters have physical meaning and thus can, and in a few cases have been measured. The results of this analysis is shown in Figure 4.2.2, where colored symbols represent the parameter for the best fit in Figure 4.2.1, and the error bars are the natural variation of that parameter in nature.

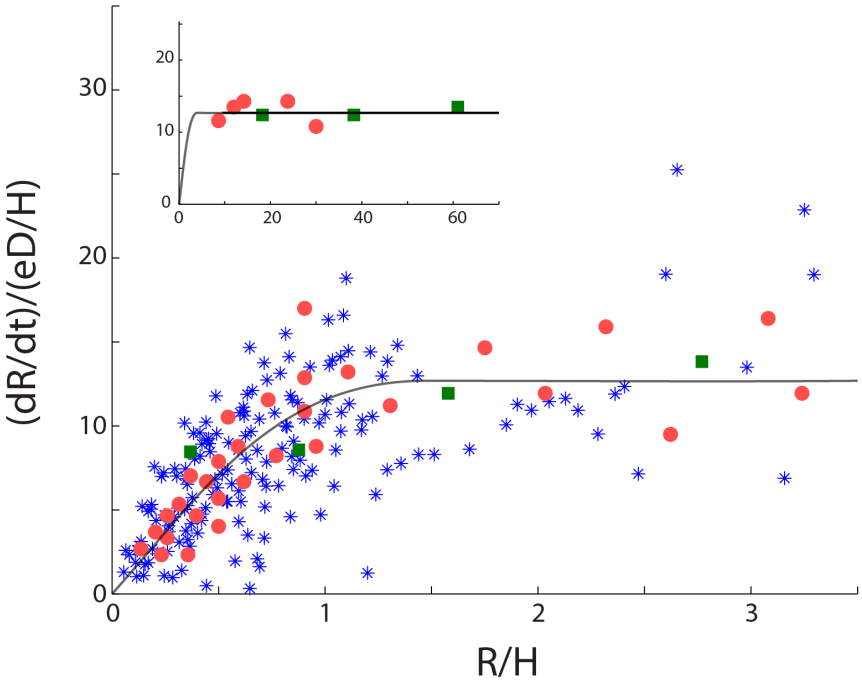

Figure 4.2.1: Universal lichen growth curve and comparison with experiments. The gray line is the predicted unviversal shape of the growth curve. Different symbols and colors represent experimental data from several literature sources (blue stars: Pringle 2013 (unpublished), green squares: [9], red circles: [17]).

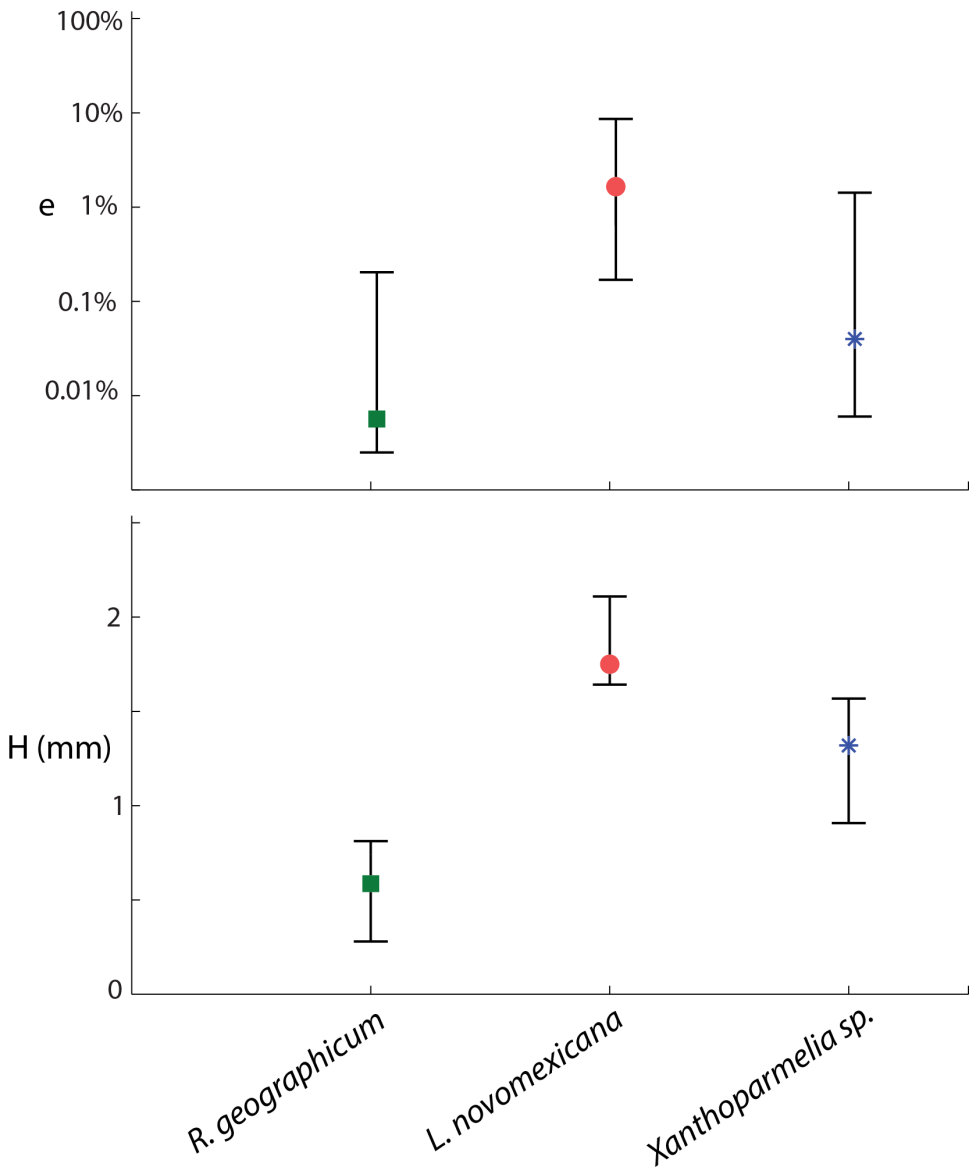

Figure 4.2.2: Values of fitting parameters agree with experimental data. colored symbols represent the parameter for the best fit in Figure 2 (blue stars: Pringle 2013 (unpublished), green squares: [9], red circles: [17]), error bars are the natural variation of that parameter in nature [6, 8, 9].

4.3 Direct lichen growth speed measurements

Most of the data presented in Figure 2 is based on indirect measurements of growth rate. To verify the accuracy of these experiments we additionally performed direct measurements of the growth rate for 40 lichens over the course of 6 years. A group of 55 foliose lichens growing on the French tombstone of the North Cemetery, Petersham, MA, USA (42°31'49.87" N, 72°11'22.32" W) was used to measure growth rates in nature. Target lichens are morphologically uniform and belong to the genus Xanthoparmelia. The taxonomy of species within Xanthoparmelia is controversial [70, 75], and without genetic data we cannot assign the population a species epithet. Inscribed letters and numbers were used to make a map of the entire population and identify individual thalli from year to year. Each thallus was measured each fall for seven years, starting in 2005. A transparent piece of plastic was placed over the thallus and the diameter of the thallus traced with permanent marker. Tracings were digitized and size calculated from digitized images. New individuals born in 2006, 2007, 2008 and 2009 were added to the survey, and during the survey 32 individuals died. By the end of the survey, in 2011, a total of 72 individuals were measured. To reduce noise in the dataset we filtered out all lichens that disappeared or died during the period of observation, and retained a dataset of 40 lichens. for each specimen, the growth rate dR/dt was determined as $(R_{n+1} - R_n)/1$ year, where $R_n = \sqrt{A_n}$ is the average radius of the lichen in year n.

4.4 Summary

We have presented a simple physical model that explains the universal growth rate of over 50.000 species of foliose and circular lichens. In contrast to previous models that analyzed internal carbon transport, this model only considers the flow of carbon in the air around the lichen. We have shown that this alone is enough to reproduce the lichen growth rate curve. This fact helps to explain the universality of the growth rate relation, the basic physical process is outside to the

control of the lichen, and using active forms of transport inside the lichen can thus not improve over this limit.

The results are also consistent with a host of interesting experiments that have been conducted to elucidate which factors play a role in explaining the growth rate. In many species, the center of the lichen dies out as the lichen grows very large, and its growth rate at the edge remains unchanged. As the lichen gets older, the carbon gain through the center becomes more and more negligible, thus making it ineffective to maintain the structure and photobionts there. At the same time, the flow pattern is not significantly disturbed when the center of the lichen is made passive, and thus the growth speed at the edge, which is limited by the external flux, remains unchanged. The model also explains nicely why experiments do not show internal fluxes of carbon towards the edge that are consistent with the observed growth speeds. The vast majority of carbon is added at the edge, where the flux is strongest, and thus no transport from the middle of the lichen to the edge is necessary.

References

[1] A. Abzhanov, M. Protas, B. R. Grant, P. R. Grant, and C. J. Tabin. Bmp4 and morphological variation of beaks in darwin's finches. *Science*, 305 (5689):1462–1465, September 2004. doi:10.1126/science.1098095.

[2] A. Abzhanov, W. P. Kuo, C. Hartmann, B. R. Grant, P. R. Grant, and C. J. Tabin. The calmodulin pathway and evolution of elongated beak morphology in darwin's finches. *Nature*, 442(7102):563–567, August 2006. doi:10.1038/nature04843.

[3] R. C. Albertson and T. D. Kocher. Genetic and developmental basis of cichlid trophic diversity. *Heredity*, 97(3):211–221, July 2006. doi:10.1038/sj.hdy.6800864.

[4] P. Aplin and D. Hill. Growth analysis of circular lichen thalli. *Journal of Theoretical Biology*, 78(3):347–363, June 1979. doi:10.1016/0022-5193(79)90335-7.

[5] R. A. Armstrong. Growth Phases in the Life of a Lichen Thallus. *New Phytologist*, 73(5):913––918, 1974. doi:10.1111/j.1469-8137.1974.tb01320.x.

[6] R. A. Armstrong and S. N. Smith. Factors determining the growth curve of the foliose lichen parmelia conspersa. *New Phytologist*, 134(3): 517–522, November 1996. doi:10.2307/2558569.

[7] R. Armstrong. Growth and regeneration of lichen thalli with the central portions artificially removed. *Environmental and Experimental Botany*, 19 (3):175–178, August 1979. doi:10.1016/0098-8472(79)90046-7.

[8] R. A. Armstrong. The biology of the crustose lichen rhizocarpon geographicum. *Symbiosis*, 55(2):53–67, September 2011. doi:10.1007/s13199-011-0147-x.

[9] R. A. Armstrong and T. Bradwell. Growth of foliose lichens: a review. *Symbiosis*, 53(1):1–16, January 2011. doi:10.1007/s13199-011-0108-4.

[10] A. E. Arnold and E. A. Herre. Canopy cover and leaf age affect colonization by tropical fungal endophytes: Ecological pattern and process in theobroma cacao (malvaceae). *Mycologia*, 95(3):388–398, May 2003.

[11] D. E. Aylor, Y. Wang, and D. R. Miller. Intermittent wind close to the ground within a grass canopy. *Boundary-Layer Meteorology*, 66(4): 427–448, December 1993. doi:10.1007/BF00712732.

[12] M. E. Barr. Notes on and additions to north american members of the herpotrichiellaceae. *Mycotaxon*, v. 41(2) p. 419-436, September 1991.

[13] A. Bary, H. E. F. Garnsey, and I. B. Balfour. *Comparative morphology and biology of the Fungi, Mycetozoa and bacteria*. Clarendon press, 1887.

[14] G. K. Batchelor. *An introduction to fluid dynamics*. Cambridge University Press, Cambridge, U.K.; New York, NY, 1999. ISBN 9781139648974.

[15] A. Beckett. The ascus with an apical pore: development, composition, and function. *Ascomycete systematics. The Luttrellian concept. New York: Springer-Verlag. p*, 7:26, 1981.

[16] A. Beckett and R. M. Crawford. The development and fine structure of the ascus apex and its role during spore discharge in xylaria longipes. *New Phytologist*, 72(2):357–369, March 1973. doi:10.2307/2430914.

[17] J. Benedict. Experiments on lichen growth, III. the shape of the age-size curve. *Arctic, Antarctic, and Alpine Research*, 40(1):15–26, February 2008. doi:10.1657/1523-0430(06-030)[BENEDICT]2.0.CO;2.

[18] K. D. Bing-Sheng Lu and W. W. Ho. Spirodecospora gen. novo (xylariaceae, ascomycotina), from bamboo in hong kong. *Fungal Diversity*, 1:169–177, 1998.

[19] M. Blackwell and J. W. Kimbrough. Ultrastructure of the termite-associated fungus laboulbeniopsis termitarius. *Mycologia*, 68(3): 541–550, June 1976.

[20] P. T. Boag and P. R. Grant. Heritability of external morphology in darwin's finches. *Nature*, 274(5673):793–794, August 1978. doi:10.1038/274793a0.

[21] J. Bond. *Birds of the West Indies*. The Academy of Natural Sciences of Philadelphia, 1936.

[22] R. I. Bowman. Morphological differentiation and adaptation in the galápagos finches. diferenciación morfológica y adaptación en los pinzones de las galápagos. *University of California Publications in Zoology.*, 58:1–302, 1961.

[23] J. Breitenbach, F. Kranzlin, J. F. Waters, and V. L. Waters. *Fungi of Switzerland: a contribution to the knowledge of the fungal flora of Switzerland*. Verlag Mykologia, 1984.

[24] M. I. M. Brodo, M. S. D. Sharnoff, and S. Sharnoff. *Lichens of North America*. Yale University Press, first edition edition, October 2001. ISBN 0300082495.

[25] H. Bronwen Griffiths. Fine structure of seven unitunicate pyrenomycete ASCI. *Transactions of the British Mycological Society*, 60(2):261–271, IN5–IN8, February 1973. doi:10.1016/S0007-1536(73)80009-9.

[26] H. Bronwen Griffiths. Fine structure of seven unitunicate pyrenomycete asci. *Transactions of the British Mycological Society*, 60(2):261–IN8, February 1973. doi:10.1016/S0007-1536(73)80009-9.

[27] W. B. Bull and M. T. Brandon. Lichen dating of earthquake-generated regional rockfall events, southern alps, new zealand. *Geological Society of America Bulletin*, 110(1):60–84, 1998.

[28] A. H. R. Buller. *Researches on Fungi*, volume 2. Longmans, Green and Company, 1922.

[29] K. J. Burns, S. J. Hackett, and N. K. Klein. Phylogenetic relationships and morphological diversity in darwin's finches and their relatives. *Evolution*, 56:1240–1252, June 2002.

[30] J. Campbell, J. L. Anderson, and C. A. Shearer. Systematics of halosarpheia based on morphological and molecular data. *Mycologia*, 95 (3):530–552, May 2003.

[31] O. Campàs, R. Mallarino, A. Herrel, A. Abzhanov, and M. P. Brenner. Scaling and shear transformations capture beak shape variation in darwin's finches. *Proceedings of the National Academy of Sciences*, 107(8): 3356–3360, February 2010. doi:10.1073/pnas.0911575107.

[32] M. Chadefaud. Etudes d'asques, ii. structure et anatomie comparee de i'appareil apical des asques chez divers discomycetes et pyrenomycetes. *Revue Mycol.*, 7:57–88, 1942.

[33] S. Childress and J. B. Keller. Lichen growth. *Journal of Theoretical Biology*, 82(1):157–165, January 1980. doi:10.1016/0022-5193(80)90095-8.

[34] M. Corlett and M. E. Elliott. The ascus apex of ciboria acerina. *Canadian Journal of Botany*, 52(7):1459–1463, July 1974. doi:10.1139/b74-191.

[35] C. Darwin. On the origins of species by means of natural selection. *London: Murray*, 1859.

[36] R. W. G. Dennis. *British Ascomycetes*. J. Cramer., 1978.

[37] D. Dowson. Elastohydrodynamic and micro-elastohydrodynamic lubrication. *Wear*, 190(2):125–138, 1995.

[38] D. Dowson and G. R. Higginson. A numerical solution to the elasto-hydrodynamic problem. *Journal of Mechanical Engineering Science*, 1 (1):6–15, 1959.

[39] V. Duboc and M. P. Logan. Building limb morphology through integration of signalling modules. *Current Opinion in Genetics & Development*, 19(5): 497–503, October 2009. doi:10.1016/j.gde.2009.07.002.

[40] H. C. Evans. Entomogenous fungi in tropical forest ecosystems: an appraisal. *Ecological Entomology*, 7(1):47–60, 1982. doi:10.1111/j.1365-2311.1982.tb00643.x.

[41] M. Fischer, J. Cox, D. J. Davis, A. Wagner, R. Taylor, A. J. Huerta, and N. P. Money. New information on the mechanism of forcible ascospore discharge from ascobolus immersus. *Fungal Genetics and Biology*, 41(7): 698–707, July 2004. doi:10.1016/j.fgb.2004.03.005.

[42] M. W. Fischer, J. L. Stolze-Rybczynski, D. J. Davis, Y. Cui, and N. P. Money. Solving the aerodynamics of fungal flight: how air viscosity slows spore motion. *Fungal Biology*, 114(11–12):943–948, November 2010. doi:10.1016/j.funbio.2010.09.003.

[43] M. C. Fisher, D. A. Henk, C. J. Briggs, J. S. Brownstein, L. C. Madoff, S. L. McCraw, and S. J. Gurr. Emerging fungal threats to animal, plant and ecosystem health. *Nature*, 484(7393):186–194, April 2012. doi:10.1038/nature10947.

[44] P. J. Flory. *Principles of polymer chemistry.* Cornell University Press, Ithaca, 1953. ISBN 0801401348.

[45] I. A. Garibotti and R. Villalba. Lichenometric dating using rhizocarpon subgenus rhizocarpon in the patagonian andes, argentina. *Quaternary Research*, 71(3):271–283, May 2009. doi:10.1016/j.yqres.2009.01.012.

[46] A. Genbrugge, A.-S. Heyde, D. Adriaens, M. Boone, L. Van Hoorebeke, J. Dirckx, P. Aerts, J. Podos, and A. Herrel. Ontogeny of the cranial skeleton in a darwin's finch (geospiza fortis). *Journal of Anatomy*, 219(2): 115–131, 2011. doi:10.1111/j.1469-7580.2011.01388.x.

[47] F. B. Gill. *Ornithology*. W. H. Freeman, third edition edition, October 2006. ISBN 0716749831.

[48] G. Greenhalgh and L. Evans. The structure of the ascus apex in hypoxylon fragiforme with reference to ascospore release in this and related species. *Transactions of the British Mycological Society*, 50(2):183–IN1, June 1967. doi:10.1016/S0007-1536(67)80028-7.

[49] G. Greenhalgh and L. Evans. The structure of the ascus apex in hypoxylon fragiforme with reference to ascospore release in this and related species. *Transactions of the British Mycological Society*, 50(2):183–188, June 1967. doi:10.1016/S0007-1536(67)80028-7.

[50] J. A. Helms and R. A. Schneider. Cranial skeletal biology. *Nature*, 423 (6937):326–331, May 2003. doi:10.1038/nature01656.

[51] D. Hill. The growth of lichens with special reference to the modelling of circular thalli. *The Lichenologist*, 13(03):265–287, 1981. doi:10.1017/S0024282981000352.

[52] H. R. Hohl and W. Streit. Ultrastructure of ascus, ascospore and ascocarp in neurospora lineolata. *Mycologia*, 67(2):367–381, April 1975.

[53] P. W. Holland. *The skull Vol. 2: Patterns of Structural and Systematic Diversity*. Elsevier Current Trends, 1994.

[54] R. Honegger. The ascus apex in lichenized fungi i. the lecanora-, peltigera- and teloschistes-types. *The Lichenologist*, 10(01):47–67, 1978. doi:10.1017/S0024282978000079.

[55] C. J. Hooke and J. P. O'Donoghue. Elastohydrodynamic lubrication of soft, highly deformed contacts. *Journal of Mechanical Engineering Science*, 14(1):34–48, 1972.

[56] J. Huxley. Evolution. the modern synthesis. *Evolution. The Modern Synthesis.*, 1942.

[57] K. D. Hyde and S. W. Wong. An ultrastructural study of the asci and banded ascospores of fasciatispora petrakii. *Fungal Diversity*, 2:129–134, 1999.

[58] P. Inderbitzin and M. L. Berbee. Lollipopaia minuta from thailand, a new genus and species of the diaporthales (ascomycetes, fungi) based on morphological and molecular data. *Canadian Journal of Botany*, 79(9): 1099–1106, 2001.

[59] C. T. Ingold. Ballistics in certain ascomycetes. *New Phytologist*, 60(2): 143–149, 1961. doi:10.1111/j.1469-8137.1961.tb06248.x.

[60] C. T. Ingold. *Fungal spores: their liberation and dispersal*. Clarendon Press, 1971.

[61] J. L. Innes. Lichenometry. *Progress in Physical Geography*, 9(2):187–254, 1985.

[62] F. Jacob. Evolution and tinkering. *Science*, 196(4295):1161–1166, 1977.

[63] J. D. Jensen. The development of diaporthe phaseolorum variety sojae in culture. *Mycologia*, 75(6):1074–1091, November 1983. doi:10.2307/3792664.

[64] T. P. J. Knowles and M. J. Buehler. Nanomechanics of functional and pathological amyloid materials. *Nature Nanotechnology*, 6(8):469–479, August 2011. doi:10.1038/nnano.2011.102.

[65] R. D. Koehn. Laboratory culture and ascocarp development of podosordaria leporina. *Mycologia*, 63(3):441–458, 1971. doi:10.2307/3757544.

[66] R. A. Krause and R. K. Webster. The morphology, taxonomy, and sexuality of the rice stem rot fungus, magnaporthe salvinii (leptosphaeria salvinii). *Mycologia*, 64(1):103–114, January 1972. doi:10.2307/3758018.

[67] H. M. Kronenberg. Developmental regulation of the growth plate. *Nature*, 423(6937):332–336, May 2003. doi:10.1038/nature01657.

[68] D. Lack. *Darwin's finches*. Cambridge University Press, 1947. ISBN 0521252431.

[69] E. Laufer, C. E. Nelson, R. L. Johnson, B. A. Morgan, and C. Tabin. Sonic hedgehog and fgf-4 act through a signaling cascade and feedback loop to integrate growth and patterning of the developing limb bud. *Cell*, 79(6): 993–1003, December 1994. doi:10.1016/0092-8674(94)90030-2.

[70] S. D. Leavitt, L. Johnson, and L. L. S. Clair. Species delimitation and evolution in morphologically and chemically diverse communities of the lichen-forming genus xanthoparmelia (parmeliaceae, ascomycota) in western north america. *American Journal of Botany*, 98(2):175–188, February 2011. doi:10.3732/ajb.1000230.

[71] K. Leenurm, A. Raitviir, and R. Raid. Studies on the ultrastructure of lachnum and related genera (hyaloscyphaceae, helotiales, ascomycetes). *Sydowia*, 52(1):30–45, June 2000.

[72] C. Linnaeus. *Species plantarum*, volume 4. Impensis GC Nauk, 1800.

[73] R. W. Little. *Elasticity*. Prentice-Hall (Englewood Cliffs, NJ), 1973.

[74] M. G. Loso and D. F. Doak. The biology behind lichenometric dating curves. *Oecologia*, 147(2):223–229, March 2006. doi:10.1007/s00442-005-0265-3.

[75] H. T. Lumbsch and S. D. Leavitt. Goodbye morphology? a paradigm shift in the delimitation of species in lichenized fungi. *Fungal Diversity*, 50(1): 59–72, September 2011. doi:10.1007/s13225-011-0123-z.

[76] R. Mallarino, P. R. Grant, B. R. Grant, A. Herrel, W. P. Kuo, and A. Abzhanov. Two developmental modules establish 3D beak-shape variation in darwin's finches. *Proceedings of the National Academy of Sciences*, 108(10):4057–4062, March 2011. doi:10.1073/pnas.1011480108.

[77] R. Mallarino, O. Campàs, J. A. Fritz, K. J. Burns, O. G. Weeks, M. P. Brenner, and A. Abzhanov. Closely related bird species demonstrate flexibility between beak morphology and underlying developmental programs. *Proceedings of the National Academy of Sciences*, 109(40): 16222–16227, October 2012. doi:10.1073/pnas.1206205109.

[78] E. Mayr. Geographical character gradients and climatic adaptation. *Evolution*, 10(1):105–108, March 1956. doi:10.2307/2406103.

[79] S. T. Moss. *The Biology of marine fungi*. CUP Archive, 1986. ISBN 9780521308991.

[80] A. A. Mushegian, C. N. Peterson, C. C. Baker, and A. Pringle. Bacterial diversity across individual lichens. *Applied and environmental microbiology*, 77(12):4249–4252, 2011.

[81] A. Nakagiri and T. Ito. Aniptodera salsuginosa, a new mangrove-inhabiting ascomycete, with observations on the effect of salinity on ascospore appendage morphology. *Mycological Research*, 98 (8):931–936, August 1994. doi:10.1016/S0953-7562(09)80265-7.

[82] E. E. Pennisi. Armed and dangerous. *Science*, 327(5967):804–805, February 2010. doi:10.1126/science.327.5967.804.

[83] J. Podos. Correlated evolution of morphology and vocal signal structure in darwin's finches. *Nature*, 409(6817):185–188, January 2001. doi:10.1038/35051570.

[84] K. Pärtel and A. Raitviir. The ultrastructure of the ascus apical apparatus of some dermateaceae (helotiales). *Mycological Progress*, 4(2):149–159, May 2005. doi:10.1007/s11557-006-0118-4.

[85] E. M. Purcell. Life at low reynolds number. *AIP Conference Proceedings*, 28 (1):49–64, December 1976. doi:doi:10.1063/1.30370.

[86] N. B. Raju. Nonlinear asci without apical pores in the peak mutant of neurospora. *Mycologia*, 80(6):825–831, November 1988. doi:10.2307/3807561.

[87] N. B. Raju and D. D. Perkins. Diverse programs of ascus development in pseudohomothallic species of neurospora, gelasinospora, and podospora. *Developmental Genetics*, 15(1):104–118, January 1994. doi:10.1002/dvg.1020150111.

[88] A. W. Ramaley. Barrina, a new genus with polysporous asci. *Mycologia*, 89 (6):962, November 1997. doi:10.2307/3761118.

[89] S. J. Read, E. B. G. Jones, S. T. Moss, and R. G. Johnson. Ultrastructural observations of the marine ascomycotina *Corollospora angusta, Corollospora colossa, Corollospora lacera* and *Chaetosphaeria chaetosa*. *Botanica Marina*, 35(6):553–560, January 1992. doi:10.1515/botm.1992.35.6.553.

[90] F. B. Reeves. The structure of the ascus apex in sordaria fimicola. *Mycologia*, 63(2):204–212, April 1971.

[91] R. S. Ridgely and G. Tudor. *The Birds of South America: Jays and Swallows, Wrens, Thrushes, and Allies, Vireos and Wood-warblers, Tanagers, Icterids, and Finches. The Oscine Passerines*, volume 1. U of Texas Press, 1989.

[92] S. J. Rodda and A. P. McMahon. Distinct roles for hedgehog and canonical wnt signaling in specification, differentiation and maintenance of osteoblast progenitors. *Development*, 133(16):3231–3244, August 2006. doi:10.1242/dev.02480.

[93] M. Roper, R. E. Pepper, M. P. Brenner, and A. Pringle. Explosively launched spores of ascomycete fungi have drag-minimizing shapes. *Proceedings of the National Academy of Sciences*, 105(52):20583–20588, December 2008. doi:10.1073/pnas.0805017105.

[94] M. Roper, A. Seminara, M. M. Bandi, A. Cobb, H. R. Dillard, and A. Pringle. Dispersal of fungal spores on a cooperatively generated wind. *Proceedings of the National Academy of Sciences of the United States of*

America, 107(41):17474–17479, October 2010. doi:10.1073/pnas.1003577107.

[95] A. Sakai. Formation of ascispore delimiting membrane in sordaria humana. *Development, Growth & Differentiation*, 16(3):181–190, January 1974. doi:10.1111/j.1440-169X.1974.00181.x.

[96] I. Salazar-Ciudad and M. Marín-Riera. Adaptive dynamics under development-based genotype-phenotype maps. *Nature*, 497(7449): 361–364, May 2013. doi:10.1038/nature12142.

[97] D. A. Samuelson. Asci of the pezizales. i. the apical apparatus of iodine-positive species. *Canadian Journal of Botany*, 56(16):1860–1875, August 1978. doi:10.1139/b78-225.

[98] P. J. Scherz, B. D. Harfe, A. P. McMahon, and C. J. Tabin. The limb bud shh-fgf feedback loop is terminated by expansion of former ZPA cells. *Science*, 305(5682):396–399, July 2004. doi:10.1126/science.1096966.

[99] H. Schlichting and K. Gersten. *Boundary-layer theory*. Springer, 2000.

[100] R. A. Schneider and J. A. Helms. The cellular and molecular origins of beak morphology. *Science*, 299(5606):565–568, January 2003. doi:10.1126/science.1077827.

[101] C. L. Schoch, G.-H. Sung, F. López-Giráldez, J. P. Townsend, J. Miadlikowska, V. Hofstetter, B. Robbertse, P. B. Matheny, F. Kauff, Z. Wang, C. Gueidan, R. M. Andrie, K. Trippe, L. M. Ciufetti, A. Wynns, E. Fraker, B. P. Hodkinson, G. Bonito, J. Z. Groenewald, M. Arzanlou, G. S. d. Hoog, P. W. Crous, D. Hewitt, D. H. Pfister, K. Peterson, M. Gryzenhout, M. J. Wingfield, A. Aptroot, S.-O. Suh, M. Blackwell, D. M. Hillis, G. W. Griffith, L. A. Castlebury, A. Y. Rossman, H. T. Lumbsch, R. Lücking, B. Büdel, A. Rauhut, P. Diederich, D. Ertz, D. M. Geiser, K. Hosaka, P. Inderbitzin, J. Kohlmeyer, B. Volkmann-Kohlmeyer, L. Mostert, K. O'Donnell, H. Sipman, J. D. Rogers, R. A. Shoemaker, J. Sugiyama, R. C. Summerbell, W. Untereiner, P. R. Johnston, S. Stenroos, A. Zuccaro, P. S. Dyer, P. D. Crittenden, M. S. Cole, K. Hansen, J. M. Trappe, R. Yahr, F. Lutzoni, and J. W. Spatafora. The ascomycota tree of life: A phylum-wide phylogeny clarifies the origin and evolution of fundamental reproductive and ecological traits. *Systematic Biology*, 58(2): 224–239, April 2009. doi:10.1093/sysbio/syp020.

[102] O. Shoval, H. Sheftel, G. Shinar, Y. Hart, O. Ramote, A. Mayo, E. Dekel, K. Kavanagh, and U. Alon. Evolutionary trade-offs, pareto optimality, and the geometry of phenotype space. *Science*, 336(6085):1157–1160, June 2012. doi:10.1126/science.1217405.

[103] L. Shum, X. Wang, A. A. Kane, and G. H. Nuckolls. BMP4 promotes chondrocyte proliferation and hypertrophy in the endochondral cranial base. *The International journal of developmental biology*, 47(6):423–431, September 2003.

[104] A. Sivanesan, W. Hsieh, and C. Chen. Prostratus, a new diaporthaceous ascomycete genus on cyclobalanopsis from taiwan. *Mycological Research*, 97(10):1179–1182, 1993. doi:16/S0953-7562(09)81281-1.

[105] J. Soons, A. Herrel, A. Genbrugge, P. Aerts, J. Podos, D. Adriaens, Y. de Witte, P. Jacobs, and J. Dirckx. Mechanical stress, fracture risk and beak evolution in darwin's ground finches (geospiza). *Philosophical Transactions of the Royal Society B: Biological Sciences*, 365(1543):1093–1098, April 2010. doi:10.1098/rstb.2009.0280.

[106] B. St-Jacques, M. Hammerschmidt, and A. P. McMahon. Indian hedgehog signaling regulates proliferation and differentiation of chondrocytes and is essential for bone formation. *Genes & Development*, 13(16):2072–2086, August 1999.

[107] D. L. Stiers. The fine structure of the ascus apex in hypoxylon serpens, poronia punctata, rosellinia aquila, and r. mammiformis. *Cytologia*, 42 (3-4):697–702, 1977. doi:10.1508/cytologia.42.697.

[108] S. Thongkantha, R. Jeewon, D. Vijaykrishna, S. Lumyong, E. H. C. McKenzie, and K. D. Hyde. Molecular phylogeny of magnaporthaceae (sordariomycetes) with a new species, Ophioceras chiangdaoense from Dracaena loureiroi in thailand. *Fungal Diversity*, 34:157–173, 2009.

[109] F. Trail. Fungal cannons: explosive spore discharge in the ascomycota. *FEMS Microbiology Letters*, 276(1):12–18, 2007. doi:10.1111/j.1574-6968.2007.00900.x.

[110] F. Trail, H. Xu, R. Loranger, and D. Gadoury. Physiological and environmental aspects of ascospore discharge in gibberella zeae

(anamorph fusarium graminearum). *Mycologia*, 94(2):181–189, March 2002. doi:10.2307/3761794.

[111] F. Trail, I. Gaffoor, and S. Vogel. Ejection mechanics and trajectory of the ascospores of gibberella zeae (anamorph fuarium graminearum). *Fungal Genetics and Biology*, 42(6):528–533, June 2005. doi:10.1016/j.fgb.2005.03.008.

[112] G. J. M. Verkley. Ultrastructure of the apical apparatus of asci in Ombrophila violacea, Neobulgaria pura and Bulgaria inquinans (Leotiales). *Persoonia*, 15:3–22, 1992.

[113] G. J. M. Verkley. Ultrastructure of the ascus apical apparatus in Hymenoscyphus and other genera of the Hymenoscyphoideae (Leotiales, Ascomycotina). *Persoonia*, 15:303–340, 1993.

[114] G. J. M. Verkley. Ultrastructure of the ascus apical apparatus in Leotia lubrica and some Geoglossaceae (Leotiales, Ascomycotina). *Persoonia*, 15:405–430, 1994.

[115] G. J. M. Verkley. *A monograph of the genus Pezicula and its anamorphs*. Studies in mycology ; no. 44. Centraalbureau voor Schimmelcultures, Baarn/Delft, The Netherlands, 1999. ISBN 9070351404.

[116] G. J. Verkley. Ultrastructure of the ascus apical apparatus in ten species of Sclerotiniaceae. *Mycological Research*, 97(2):179–194, February 1993. doi:10.1016/S0953-7562(09)80240-2.

[117] G. J. Verkley. Ultrastructure of the ascus apical apparatus and ascospore wall in Ombrophila hemiamyloidea (Helotiales, Ascomycota). *Nova Hedwigia*, 77(3-4):271–285, 2003. doi:10.1127/0029-5035/2003/0077-0271.

[118] S. Vogel. Living in a physical world II. the bio-ballistics of small projectiles. *Journal of Biosciences*, 30(2):167–175, March 2005. doi:10.1007/BF02703696.

[119] J. D. Wilson, D. P. Ward, G. W. Thurtell, and G. E. Kidd. Statistics of atmospheric turbulence within and above a corn canopy. *Boundary-Layer Meteorology*, 24(4):495–519, December 1982. doi:10.1007/BF00120736.

[120] P. Wu, T.-X. Jiang, S. Suksaweang, R. B. Widelitz, and C.-M. Chuong. Molecular shaping of the beak. *Science*, 305(5689):1465 –1466, 2004. doi:10.1126/science.1098109.

[121] L. Yafetto, L. Carroll, Y. Cui, D. J. Davis, M. W. F. Fischer, A. C. Henterly, J. D. Kessler, H. A. Kilroy, J. B. Shidler, J. L. Stolze-Rybczynski, Z. Sugawara, and N. P. Money. The fastest flights in nature: High-speed spore discharge mechanisms among fungi. *PLoS ONE*, 3(9):e3237, September 2008. doi:10.1371/journal.pone.0003237.

A

Species List for Beak Shape Study

Table A.0.1: List of analyzed bird species showing their group shape based on the analysis illustrated in Fig. 2.1.2. Bird species with the same number or letter in the group shape column collapse onto each other under scaling alone and thus have the same beak shape. The order of this list is identical with that of the heatmap shown in Fig. 2.1.2B. Fig. A.0.1 shows how the group shapes listed here translate to the colors used in Figs. 2.1.1 and 2.1.2.

species name	group shape
Cyanicterus cyanicterus	T
Compsothraupis loricata	Z
Sericossypha albocristata	Z
Nemosia pileata	Z
Tersina viridis	H
Cyanerpes caeruleus	H
Cyanerpes cyaneus	H
Cyanerpes nitidus	H
Cyanerpes lucidus	H
Dacnis venusta	G
Dacnis nigripes	G
Dacnis albiventris	D

Table A.0.1: List of analyzed bird species (continued)

species name	group shape
Dacnis flaviventer	E
Dacnis cayana	G
Dacnis hartlaubi	D
Dacnis lineata	E
Dacnis vigueri	G
Poospiza caesar	1
Cypsnagra hirundinacea	1
Donacospiza albifrons	W
Poospiza thoracica	1
Urothraupis stolzmanni	1
Poospiza cabanisi	1
Poospiza erythrophrys	1
Poospiza melanoleuca	2
Poospiza nigriceps	1
Poospiza whitii	2
Compsospiza garleppi	1
Saltatricula multicolor	4
Saltator atricollis	4
Saltator atriceps	4
Saltator atripennis	4
Saltator maximus	4
Saltator cinctus	1
Saltator aurantiirostris	1
Saltator maxillosus	4
Saltator nigriceps	4
Saltator orenocensis	1
Saltator similis	1
Saltator albicollis	1
Saltator striatipectus	1
Saltaotr coerulescens	1
Copyphaspiza melanotis	8
Embernagra platensis	8
Emberizoides ypiranganus	8
Emberizoides herbicola	8
Emberizoides duidae	8

Table A.0.1: List of analyzed bird species (continued)

species name	group shape
Euneornis campestris	4
Loxipasser anoxanthus	0
Tiaris canorus	0
Tiaris bicolor	0
Melanospiza richardsoni	0
Loxigilla noctis	0
Loxigilla barbadensis	0
Certhidea olivacea	1
Certhidea fusca	1
Tiaris fuliginosus	0
Tiaris obscurus	0
Geospiza magnirostris	0
Geospiza fuliginosa	0
Camarhynchus pallidus	1
Camarhynchus psittacula	1
Camarhynchus parvulus	1
Pinaroloxias inornata	1
Geospiza fortis	0
Geospiza conirostris	0
Geospiza difficilis	0
Geospiza scandens	0
Platyspiza crassirostris	2
Melopyrrha nigra	4
Loxigilla violacea	3
Loxigilla portoricensis	3
Tiaris olivaceus	5
Coereba flaveola	4
Oryzoborus crassirostris	0
Sporophila collaris	0
Sporophila schistacea	7
Sporophila falcirostris	7
Oryzoborus angolensis	6
Sporophila luctuosa	7
Sporophila caerulescens	6
Sporophila castaneiventris	0

Table A.0.1: List of analyzed bird species (continued)

species name	group shape
Sporophila minuta	o
Sporophila hypoxantha	9
Sporophila hypochroma	9
Sporophila palustris	o
Sporophila ruficollis	o
Sporophila cinnamomea	9
Sporophila leucoptera	o
Charitospiza eucosma	o
Creurgops verticalis	Q
Creurgops dentatus	Q
Tachyphonus cristatus	V
Tachyphonus luctuosus	V
Heterospingus xanthopygius	P
Sicalis uropygialis	F
Sicalis lebruni	F
Sicalis olivascens	F
Sicalis auriventris	F
Sicalis lutea	J
Sicalis flaveola	J
Sicalis columbiana	F
Diglossa glauca	M
Diglossa caerulescens	M
Diglossa cyanea	M
*Diglossa baritula**	M
Xenodacnis parina	F
Acanthidops bairdii	N
Haplospiza unicolor	K
Oreomanes fraseri	K
Thraupis bonairensis	B
Saltator rufiventris	V
Iridosornis porphyrocephalus	B
Iridosornis analis	B
Iridosornis reinhardti	C
Iridosornis rufivertex	C
Iridosornis jelskii	C

Table A.0.1: List of analyzed bird species (continued)

species name	group shape
Lophospingus pusillus	S
Lophospingus griseocristatus	R
Neothraupis fasciata	S
Diuca diuca	R
Gubernatrix cristata	S
Stephanophorus diadematus	U
Paroaria capitata	S
Paroaria gularis	S
Paroaria dominicana	S
Paroaria coronata	S
Chlorochrysa phoenicotis	Y
Chlorochrysa nitidissima	Y
Chlorochrysa calliparaea	Y
Tangara varia	A
Tangara xanthogastra	A
Tangara guttata	A
Tangara rufigula	A
Tangara nigroviridis	A
Tangara dowii	A
Tangara fucosa	A
Tangara vasorii	A
Incaspiza pulchra	F
Phrygilus fruticeti	F
Phrygilus alaudinus	F
Poryphyrospiza caerulescens	F
Catamblyrynchus diadema	B
Orechestichus abeillei	Q
Parkerthraustes humeralis	X

Figure A.0.1: Color table for group shapes as identified by the morphological analysis shown in Fig. 2.1.2. These colors are identical to the color scheme used in the phylogeny shown in Fig. 2.1.1.

B

Selection criteria for apical ring data

B.1 Search rules

We performed an in-depth search for publications that potentially contain high resolution images of apical ring cross sections to allow comparison with our theoretical predictions. We specifically targeted three main types of articles that are most likely to contain this type of data:

1. Studies on the actual structure of the ascus apex following Chadefaud's initial observations [32])
2. Original species descriptions
3. Comparative studies of ascus structure between genera and families.

Our strategy was to first sample the literature in these three areas with strategically chosen keywords and then refine the results by searching references and author publications for articles that contain desired data.

As a first step we queried both Google Scholar and Web of Science for any three of the following four criteria: [1]

[1] An example of a valid search in Google Scholar notation would thus be `("inoperculate discomycetes" OR "sordariomycetes" OR "leotiomycetes") AND ("ascus"`

- ”ultrastructure” or ”fine structure” or ”tem” or ”morphological studies”
- ”inoperculate discomycetes” or ”sordariomycetes” or ”leotiomycetes”
- ”ascus” or ”asci”
- ”apical ring” or ”apical pore” or ”apical annulus” or ”ascus apex” or ”apical thickening”

This returns a library of over 500 potential publications that we checked by hand for appropriate data (see appendix B.2). We found 26 papers that satisfy the criteria outlined there (hits). For each of these hits we compiled an additional list of all publications

- published by any of the authors
- referenced in the hits
- referencing these hits, based on both Google Scholar and Web of Science

resulting in an additional library of roughly 500 papers after screening for overlap with the former list and subject matter (e.g. excluding publications in botany or about fungal classes that cannot have apical rings). We again searched this list by hand for images of apical rings according to appendix B.2 and found an additional 12 hits. Repeating this last step for the new hits generated only a very small library of roughly 50 publications with no new results, indicating that we have thoroughly sampled the target subject areas. For a full list of papers used to generate the plots in figure 3.3.10 (all hits) see table C.1.1 and the associated figure C.1.1.

B.2 Selection Criteria and Measurements of Apical Ring Images

Our goal was to extract the key dimensions of apical rings (ℓ, b, d) from published micrographs. To ensure accuracy we only used micrographs that

1. display a **median** or very nearly median longitudinal section or projection of an apical ring: this is the only geometric configuration in which all 3 dimensions can be reliably measured.

OR "asci") AND ("apical ring" OR "apical pore" OR "apical annulus" OR "ascus apex" OR "apical thickening").

2. have enough contrast and resolution such that the apical **ring** is clearly **distinguishable**

3. be in a developmental stage between advanced immature and **mature** in the notation of Verkley [112]: the individual dimensions of apical rings vary significantly during development [84, 114], however they essentially stop developing at some point before full maturity is reached.

4. the **resolution** is **high** enough such that potential measurement errors in ring shape are below $\pm 2\%$ in terms of the estimated ejection velocity.

Table C.1.1 shows the results of these measurements, which were used to create the plots in figure 3.3.10.

B.3 Selection Criteria for Spore Dimension Measurements

To determine whether a correlation between ring shape and spore size exists, we needed to determine the spore diameter for all species where accurate high-resolution apical ring cross sections are available. Variations in spore size can be quite pronounced in some species, so it is desirable to determine spore size from a source that as closely as possible matches the specimen for which the apical ring was measured. However most publications containing apical ring micrographs do not contain specific information on spore sizes, so we had to use average spore sizes reported elsewhere in the literature. We used the following order for spore size measurement sources, where the expected uncertainty mildly increases the further down an item is listed:

1. spore size given in the text of the publication, where the apical ring dimensions were measured

2. spore size measured from images in the publication where the apical ring dimensions were measured

3. in species with populations that vary in spore size, spore size reported in publications from the same or a similar population

4. average spore size from measurements of a representative number of spores (> 20) online or in a publication with explicitly reported median size

5. calculated average spore size from the lower and higher range of spore size in standard sources [23, 36]

C

Species list for apical ring study

C.1 Data for Species with Functional Apical Rings

Table C.1.1: Data for species with functional apical rings

species name	W (μm)	$\ell \times b \times d$ (μm)	S_r (μm$^{1/2}$)	#
Albotricha acutipila	1.50 [23]	0.85×0.30×0.42 [71]	2.16	1
Annulohypoxylon multiforme	4.50 [25]	1.16×0.57×0.80 [25]	3.57	2
Brunnipila clandestina	1.65 [23]	0.91×0.28×0.33 [71]	1.60	3
Bulgaria inquinans	6.75 [112]	1.20×0.87×1.30 [112]	5.79	4
Chlorociboria aeruginascens	1.75 [23]	0.58×0.40×0.26 [116]	1.43	5
Ciboria acerina	6.00 [34]	1.27×1.19×1.26 [34]	5.09	6
Ciboria batschiana	5.00 [36]	1.13×0.36×0.76 [113]	3.88	7

Table C.1.1: Data for species with functional apical rings (continued)

species name	W (μm)	$\ell \times b \times d$ (μm)	S_r (μm$^{1/2}$)	#
Cudoniella clavus	4.50 [23]	0.28×0.84×0.44 [116]	3.53	8
Dasyscyphella cassandrae	2.00	0.93×0.25×0.29 [71]	1.40	9
Dialonectria episphaeria	3.55 [25]	0.80×0.35×0.57 [25]	3.17	10
Diaporthe eres	2.57 [25]	1.41×0.71×0.54 [25]	1.95	11
Eutypella quaternata	3.50 [25]	0.34×0.14×0.52 [25]	6.11	12
Fasciatispora petrakii	6.00 [57]	0.77×0.26×0.65 [57]	4.30	13
Gelasinospora tetrasperma	14.50	1.77×1.02×2.33 [87]	9.75	14
Geoglossum nigritum	5.50 [23]	1.83×1.04×1.07 [114]	3.59	15
Hymenoscyphus herbarum	2.50 [23]	0.54×0.43×0.37 [116]	2.19	16
Hypoxylon fragiforme	5.70	0.91×0.57×0.98 [49]	5.19	17
Lachnum bicolor	1.75 [23]	1.38×0.38×0.31 [71]	1.15	18
Lachnum brevipilosum	1.70	0.83×0.21×0.26 [71]	1.30	19
Mitrula paludosa	2.75 [23]	1.22×0.52×0.72 [114]	3.13	20
Monilinia johnsonii	4.15 [113]	1.39×0.53×0.58 [113]	2.24	21
Natantiella ligneola	3.64 [25]	1.14×0.38×0.97 [25]	5.31	22
Neobulgaria pura	5.25 [36]	1.39×0.98×1.62 [112]	6.90	23
Neurospora crassa	16.58 [86]	0.61×0.28×1.27 [86]	12.60	24

Table C.1.1: Data for species with functional apical rings (continued)

species name	W (μm)	$\ell \times b \times d$ (μm)	S_r (μm$^{1/2}$)	#
Neurospora lineolata	12.00	0.77×0.38×1.26 [52]	9.40	25
Neurospora tetrasperma	17.00	1.04×0.68×1.90 [86]	11.36	26
Ombrophila hemiamyloidea	3.50 [117]	0.71×0.93×0.50 [117]	2.49	27
Ombrophila violacea	4.00 [23]	1.47×0.25×0.77 [112]	4.05	28
Peltigera canina	3.20 [54]	1.69×0.73×0.77 [54]	2.68	29
Pezicula ocellata	13.00 [115]	1.30×0.13×0.83 [115]	6.85	30
Pezizella alniella	2.75 [23]	0.73×0.32×0.43 [116]	2.37	31
Pezizella gemmarum	2.10 [23]	0.46×0.32×0.29 [116]	1.87	32
Phaeohelotium carneum	3.25 [23]	0.55×0.40×0.58 [116]	3.81	33
Podosordaria leporina	9.30 [65]	1.14×0.78×1.34 [65]	6.36	34
Poronia punctata	9.50 [36]	1.74×0.60×1.50 [107]	6.61	35
Rutstroemia lindaviana	1.75 [36]	0.53×0.26×0.23 [113]	1.36	36
Rutstroemia petiolorum	4.50 [36]	1.05×0.46×0.76 [113]	3.73	37
Ruzenia spermoides	4.94 [25]	1.06×0.36×1.05 [25]	6.24	38
Sclerotinia sclerotiorum	5.00 [23]	1.40×0.42×0.67 [113]	2.79	39
Sordaria fimicola	16.08 [90]	0.72×0.41×1.57 [90]	12.93	40
Sordaria humana	15.00 [36]	2.28×1.08×2.92 [95]	11.54	41
Spirodecospora bambusicola	13.00	2.59×1.18×2.98 [18]	10.75	42

Table C.1.1: Data for species with functional apical rings (continued)

species name	$W\,(\mu\mathrm{m})$	$\ell \times b \times d\,(\mu\mathrm{m})$	$S_r\,(\mu\mathrm{m}^{1/2})$	#
Stromatinia rapulum	6.25	1.43×0.45×0.74 [113]	3.13	43
Xylaria hypoxylon	5.00 [23]	0.66×0.31×0.43 [15]	2.58	44
Xylaria longipes	6.00 [23]	1.85×0.47×0.89 [16]	3.44	45

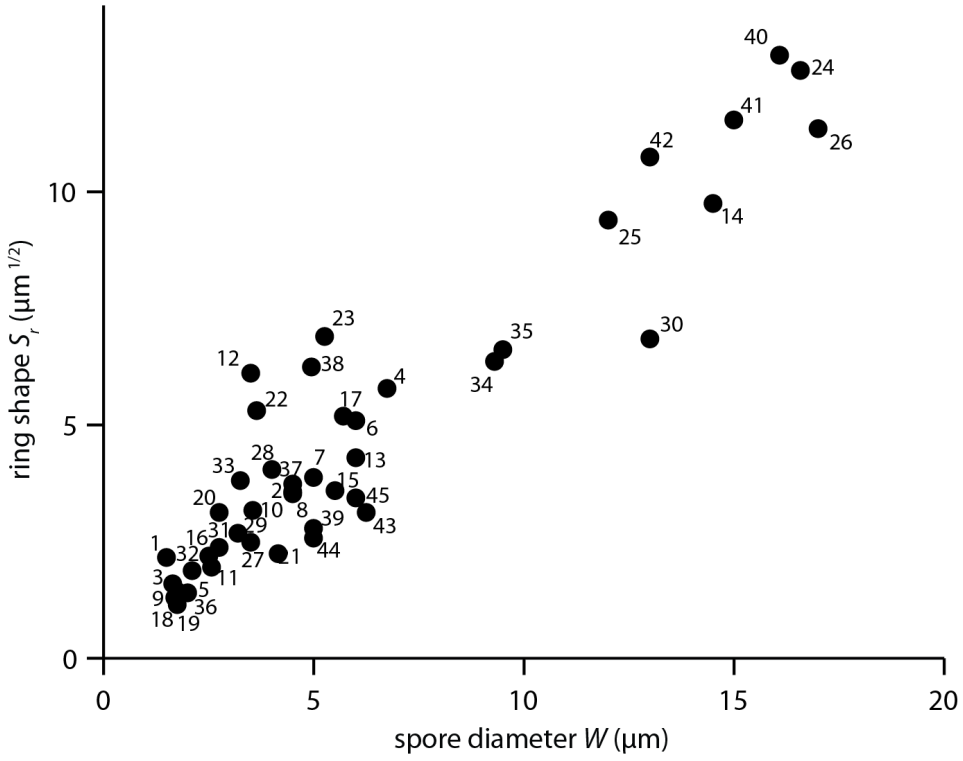

Figure C.1.1: Plot of ring shape S_r over spore size W with number labels corresponding to table C.1.1. The data shown is identical to figure 3.3.10.

C.2 Data for Species with Non-functional Apical Rings

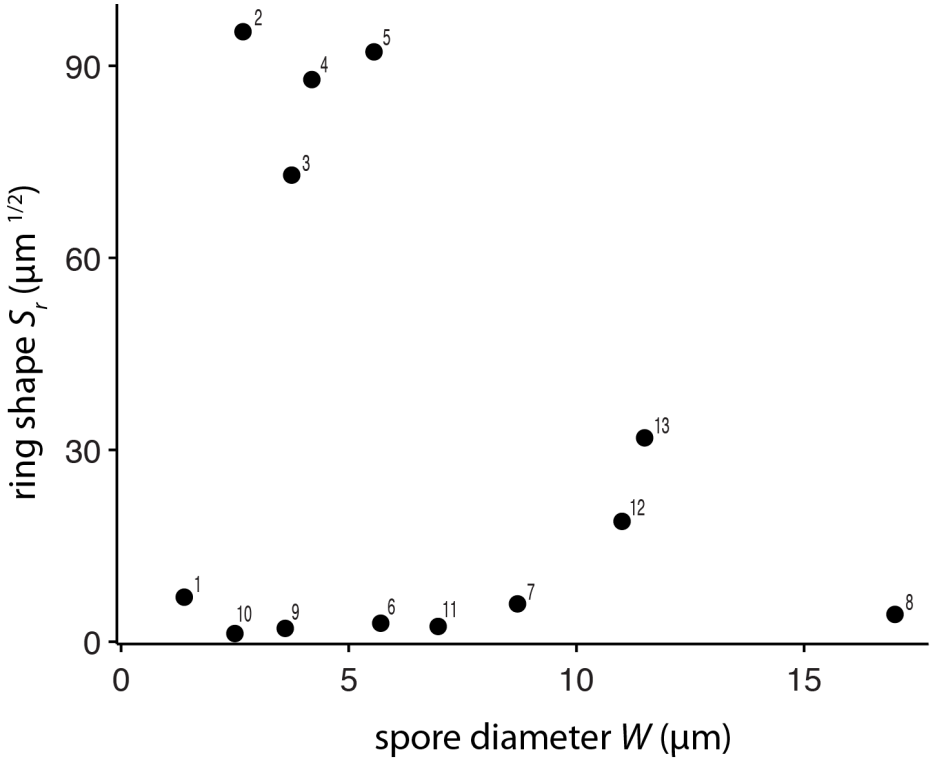

Figure C.2.1: Plot of ring shape S_r over spore size W with number labels corresponding to table C.2.1. The data shown is identical to figure 3.3.11.

Table C.2.1: Morphological data for ascomycete species with non-functional apical rings

species name	$W\,(\mu\mathrm{m})$	$\ell \times b \times d\,(\mu\mathrm{m})$	$S_r\,(\mu\mathrm{m}^{1/2})$	#	reason for loss of function
Laboulbeniopsis termitarius	1.90 [19]	1.45×0.81×1.46 [19]	6.26	1	ascus wall dissolves [19]
Thelebolus stercoreus	3.10 [97]	8.22×4.39×28.79 [97]	97.32	2	ejection into closed sporocarp [97]
Thelebolus polysporus	3.75 [97]	3.25×4.39×11.06 [97]	72.92	3	ejection into closed sporocarp [97]
Thelebolus crustaceus	4.50 [97]	5.21×2.35×18.42 [97]	88.28	4	ejection into closed sporocarp [97]
Thelebolus microsporus	5.27 [97]	1.64×0.41×6.37 [97]	91.94	5	ejection into closed sporocarp [97]
Aniptodera salsuginosa	5.70 [81]	1.02×1.79×0.72 [81]	2.92	6	ejection through ascus wall [81]
Magnaporthe salvinii	8.70 [66]	1.25×1.29×1.44 [66]	5.91	7	ascus wall dissolves [66]
Prostratus cyclobalanopsidis	17.0 [104]	2.42×1.51×1.73 [104]	5.16	8	ascus detaches [104]
Diaporthe phaseolorum	3.60 [63]	1.72×0.59×0.60 [63]	2.07	9	ascus detaches [63]
Lollipopaia minuta	2.50 [58]	0.96×0.35×0.29 [58]	1.31	10	ascus detaches [58]
Chaetosphaeria chaetosa	6.96 [89]	1.43×0.47×0.61 [89]	2.44	11	ascus wall dissolves [89]
Aniptodera chesapeakensis	11.0 [79]	0.22×0.37×1.31 [79]	18.87	12	ascus wall dissolves [79]
Halosarpheia marina	11.5 [79]	0.13×0.44×1.65 [36]	31.86	13	ascus wall dissolves [79]

D

Pressure Volume Relation for Ascus

Here we outline a model calculation for the pressure volume relation in the ascus. As noted above, since the volume change in the ascus is small during the ejection of a single spore, for our calculation it is valid to approximate the pressure as depending linearly on the ascus volume. However, it is of interest to understand the full nonlinear relationship between pressure and volume in the ascus and here we outline a plausible model. Our model is based on the fact that the ascus walls are very thin, yet the ascus changes its volume by roughly an order of magnitude during its expansion before ejection. This makes it plausible that the ascus wall has material properties similar to polymer networks in a hyperelastic material (like e.g. in a balloon).

The main feature of (ideal) polymer networks is that cross-links are evenly and randomly distributed in the bulk of the material. This leads to chains along which stress can be propagated that have random configurations. If we consider a deformation of this network, described by elongation factors λ_i in dimensions x_i we can calculate the change in entropy S associated with this deformation [44]

$$S = -\frac{kn_e}{2}\left(\sum_{i=1}^{3}\lambda_i^2 - 3 - \ln\prod_{i=1}^{3}\lambda_i\right) \tag{D.1}$$

where n_e is the number of chains. As a good approximation the volume of the

ascus wall stays constant and thus $\prod_{i=1}^{3} \lambda_i = 1$ which simplifies things quite a bit. We want to consider a reversible process ($dQ = TdS$), where work is done by an external pressure, which creates reaction forces f_i along the directions x_i. The change in internal energy associated with this process is

$$dE = TdS + \sum_{i=1}^{3} f_i dx_i \tag{D.2}$$

For an ideal polymer, we would expect $(\partial E/\partial x_i)_{T,V} = 0$ and thus

$$f_i = -T\left(\frac{\partial S}{\partial x_i}\right)_{T,V} \tag{D.3}$$

The stress (with reference to the undeformed state) is

$$\tau_i = \frac{l_i}{V} f_i + \tau_p \tag{D.4}$$

where l_i is the length in direction x_i, V is the volume of the bulk and τ_p is an arbitrary constant (e.g. hydrostatic pressure). From this we can derive a stress-strain (or elongation ratio) relationship

$$\tau_i = \frac{l_i}{V}\left(-T\frac{\lambda_i}{l_i}\frac{\partial S}{\partial \lambda_i}\right) + \tau_p \tag{D.5}$$

or more concretely

$$\tau_i = G\lambda_i^2 + \tau_p \tag{D.6}$$

where $G \approx n_e kT/V$ is the shear modulus of the material.

In the case of an elastic thin-walled cylinder, we have 3 major dimensions: z,r and t. We define the extension ratios along these dimensions as $\lambda_z = l/l_0$, $\lambda_r = r/r_0$ and $\lambda_t = t/t_0$. To impose conservation of volume we approximate the cylinder wall volume by

$$V_w = 2\pi rlt \tag{D.7}$$

ignoring the bottom and top and thus the volume is linear with regard to the major dimensions. Motivated by classical mechanics and the stresses in thin shells we introduce an anisotropy factor a to express the extension ratios as functions of each other.

$$\lambda_r = \lambda_z^a \,;\, \lambda_t = \lambda_z^{-(1+a)} \tag{D.8}$$

where the last relation results from volume conservation.

The arbitrary constant in the stress strain relation can be determined from $\tau_t = 0$ as

$$\tau_p = G\lambda_z^{-2(1+a)} \tag{D.9}$$

which gives us for the other two stresses

$$\tau_z = G\left(\lambda_z^2 - \lambda_z^{-2(1+a)}\right) \tag{D.10}$$

and

$$\tau_r = G\left(\lambda_z^{2a} - \lambda_z^{-2(1+a)}\right) \tag{D.11}$$

The force balances in z and r direction give us a relation between the stresses and the pressure inside the ascus.

$$2\pi r t \tau_z = p\pi r^2 \tag{D.12}$$

and

$$2\pi\Delta l \tau_r = 2r\Delta l p \tag{D.13}$$

With this information we can eliminate the stresses and nondimensionalize with $\tau_{sm} = \frac{2Gt_0}{r_0}$

$$\frac{p}{\tau_{sm}} = \frac{\lambda_z^2 - \lambda_z^{-2(1-a)}}{\lambda_z^{1+2a}} \tag{D.14}$$

and from equation (D.13)

$$\frac{p}{\tau_{sm}} = \frac{\lambda_z^{2a} - \lambda_z^{-2(1-a)}}{2\lambda_z^{1+2a}} \tag{D.15}$$

We can substitute λ_z with a dimensionless volume $\tilde{V} = \frac{\pi r^2 l - \pi r_0^2 l_0}{\pi r_0^2 l_0} = \lambda_z^{1+2a} - 1$ and eliminate a by combining equations (D.14) and (D.15) to get a pressure volume relationship in dimensionless form

$$\frac{p}{\tau_{sm}} = \frac{(1+\tilde{V})^2 - 1}{2(1+\tilde{V})}\left(\frac{2}{(1+\tilde{V})^2\left((1+\tilde{V}^2)^2+1\right)}\right)^{1/3} \tag{D.16}$$

Figure D.0.1 plots the predicted pressure volume relationship. The main point for the purposes of this manuscript is that during the ejection of a single spore, the volume does not change by very much, and in the region where pressure and

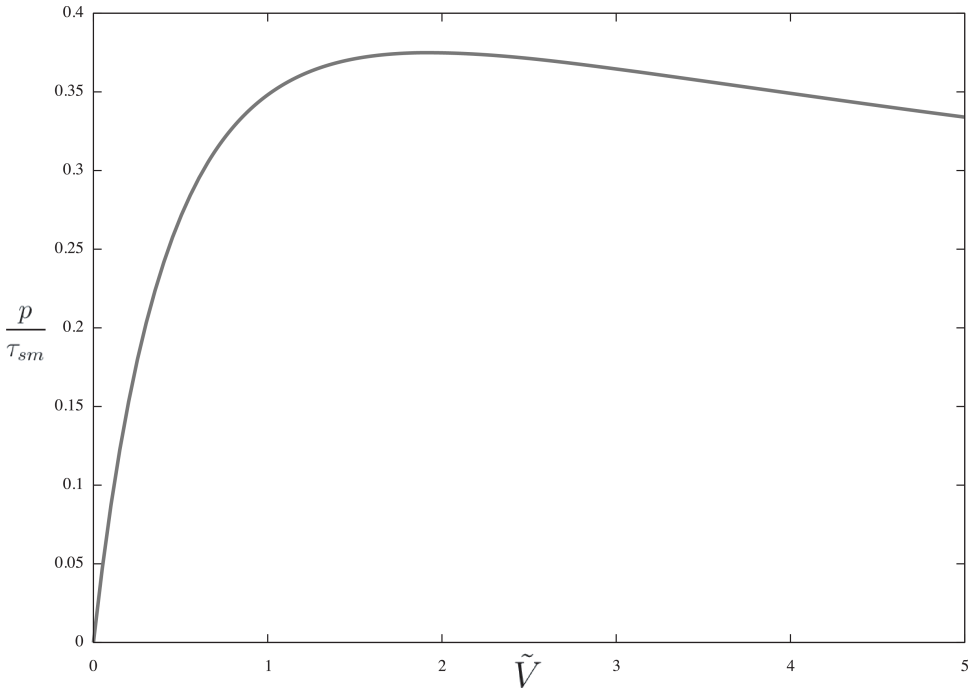

Figure D.0.1: Expected pressure volume relation for a fungal ascus. In the region where pressure and volume covary (for small $\tilde{V}$), they are approximately linearly related. This is the regime where we expect asci to operate during spore ejection.

volume covary (experimental evidence shows that they do[59]), their relation is indeed roughly linear. We therefore assume that fungal asci opperate in the small $\tilde{V}$ regime and consider the pressure volume relationship of the spore to be linearized around the initial ascus volume.